



# Experimental and numerical study of humid granular material: influence of liquid content in quasi-static regime

Haithem Louati

## ► To cite this version:

Haithem Louati. Experimental and numerical study of humid granular material: influence of liquid content in quasi-static regime. Chemical and Process Engineering. Ecole des Mines d'Albi-Carmaux, 2016. English. NNT: 2016EMAC0008 . tel-01426070

**HAL Id: tel-01426070**

**<https://theses.hal.science/tel-01426070>**

Submitted on 4 Jan 2017

**HAL** is a multi-disciplinary open access archive for the deposit and dissemination of scientific research documents, whether they are published or not. The documents may come from teaching and research institutions in France or abroad, or from public or private research centers.

L'archive ouverte pluridisciplinaire **HAL**, est destinée au dépôt et à la diffusion de documents scientifiques de niveau recherche, publiés ou non, émanant des établissements d'enseignement et de recherche français ou étrangers, des laboratoires publics ou privés.



# THÈSE

En vue de l'obtention du

**DOCTORAT DE L'UNIVERSITÉ DE TOULOUSE**  
**Délivré par :** École Nationale Supérieure des Mines d'Albi-Carmaux

---

**Présentée et soutenue par :**

**Haithem Louati**

le 04/11/2016

**Titre :**

EXPERIMENTAL AND NUMERICAL STUDY OF HUMID GRANULAR  
MATERIAL : INFLUENCE OF LIQUID CONTENT IN QUASI-STATIC REGIME

---

**École doctorale et spécialité :**

*MEGEP : Génie des procédés et de l'Environnement*

**Unité de Recherche :**

*Centre RAPSODEE, CNRS – UMR 5302, Ecole des Mines d'Albi-Carmaux*

**Directeurs de Thèse :**

Alain de Ryck – Directeur de thèse  
Driss Oulahna – Co-directeur de thèse

**JURY :**

Olivier Bonnefoy	Professeur, Ecole des Mines de Saint-Etienne	Rapporteur / Président
Bogdan Cazaciu	Professeur, IFSTTAR Nantes	Rapporteur
Mojtaba Ghadiri	Professeur, IPSE University of Leeds	Examineur
Martin Morgeneyer	Dr Ingénieur, UTC Compiègne	Examineur
Alain de Ryck	Professeur, Ecole des Mines d'Albi	Directeur de thèse
Driss Oulahna	MA HDR, Ecole des Mines d'Albi	Co-directeur de thèse



# Table of contents

<b>Table of contents .....</b>	<b>1</b>
<b>Table of Appendices .....</b>	<b>3</b>
<b>Introduction .....</b>	<b>5</b>
<b>Chapter 1. Introduction to the granular material.....</b>	<b>9</b>
1.1. Introduction.....	10
1.2. Granular material properties .....	10
1.2.1. Particle size and size distribution.....	10
1.2.2. Surface Roughness .....	11
1.2.3. Arrangement of the granular material and voidage fraction.....	11
1.2.4. Inter-particle forces.....	12
1.3. Wet granular material properties .....	13
1.3.1. Wettability of granular materials .....	13
1.3.2. Saturation states of liquid .....	14
1.3.3. Liquid bridge force in the pendular regime .....	15
1.3.4. Viscous force in the pendular regime .....	17
1.4. Mechanical properties of dry and wet granular materials.....	18
1.4.1. Angle of repose and critical angle of a granular pile .....	18
1.4.2. Granular friction and cohesion .....	20
1.4.3. Tensile strength for wet granular material .....	21
1.4.4. Stresses and shear tests .....	22
1.4.5. Stick-slip motion .....	25
1.5. Conclusions .....	26
<b>Chapter 2. Introduction to the discrete element method (DEM) .....</b>	<b>31</b>
2.1. Introduction.....	32
2.2. Principle of DEM .....	32
2.3. Equations of motion .....	33
2.4. Simulation time-step.....	33
2.5. Forces in DEM .....	34
2.5.1. Non-contact forces .....	34
2.5.2. Contact forces.....	34
2.6. Input parameters for the simulation.....	44
2.6.1. Contact stiffness .....	44



2.6.2. Coefficient of restitution .....	44
2.6.3. Coefficient of sliding friction .....	44
2.6.4. Coefficient of rolling friction .....	45
2.7. Conclusions .....	45
<b>Chapter 3. Materials and methods .....</b>	<b>51</b>
3.1. Materials and characterisations .....	52
3.1.1. The granular materials .....	52
3.1.2. Characterisation of the granular materials .....	52
3.1.3. Wetting the granular material .....	55
3.1.4. Characterisation of the liquid .....	56
3.2. Characterisation of the flow behaviour of the granular material .....	58
3.2.1. The angle of repose .....	58
3.2.2. The shear test in steady-state conditions .....	59
3.3. Characterisation of the properties of glass beads (2 mm) for the input parameters for the simulation .....	61
3.3.1. Nanoindentation test .....	61
3.3.2. Particle sliding friction .....	62
<b>Chapter 4. Experimental study of the shear behaviour of wet granular material .....</b>	<b>65</b>
4.1. Introduction .....	68
4.2. Shear behaviour of partially wet granular material .....	68
4.2.1. Effect of liquid on the voidage fraction of the granular bed .....	68
4.2.2. Effect of liquid on the steady-state shear stress .....	70
4.2.3. Theoretical estimation of the tensile strength using the Rumpf model .....	74
4.3. Effect of particle size on the shear behaviour of partially wet granular material .....	77
4.3.1. Effect of particle size on the voidage fraction of the granular bed .....	77
4.3.2. Effect of particle size on the shear stress .....	78
4.3.3. Theoretical estimation of the tensile strength using the Rumpf model .....	80
4.4. Investigation of more saturation states of liquid .....	81
4.4.1. Effect of liquid on the voidage fraction .....	82
4.4.2. Effect of liquid on the shear stress behaviour .....	87
4.5. Conclusions .....	89
<b>Chapter 5. Discrete element analysis of the shear behaviour of dry and partially wet granular material .....</b>	<b>99</b>
5.1. Introduction .....	101
5.2. Materials and methods .....	101
5.2.1. Shear test experiment .....	101
5.2.2. Shear test simulation .....	102
5.2.3. Models used for the simulation .....	104

5.3. Results and discussions .....	107
5.3.1. Inter-particle friction measurements .....	107
5.3.2. Effect of microscopic properties on the macroscopic behaviour of the granular material in the simulation.....	109
5.3.3. Effect of liquid on the shear behaviour of wet granular material.....	118
5.4. Conclusions .....	125
<b>Conclusions and perspectives .....</b>	<b>131</b>
<b>References .....</b>	<b>135</b>

## Table of Appendices

<b>Appendices (Chapter 2).....</b>	<b>48</b>
Appendix 2.1. Equivalent stiffness coefficient and damping coefficient.....	48
Appendix 2.2. Equivalent radius, mass, Young modulus and shear modulus.....	48
<b>Appendices (Chapter 4): observation of the stick-slip motion .....</b>	<b>94</b>
Appendix 4.1. The steady-state shear stress signal.....	94
Appendix 4.2. The choice of steady-state shear stress value .....	95
Appendix 4.3. Effect of the liquid fraction on the amplitude of the stick-slip response .....	96
Appendix 4.4. Conclusions .....	97
<b>Appendices (Chapter 5): Investigation of the effect of the rotational speed of the shear cell on the stress ratio response during shearing.....</b>	<b>129</b>



# Introduction

Les milieux granulaires humides peuvent être observés dans notre environnement quotidien tel que le sable de plage, le sol humide sous la pluie, la neige, etc., et dans de nombreuses industries telles que les industries pharmaceutique, alimentaire, minière et de la construction. Les exemples de procédés industriels qui impliquent des milieux granulaires humides sont nombreux tel que la granulation humide, le séchage par pulvérisation, l'atomisation, etc. Ces procédés impliquent différents régimes de saturation en liquide, par exemple un milieu granulaire insaturé pour la granulation humide et un milieu saturé pour l'atomisation. Toutefois, même une faible quantité de liquide (par exemple l'humidité dans l'air) peut influencer le comportement de milieu granulaire. Le changement du comportement de milieu humide par rapport au milieu sec est dû à la cohésion induite par les forces capillaires (Israelachvili, 1991; Hornbaker *et al.*, 1997; Bocquet *et al.*, 1998; Mikami *et al.*, 1998; Fraysse *et al.*, 1999). Les milieux granulaires cohésifs ont un comportement à l'écoulement complexe qui pose certains problèmes lors de la manipulation, notamment un écoulement pauvre lors de vidange des silos ou au niveau des lignes du transport, etc. Malgré les progrès réalisés au cours des deux dernières décennies pour étudier les propriétés d'un milieu granulaire, son comportement reste pas complètement compris (Fournier *et al.*, 2005; Mitarai and Nori, 2006). De plus, une analyse qualitative et quantitative de la cohésion induite par le liquide pour différent régime de saturation est nécessaire pour limiter les problèmes liés à la manipulation de la poudre.

Une étude récente faite au centre Rapsodee par Collet (2010) a été focalisée sur l'analyse du comportement de milieu granulaire sec et humide dans un mélangeur. L'auteur a mis l'accent sur la complexité de cette analyse en présence de plusieurs paramètres qui peuvent influencer le comportement du milieu (les paramètres de procédé, les propriétés du liquide, les propriétés du milieu granulaire). Par conséquent, cette étude en régime dynamique dans le mélangeur a été complétée par une analyse en régime quasi-statique afin d'obtenir une approche simplifiée du mélange et des contraintes locales. Dans notre étude nous analysons le comportement au cisaillement de milieu granulaire humide en utilisant une double approche : expérimentale et numérique. Nous investiguons le comportement du milieu granulaire humide en régime quasi-statique, moyennant une cellule de cisaillement pour une meilleure maîtrise du plan de cisaillement et des contraintes extérieures. Des billes de verre mono-sphérique ont été utilisées pour faciliter la caractérisation et la teneur en liquide a été bien contrôlée. L'étude numérique par la méthode des éléments discrets (DEM) a été effectuée en collaboration avec le groupe de recherche de Prof. Ghadiri à l'université de Leeds durant un séjour de sept mois. La méthodologie adoptée dans cette étude consiste, tout d'abord, à conduire une série d'expérience pour étudier le comportement du milieu granulaire humide à l'échelle macroscopique. Ensuite, cette étude a été complétée par une analyse théorique pour comprendre mieux les phénomènes observés par l'étude expérimentale. Enfin, nous avons mis en place une méthode de simulation en parallèle d'expériences afin de comparer les résultats et de donner une compréhension du comportement granulaire à l'échelle microscopique.

Les objectifs de ce travail consistent à :

- Analyser le comportement du milieu granulaire humide, en régime quasi-statique, et pour différents régimes de saturation. Ainsi, les fractions de liquide ont été largement variées de 0.01% jusqu'à 60% en rapport volumique.
- Investiguer l'effet du liquide en relation avec la contrainte normale appliquée au milieu granulaire. La contrainte normale a été aussi largement variée de 0.3 kPa jusqu'au 11 kPa.
- La variation de la fraction du liquide et de la contrainte normale influence aussi la porosité de milieu granulaire. Ainsi nous analysons l'effet de ces deux paramètres sur la structuration du milieu granulaire humide.
- L'effet de la taille des particules est aussi brièvement étudié dans ce manuscrit et donne lieu à des éventuelles perspectives.
- L'état insaturé du milieu granulaire, en présence des ponts liquides entre les grains, a été largement étudié dans la littérature, de ce fait, plusieurs modèles théoriques ont été développés. Ainsi nous présentons une étude qualitative des forces capillaires moyennant le modèle du Rumpf et de Schubert pour estimer la traction en cisaillement.
- Une étude expérimentale et de simulation numérique pour étudier le comportement au cisaillement du milieu granulaire insaturé a été mise en place pour une meilleur compréhension à l'échelle microscopique.

Ce manuscrit s'articule autour de cinq chapitres. Dans le chapitre 1, nous introduisons le milieu granulaire d'une manière générale et le milieu humide en particulier. Ce chapitre présente aussi l'état de l'art sur les travaux récents dans ce domaine. Le chapitre 2 donne une introduction sur les modèles et les approches de la méthode des éléments discrets (DEM). Certain paramètres d'entrée pour la simulation font un sujet de discussion. Dans le chapitre 3, nous présentons les matériels et méthodes utilisés dans cette étude. Le chapitre 4 est dédié aux résultats expérimentaux du comportement au cisaillement du milieu granulaire humide ; Nous étudions en particulier l'effet de la quantité de liquide et de la contrainte normale appliquée sur le milieu granulaire. A la fin de ce chapitre nous investiguons brièvement le glissement saccadé qui accompagne le signal de la contrainte de cisaillement ; l'amplitude et la fréquence de ce signal dépendent à la fois de la fraction de liquide et la contrainte normale. Enfin, le chapitre 5 est concerné par la méthode de simulation, en utilisant le logiciel EDEM<sup>TM</sup> version V.2.7 de DEM-Solutions Ltd, Edimbourg, UK). Dans ce chapitre, nous traitons l'effet de la propriété de matériau, bille de verre, (Module de Young et le coefficient de frottement) sur le comportement au cisaillement ainsi que l'effet de liquide et la contrainte normale sur le comportement granulaire en cisaillement.

# Introduction

Wet granular materials can be encountered in our every day environment such as beach sand, wet soil under the rain, snow, etc. and in many industries such as pharmaceutical, food processing, mining and construction industries. Examples of processes that involve wet granular material in industry are many such as wet granulation, spray drying, atomisation, etc. These processes imply different states of saturation of liquid, i.e. unsaturated state for wet granulation and slurry state for atomisation or spray drying. Even minute amounts of liquid (for example condensed airborne humidity) can change the behaviour of granular materials. The major change of the wet granular material behaviour compared to the dry one is due to the cohesion induced by the capillary forces (Israelachvili, 1991; Hornbaker *et al.*, 1997; Bocquet *et al.*, 1998; Mikami *et al.*, 1998; Fraysse *et al.*, 1999). Cohesive granular materials have a complex flow behaviour and pose problems in handling and processing, such as poor flow behaviour in the storage bin and transport line etc. Despite progress made over the past two decades to study the wet granular material properties, little is understood in terms of the mechanical properties (Fournier *et al.*, 2005; Mitarai and Nori, 2006). In addition, more quantitative analyses of the cohesion induced by the liquid with various liquid contents are needed to reduce problems in powder handling and processing.

A recent study by Collet (2010), from Rapsodee research centre, was concerned by analysing the behaviour of dry and wet granular material during mixing. Collet highlighted the complexity of the analysis of the wet granular material behaviour in the presence of several parameters (process parameters, liquid properties, granular material properties...). Therefore, the dynamic analysis using a mixer was supported by a quasi-static analysis using a shear tester to achieve a simplified approach to the mixing and the local stresses. In this study, we analyse the shear behaviour of wet granular materials using experimental and numerical approaches. We investigate the wet granular material behaviour in quasi-static regime using an annular shear cell in order to better control the shear plan and the external constraints. Mono-dispersed, spherical glass beads are used to facilitate the characterisation and the quantities of liquid are controlled. The numerical study using the discrete element method (DEM) was performed in collaboration with Ghadiri research group at the university of Leeds during an internship of seven months. The methodology adopted for this study consists of firstly, conducting experiments to analyse the shear behaviour of wet granular material at a macroscopic scale. Secondly, using theoretical models in order to provide an understanding of some experimental results. Finally, conducting experiments and simulations (using the discrete element method) in parallel to compare the results and to gain a microscopic and macroscopic understanding of the shear behaviour.

The objectives of this study include:

- An analysis of the shear resistance of wet granular material, in steady-state regime, for different states of liquid saturation. Thus, the liquid fraction has been largely varied from 0.01% to 60% in volume fraction.
- An investigation of the effect of the normal stress applied to the granular material together with the liquid content variation. The normal stress has been also largely varied from 0.3 kPa to about 11 kPa.
- Both normal loading and liquid content affect the voidage fraction in the granular material. Thus, we study the influence of these two parameters on the voidage fraction.
- A comparative study of the effect of liquid using two different sizes of the granular materials.
- The unsaturated state of wet granular materials, where liquid bridges are formed between grains, has been intensively studied and many theoretical models have been developed. Thus, we provide a qualitative analysis of the cohesive behaviour based on the liquid bridge forces using Rumpf model.
- A simulated and experimental analysis of the shear behaviour of unsaturated granular material in order to provide a better understanding at the microscopic scale.

This manuscript contains five chapters. Chapter 1 is devoted to introduce the granular material properties in general and the wet case in particular. It also contains information on the recent state of the art regarding wet granular material studies. Chapter 2 gives an overview of the models and approaches of the discrete element method. Some relevant parameters for the DEM simulation are also discussed. Chapter 3 describes the materials and methods used in this study. Chapter 4 is concerned by the experimental results of the shear behaviour of wet granular material; the effect of the liquid content and the normal stress applied. At the end of this chapter a brief investigation of the stick-slip motion is given in the appendices. Finally, chapter 5 is concerned with a discrete element analysis of experimental studies (using EDEM<sup>TM</sup> software V.2.7 from DEM-Solutions Ltd, Edinburgh, UK). Different points will be presented and discussed: the effect of some particle properties (Young's modulus and sliding friction coefficient) on the shear behaviour of dry and wet granular material and an investigation of the effect of liquid and normal stress on the unsaturated state of wet granular materials.

# Chapter 1. Introduction to the granular material

---

## Résumé:

Ce chapitre présente une introduction au milieu granulaire en général et les granulaires humides en particulier. Une première partie a été consacrée aux propriétés de particules qui composent le milieu tel que la distribution de taille, la rugosité de la surface et les forces inter-particulaires etc. Ces propriétés permettent de caractériser un milieu granulaire et influencent son comportement à l'écoulement. Une deuxième partie est réservée à l'introduction de l'état de saturation de liquide dans un milieu granulaire et les modèles de calcul de forces capillaires. Enfin, les lois mécaniques qui permettent de caractériser le comportement d'un milieu granulaire ont été brièvement présentées et seront utilisées dans cette étude.

## Abstract:

This chapter is an introduction of the granular material in general and the wet case in particular. Firstly, some of the particle properties such as the size distribution, the surface roughness and the inter-particle forces etc. have been presented. These properties allow to characterise the granular material and influence its flow behaviour. Secondly, the states of saturation of liquid in the granular material have been introduced and the capillary forces have been discussed. Finally, the mechanical laws to characterise the granular material flow have been briefly presented and will be used in our study.



## 1.1. Introduction

The granular material is an assembly of individual particles, discrete but have a collective behaviour due to friction and interactions between particles. The behaviour of the granular material is intermediate between solid, as particles can be held together in a motionless state (e.g., sand dunes), and liquid as they flow (e.g., avalanche). Thus, the behaviour of the granular material can be studied in a discrete way by considering the interaction forces between grains, and in a continuum way by considering the boundary conditions and applying the theories of solid mechanics. In both ways, the particle properties such as the particle size distributions, the morphology, and the surface properties etc. play important roles in the bulk behaviour and should be carefully taken into account. Moreover, the spaces in between particles are generally occupied by fluid (air or liquid), which gives rise to solid-fluid interactions. In addition, the granular materials interact with its environment (e.g., with the powder-handling system), which involves other interactions. All these factors make the understanding of the granular material behaviour complicated.

In this chapter, we first introduce some properties of the granular material, which are concerned in our study, for better understanding of their potential impacts as mentioned above. We devote a second section to the wet granular material properties since it is the focus of our study. Last but not least, we introduce the mechanical properties of the dry and wet granular materials. We mainly consider the mechanical theories in the static and the quasi-static situations.

## 1.2. Granular material properties

### 1.2.1. Particle size and size distribution

The particle size is one of the fundamental factors to characterise a granular material. It gives an idea about the number of particles per unit of mass or volume. The diameter is often sufficient to describe the size of mono-dispersed, spherically shaped granular material. The poly-dispersity of a granular material is conventionally concerned with the particle size dispersion. For poly-dispersed granular material, the mean diameter is not enough to give an idea about the particle size. It is necessary to know the particle size distribution since it predicts the particle arrangement, the voidage fraction and the coordination number (e.g., in the case of a large size distribution, the small particles will be able to be intercalated in between the big ones, leading to reduce the voidage fraction in the granular material). For particles with irregular shapes, a size number can be used and is given by an equivalent sphere diameter, i.e. the diameter of a hypothetical sphere with the same area, mass or volume as the concerned particle (Pietsch, 1991).

In order to determine the particle size distribution, many analytic technologies can be used, such as the laser measurement, the optic measurement or just by sieving operations. Depending on the material properties (size, morphology, dispersity...) it is necessary to well select the method that gives adequate information about the particle size distribution.

### 1.2.2. Surface Roughness

The roughness is the irregularity of the particle surface. The increase of the surface roughness of a granular material increases the inter-particle friction, decreases the coordination number and increases the voidage fraction (Yang *et al.*, 2003). It may also influence the contact areas between particles and affect the inter-particle forces, in particular the liquid bridge forces at small amounts of liquid.

### 1.2.3. Arrangement of the granular material and voidage fraction

The voidage fraction is an important parameter, which helps to have an idea about the arrangement of the particles in the granular material. It is defined as the ratio of the voidage relative to the total volume occupied by the granular material in a container for example. A volume fraction can be alternatively used, which gives the ratio of the volume occupied by the particles relative to the total volume. The arrangement of the granular material directly affects its flow behaviour. The granular material can be orderly arranged, which gives a dense configuration or disorderly arranged, which gives a loose configuration. Considering an arrangement of mono-sized spheres, the densest configuration gives a voidage fraction of 0.36 (Scott, 1962; Scott and Kilgour, 1969) and the loosest configuration gives a voidage fraction of 0.45 (Onoda and Liniger, 1990). The configuration of the granular material can be evolved from loose to dense by applying vibration or compaction. The inter-particle forces such as Van-der-Waals force or capillary force affect the voidage fraction and, hence, the configuration of the granular material. Yu *et al.* (2003) have investigated the relationship between the voidage fraction and the inter-particle forces and proposed this empirical equation:

$$\varepsilon = \varepsilon_0 + (1 - \varepsilon_0)\exp(mR_F^{-n}), \quad \text{Eq. 1.1}$$

where  $\varepsilon$  is the voidage fraction,  $\varepsilon_0$  is the voidage fraction without any inter-particle force.

$R_F$  is the ratio between the magnitudes of the inter-particle forces (Van-der-Waals or capillary force) and the gravity.  $m$  and  $n$  are two parameters, which depend on the granular material packing;  $m = 2.954$  and  $n = 0.156$  for loose random packing and  $m = 2.162$  and  $n = 0.129$  for dense random packing (Yu *et al.*, 2003). Fig. 1.1 shows the variation of the voidage fraction with the inter-particle forces obtained from Eq. 1.1 and data from the literature generated by Yu *et al.* (2003). An increase of the voidage fraction with the inter-particle forces is observed for the different data. This demonstrates that the effect of the inter-particle forces can be really large on the voidage fraction of the granular material. Some of these inter-particle forces will be introduced in the following sections. The effect of the capillary force on the voidage fraction will be analysed in our study in chapter 4.

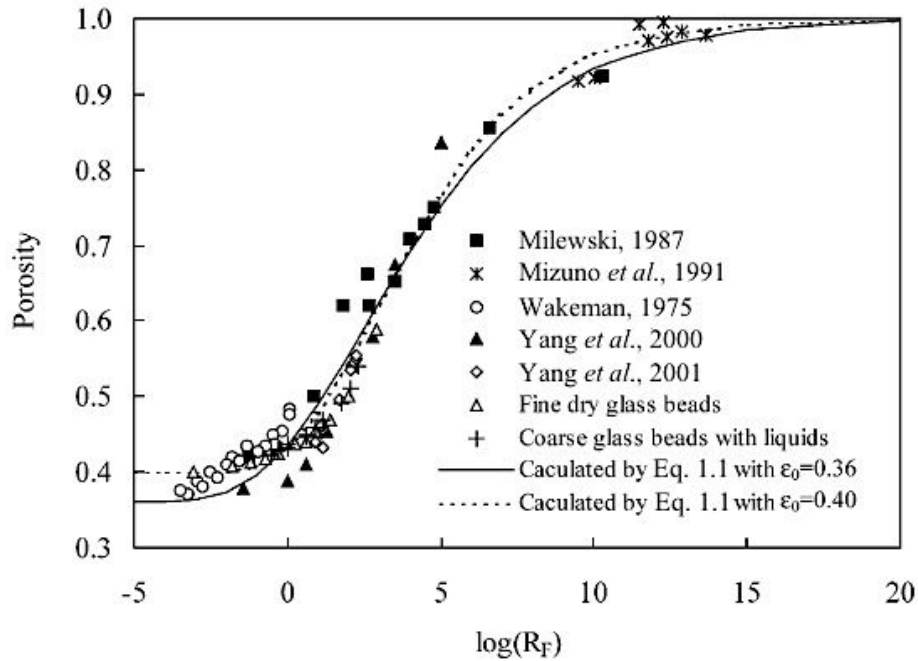


Fig. 1.1. Voidage fraction (porosity) as a function of inter-particle force from Yu *et al.* (2003).

#### 1.2.4. Inter-particle forces

The inter-particle forces are the forces exerted between neighbouring particles. The origin of these forces can be the particles themselves such as Van-der-Waals and electrostatic forces, which have a short-range character, i.e. they act at small distances. Though, the electrostatic force can have also a long-range character. The origin can be an external source such as the capillary and viscous forces in the presence of liquid. The magnitude of these forces depends on the particle properties, in particular the particle size (e.g. Van-der-Waals forces prevail the gravitational force at small particle sizes and the other way around). The inter-particle forces influence widely the flowability of the granular materials. On one hand, they may cause problems in powder processing such as arching in silos, where the inter-particle forces prevail the gravity and hinder the emptying process. On the other hand, these forces are employed in some other processes such as granulation or coating in order to improve the flowability of the granular material by increasing the size of granules. Thus, a good understanding of these forces is necessary for a better estimation of their roles. In the next subsections, we introduce the electrostatic and Van-der-Waals forces and we introduce the capillary and the viscous forces in the next section.

##### 1.2.4.1. Electrostatic force

The electrostatic forces are occurred by the tribo-electric effect due to the friction contact or the corona charge due to the impact charge of ions. These forces can be attractive (between particles of opposite charge) or repulsive (between particles of similar charge). A different distribution of the electrostatic charges can be established depending on the nature of the

materials (conductors or insulators). An estimation of the attractive electrostatic force  $F_E$ , between two identical spherical and non conducting particles, has been given by Piesch (1991), based on Coulomb's formula:

$$F_E = \frac{10q^2}{(1 + \frac{2a}{d})^2} d^2, \quad \text{Eq. 1.2}$$

Where  $F_E(N)$  is the electrostatic force,  $q^2 (N/m^2)$  is the charge density per unit area,  $d (m)$  is the particle diameter and  $2a$  is the inter-particle distance. This expression implies a uniform distribution of the charges on the particle surface.

The electrostatic forces of fine granular material can be really dangerous. In fact, the accumulation of the electric charge during handling powder (e.g., emptying silos) may cause an explosion (e.g., the tragic explosion of flour dust in Minnesota in 1878 has led to the destruction of a mill and the death of a 14 workers (Huntzicker, 2003)).

#### 1.2.4.2. Van-der-Waals force

The Van-der-Waals forces are occurred between permanent dipoles, induced dipoles and one permanent and one induced dipoles. These forces are often attractive forces and they are significant compare to the gravitational forces for small particle size ( $d < 100 \mu m$ ) (Pietsch, 2002). Van-der-Waals forces act also in the presence of gas or liquid within the granular material, although its magnitudes can be reduced in the case of liquid (Visser, 1989). An approximation of this force was given by Hamaker based on the microscopic theory of London-Heitler (Seville, 2000; Israelachvili, 1991), respectively,

between sphere-sphere:

$$F_{vdw} \approx \frac{A_H}{24(2a)^2} d, \quad \text{Eq. 1.3}$$

between sphere-wall:

$$F_{vdw} \approx \frac{A_H}{12(2a)^2} d, \quad \text{Eq. 1.4}$$

where  $A_H$  is the Hamaker constant, which is characteristic of the material and related to the molecular properties, generally in the range of  $10^{-20}$  to  $10^{-19}$  J.

### 1.3. Wet granular material properties

#### 1.3.1. Wettability of granular materials

The wettability can be evaluated by measuring the contact angle,  $\theta_L$ , between the material and the liquid. Generally, small contact angle ( $\theta_L < 90^\circ$ ) means high wettability and large contact angle ( $\theta_L > 90^\circ$ ) means low wettability (see Fig. 1.2). The wettability of granular materials results in the spread of liquid over the grains surface. Grains with high wettability need a small volume of liquid to cover all the surface of grains. The wettability can be interpreted in terms

of surface energy or surface tension at the interface of the different components (solid, liquid and vapour); if the surface energy of the solid-vapour interface is equal to the sum of the surface energies of the solid-liquid interface and the liquid-vapour interface, then the contact angle is zero and the wettability is perfect. However, if the surface energy of the solid-vapour interface is less than that sum, then the contact angle is non-zero and the wettability is partial. The relationship between the contact angle and the surface energies is given by the Young-Dupré equation (Klein *et al.*, 2012) as:

$$w = \cos \theta_L = (\gamma_{sv} - \gamma_{sl}) / \gamma_{lv}, \quad \text{Eq. 1.5}$$

where  $w$  is the wettability of the surface in the range of  $[-1, 1]$ ,  $\gamma_{sv}$  is the surface energy of the solid-vapour interface ( $\text{J/m}^2$ ),  $\gamma_{sl}$  is the surface energy of the solid-liquid interface ( $\text{J/m}^2$ ) and  $\gamma_{lv}$  is the surface energy of the liquid-vapour interface ( $\text{J/m}^2$ ).

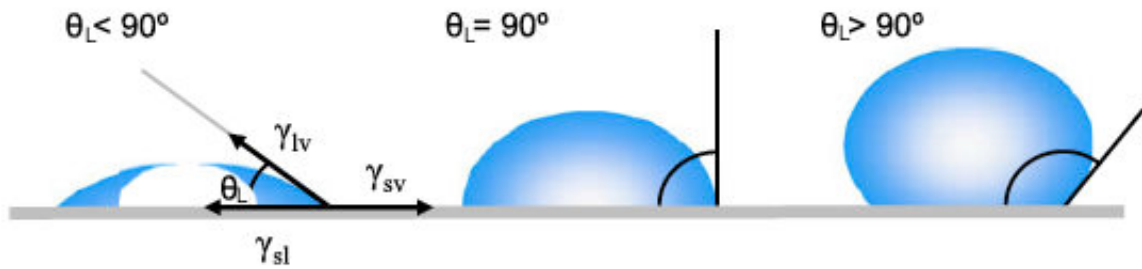


Fig. 1.2. Illustration of contact angles showing the wettability of a solid surface by a liquid (Yuan and Lee, 2013). The wettability decreases from left ( $\theta_L < 90^\circ$ ) to right ( $\theta_L > 90^\circ$ ).

### 1.3.2. Saturation states of liquid

Four saturation regimes of wetting liquid in the granular materials have been distinguished depending on the liquid content: pendular, funicular, capillary and slurry (Newitt and Conway-Jones, 1958; Iveson, 2001). The pendular regime is characterised by the presence of small quantities of liquid incorporated between particles and form liquid bridges at the contact points. Further increase of the amount of liquid leads to the funicular regime, where some neighbouring liquid bridges become connected. The capillary regime is reached when the liquid fills almost all the spaces between particles but the liquid surface forms menisci under the capillary effect. The particles become fully immersed in liquid when the volume of liquid introduced exceeds the volume of voids in the granular material and we talk about the slurry regime. Fig. 1.3 illustrates the four regimes described above. It has been reported that the cohesion arises in the pendular, funicular and capillary regime (Mitarai and Nori, 2006). Moreover, another regime can be observed at very small amounts of liquid, which is not sufficient to form liquid bridges, but the liquid is adsorbed on the surface of the particles and

trapped in the surface roughness. This state is often occurred from a humid environment and depends on the hygroscopic properties of the material. This small liquid may induce some cohesive forces at the contact point between grains (Mason *et al.*, 1999). In addition this adsorbed layer may contribute to enhance some molecular forces such as Van-der-Waals forces (Pietsch, 2002), which contradicts the observation by Vesser (1989).

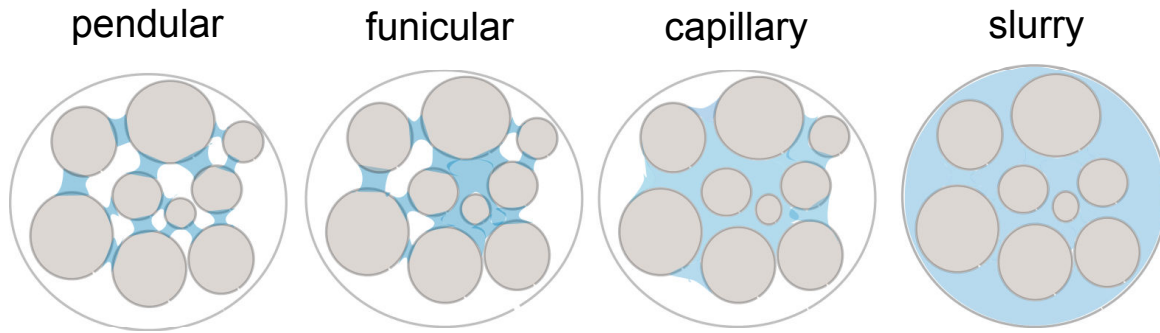


Fig. 1.3. Different saturation states of liquid in granular materials.

### 1.3.3. Liquid bridge force in the pendular regime

Most studies on wet granular materials have been focused on the pendular regime thanks to the well-defined shapes of liquid in form of liquid bridges. Many theories have been established to estimate the liquid bridge force. The latter arises from the capillary depression at the liquid-air interface and the surface tension. The depression of the meniscus is given by the Young-Laplace equation as:

$$\Delta P = \gamma \left[ \frac{1}{r_1} + \frac{1}{r_2} \right], \quad \text{Eq. 1.6}$$

where  $r_1$  and  $r_2$  are the main radii of curvature of the meniscus and  $\gamma$  is the surface tension between air and liquid (Mitarai and Nori 2006). Many approaches have been developed to estimate the liquid bridge force using an approximate geometry of the liquid bridge profile. We detail here the toroidal approximation as an example:

The toroidal approximation, proposed by Fisher (1926) is a simple approach to estimate the liquid bridge force between two spheres. This method consists in considering the meniscus profile at the air-liquid interface as an arc of circle (see Fig. 1.4). Lian *et al.* (1993) have studied the toroidal approach and have reported that it gives a good estimation of the liquid bridge force by comparing the results with the numerical solution of the exact shape of the meniscus. However, the toroidal approximation is less time consuming than solving the exact numerical solution. The force from the toroidal approximation can be calculated using different methods:

The boundary method (Hotta *et al.*, 1974) involves calculating the capillary force at the interface liquid-solid-air and is given as follow (Adams and Perchard, 1985):

$$F_c = 2\pi r_1 \gamma \sin^2 \alpha + \pi r_1^2 \Delta P \sin^2 \alpha, \quad \text{Eq. 1.7}$$

$\alpha$  is the half-filling angle (see Fig. 1.4).

The gorge method (Hotta *et al.*, 1974) involves calculating the force at the neck of the liquid bridge by considering the radius  $r_2$  (see Fig. 1.4) as:

$$F_c = 2\pi r_2 \gamma + \pi r_2^2 \Delta P, \quad \text{Eq. 1.8}$$

The above equations do not give an explicit relationship between the liquid bridge force and the liquid bridge volume or the separation distance. Another expression proposed by Maugis (1987) implies the volume of the liquid bridge,  $V$ , and the half-separation distance,  $a$ , (Pitois *et al.*, 2000) as follow:

$$F_c = 2\pi R \gamma \cos(\theta_L) \left( 1 - \frac{1}{\sqrt{1 + \frac{V}{2\pi R a^2}}} \right). \quad \text{Eq. 1.9}$$

where  $\theta_L$  is the contact angle (see Fig. 1.4). This equation shows that the liquid bridge force increases for an increase in the liquid bridge volume and a decrease in the separation distance. The shortcoming of this model is that it is not valid for a zero separation distance. The limit of the separation distance should be also considered, i.e. the critical separation distance for which a rupture of the liquid bridge is occurred. If the separation distance exceeds the critical value, the liquid bridge force vanishes. A relationship of this critical distance with the volume of liquid bridge was given earlier by Lian *et al.*, (1993) as:

$$a_c = (1 + 0.5\theta_L)V^{\frac{1}{3}}, \quad \text{Eq. 1.10}$$

$\theta_L$  is the contact angle in radians.

The previous methods assume that the gravity effect on the liquid bridge is negligible. Some modified models, which take into consideration the effect of gravity, can be found in this reference (Hotta *et al.*, 1974). It is also assumed that the liquid bridge force is conservative which is not true. Willet (1999) has shown a difference in the force – separation curves for approach and departure cases between two spheres. This reveals a hysteresis and an energy dissipation of the liquid bridge force (Seville *et al.*, 2000).

As mentioned above, the toroidal approximation gives a good estimation of the liquid bridge between two sphere bodies (Hotta *et al.*, 1974; Lian *et al.* 1993), however it was observed an increasingly underestimation as the separation distance increases (Mazzone *et al.*, 1986). Another approach consists of considering a finite separation distance in the expression of the liquid bridge force, which is caused by the asperities at the surface of particles. This will be discussed further in chapter 4.

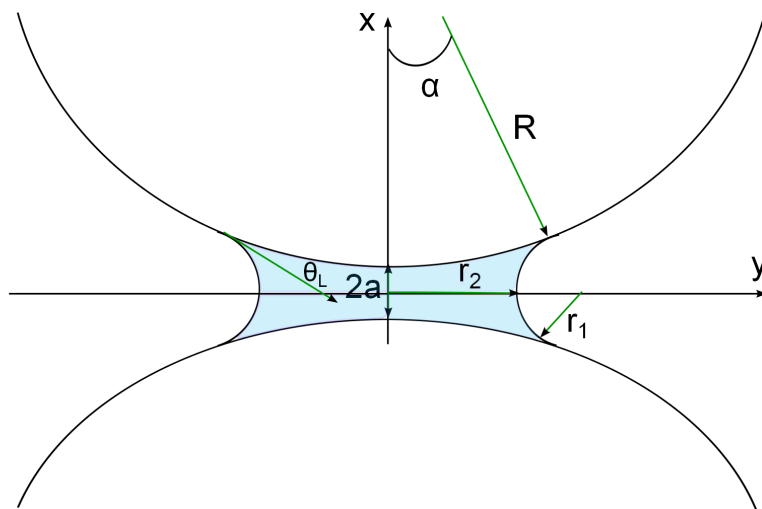


Fig. 1.4. Sketch of a liquid bridge between two spherical particles showing the different parameters used to estimate the liquid bridge force.

#### 1.3.4. Viscous force in the pendular regime

The liquid bridge also dissipates energy by viscous flow (Seville, 2000). The viscous force has a normal component resulting from the elongation or the compression of the liquid bridge and a tangential component resulting from the shear flow of liquid. For two spheres in contact, the normal viscous force,  $F_{vn}$ , can be estimated according to Reynolds' lubrication equation (Iveson *et al.* 2002) as:

$$F_{vn} = 6\pi\mu_v R^* v_n \frac{R^*}{2a}, \quad \text{Eq. 1.11}$$

where  $\mu_v$  is the dynamic viscosity of liquid,  $R^*$  is the equivalent radius of the two spheres and  $v_n$  is the normal relative velocity.

An expression of the tangential viscous force,  $F_{vt}$ , was given by Goldman *et al.* (1967) for sufficiently small separation distance (Lian *et al.*, 1998) as:

$$F_{vt} = \left( \frac{8}{15} \ln \frac{R^*}{2a} + 0.9588 \right) 6\pi\mu_v R^* v_t, \quad \text{Eq. 1.12}$$

where  $v_t$  is the tangential relative velocity.

A dimensionless capillary number  $Ca$  can be used to compare the capillary force and the viscous force contributions to the total liquid bridge force. This number is expressed as the ratio of the dynamic force to the static force as:

$$Ca = \frac{\mu_v v}{\gamma}, \quad \text{Eq. 1.13}$$



where  $v$  is the particle to particle relative velocity. The viscous force prevails if the ratio is larger than 1, however the effect of viscosity can be neglected if the ratio is lower than  $10^{-3}$  (Mikami, 1997; Gras, 2011).

## 1.4. Mechanical properties of dry and wet granular materials

In this section, we introduce some mechanical properties of wet granular materials in static and quasi-static regimes.

### 1.4.1. Angle of repose and critical angle of a granular pile

The deposit of an assembly of grains on a horizontal plane forms a pile, where grains are held by the permanent contact interactions able to withstand in the presence of some tangential stresses. The angle of repose,  $\theta_r$ , of a granular pile is the surface angle after the avalanche. The angle just before the avalanche takes place is called the critical angle  $\theta_c$  (see Fig. 1.5).  $\theta_c$  is the final angle obtained when all grains at the surface are in a stable position, i.e. no grains are rolling down any more (Albert *et al.*, 1997). This angle is independent on the system size (Mitarai and Nori, 2006). The measurement of either angle gives an idea about the cohesive states of the granular material. Bocquet *et al.* (1998) studied the effect of humidity on the critical angle of glass beads in slowly rotating drum. They observed that the critical angle increases for an increase in the condensate liquid with the waiting time (time after sample preparation and before measurement) (see Fig. 1.6). The same figure also displays the increase of the critical angle with the increase of the humidity. Bocquet *et al.* (1998) reported that the critical angle increases due to the increase of the cohesion from the liquid bridges at the contact point. Hornbaker *et al.* (1997) studied the effect of liquid content increasing on the angle of repose of spherical polystyrene beads mixed with oils (pump oil and corn oil). They reported an almost linear increase of the angle of repose with the liquid content (Fig. 1.7). The measured angle of repose of dry beads is  $22^\circ$  and it is rapidly increased by adding very small quantity of liquid. They reported also that the increase of the angle of repose with the liquid due to the cohesive force between particles caused by the formation of small liquid bridges at the contact point between beads. We point out here that the measurements of the angle of repose of wet granular material are more accurate at low humidity since the increase of the liquid amount leads to the formation of particle clusters (Hornbaker *et al.*, 1997). Moreover, it was observed that the angle of repose depends on the system size at large liquid content (Tegzes *et al.*, 1999); it decreases for an increase in the system size. Thus, the continuum analysis of the wet granular material using the Mohr-Coulomb criterion, which will be discussed in the next section, is more appropriate at large liquid content (Mitarai and Nori, 2006).

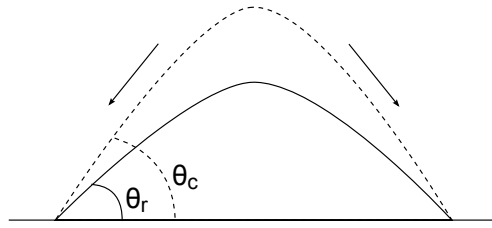


Fig. 1.5. Schematisation of a granular pile.  $\theta_r$  is the angle of repose and  $\theta_c$  is the critical angle.

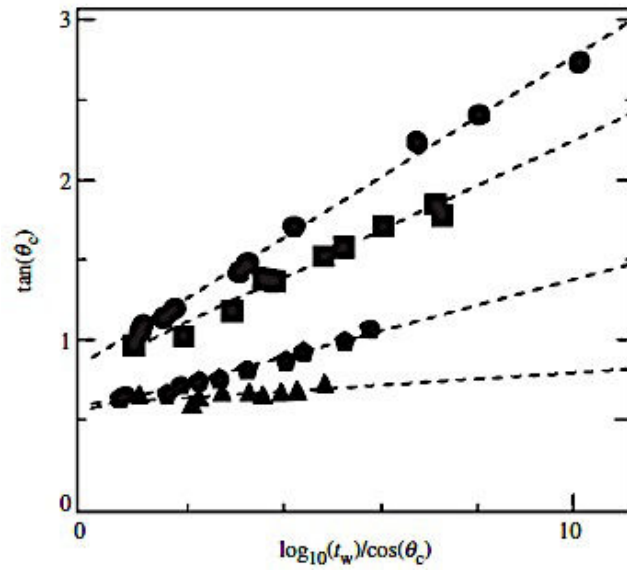


Fig. 1.6. Variation of the critical angle,  $\theta_c$ , of 200  $\mu\text{m}$  glass beads in a rotating drum with the waiting time,  $t_w$  (s), and for different humidities: 15% (triangles), 27% (pentagons) 36.1% (squares) and 45.5% (circles). This figure is a reproduction made by Mitarai and Nori (2006) of the original figure by Bocquet *et al.* (1998).

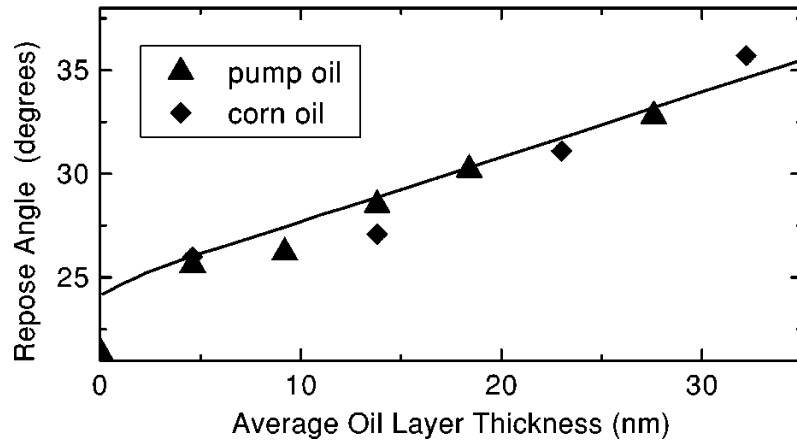


Fig. 1.7. Variation of the repose angle with small liquid content given as an average liquid-layer thickness on polystyrene beads of  $0.8 \pm 0.2$  mm (Albert *et al.*, 1997).

#### 1.4.2. Granular friction and cohesion

The friction in the granular material takes place at the contact between particles. Considering a granular pile as observed in Fig. 1.8-left, the heap shape is maintained due to the balance of frictional forces between grains and gravity. For non-cohesive granular materials, the failure criterion can be given as:

$$\tau > \mu\sigma, \quad \text{Eq. 1.14}$$

where  $\tau$  is the shear stress,  $\sigma$  is the normal stress and  $\mu$  is the internal friction coefficient. The granular material fails if the ratio  $\tau/\sigma$  exceeds  $\mu$ . The internal friction coefficient is related to the critical angle according to:

$$\frac{\tau}{\sigma} = \tan \theta_c = \mu. \quad \text{Eq. 1.15}$$

For cohesive granular materials, the cohesion arises from inter-particle forces and allows to support a finite shear stress supplementary. Fig. 1.8-right shows an increase of the angle of repose of the wet granular pile due to the capillary forces. Thus, the failure criterion is given by Eq. 1.14 plus another term, which takes into account the cohesion as:

$$\tau > \mu(\sigma + T_s), \quad \text{Eq. 1.16}$$

This relationship is known as Mohr-Coulomb criterion. The term  $T_s$  is also called tensile strength and defined as the tensile force at failure per unit surface. The measurement of the stress at failure allows to evaluate the cohesion or the tensile strength of the wet granular materials.

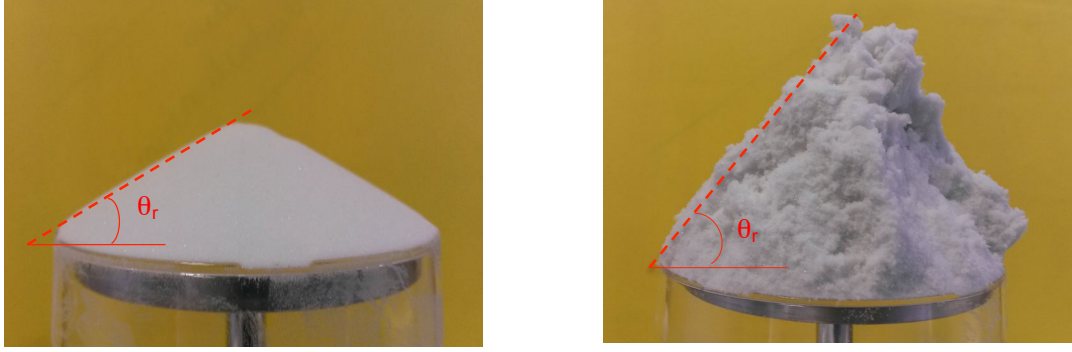


Fig. 1.8. Left, dry glass beads pile, with a well-defined surface angle. Right, wet glass beads with irregular shape and larger angle of repose compared to the dry case.

#### 1.4.3. Tensile strength for wet granular material

For wet granular material, the tensile strength arises from the capillary forces between particles. In the pendular regime, Rumpf (1962) proposed a theoretical model to estimate the tensile strength  $T_s$  (see Eq. 1.16) from the liquid bridge forces, for mono-sized spheres:

$$T_{S,pendular} = (1 - \varepsilon) \frac{k}{\pi} \frac{F_c}{d^2}, \quad \text{Eq. 1.17}$$

where  $F_c$  is the capillary force,  $k$  is the coordination number and  $\varepsilon$  is the voidage fraction of the wet granular material.

In the capillary state, the liquid fills all the space between particles and the force to hold the particles together is only produced from the capillary pressure,  $P_c$ , at the agglomerate surface (Pierrat and Caram, 1997). The tensile strength is given by Schubert (Pierrat and Caram, 1997) as:

$$T_{S,capillary} = SP_c, \quad \text{Eq. 1.18}$$

where  $P_c$  is the capillary pressure and is given as:

$$P_c = a' \frac{1 - \varepsilon}{\varepsilon} \frac{\gamma}{d}, \quad \text{Eq. 1.19}$$

where  $a'$  is a dimensionless factor, which depends on the granular bed rearrangement, ranging between 6 and 8 (Saleh and Guigon, 2009).  $S$  is the liquid saturation, which is defined as the volume of liquid divided by the volume of void in the granular material and expressed as:

$$S = \frac{1 - \varepsilon}{\varepsilon} \frac{V_L}{V_S}, \quad \text{Eq. 1.20}$$

where  $V_L$  and  $V_S$  are the volume occupied by the liquid in the granular material and the volume of solid respectively.

In the funicular state, the tensile strength is estimated from those obtained in the pendular state and the capillary state. Indeed, zones with liquid bridges and zones completely saturated with liquid coexist in the funicular regime (Pierrat and Caram, 1995). Therefore, the capillary force arises from the liquid bridge forces and the capillary pressure. The tensile strength in the funicular regime is expressed as:

$$T_{S,funicular} = T_{S,capillary} \frac{S_2 - S}{S_2 - S_1} + T_{S,pendular} \frac{S - S_1}{S_2 - S_1}, \quad \text{Eq. 1.21}$$

where  $S_1$  is the limit saturation between the pendular and the funicular states and  $S_2$  is the limit saturation between the funicular and the capillary states.

#### 1.4.4. Stresses and shear tests

##### 1.4.4.1. Stresses and Mohr-circles

The granular material is now considered at a macroscopic scale as a continuum media. In order to analyse the stresses applied to the granular media, we consider a finite elementary volume, represented as a cube in the example given in Fig. 1.9-left. The stress tensor can be divided into two components: normal stress and shear stress. Considering the principal directions, there are three principal stresses acting on the system, which are perpendicular to each other: the major principal stress  $\sigma_1$ , the minor principal stress  $\sigma_3$  and the intermediate principal stress  $\sigma_2$ . The system can be approximated in two dimensions since  $\sigma_2$  and  $\sigma_3$  are generally similar in magnitude (Nedderman, 1992). The elementary volume in two dimensions, with major and minor principal stresses acting on it, is illustrated in Fig. 1.9-right. The normal and shear stresses in any direction can be expressed using  $\sigma_1$ ,  $\sigma_3$  and the angle  $\theta$  between the inclined plane and the horizontal as:

$$\sigma_n = \frac{\sigma_1 + \sigma_3}{2} \pm \frac{\sigma_1 - \sigma_3}{2} \cos 2\theta, \quad \text{Eq. 1.22}$$

$$\tau = \frac{\sigma_1 - \sigma_3}{2} \sin 2\theta. \quad \text{Eq. 1.23}$$

The stresses at any point of an isotropic system is located in the Mohr circles represented on a graph given  $\tau$  as a function of  $\sigma$  (see Fig. 1.10). If the system has an inclination of an angle  $\theta$ , the stresses are obtained from the Mohr circles with an angle  $2\theta$  with an anti-clockwise rotation.

##### 1.4.4.2. Mohr-Coulomb criterion for granular material

The Mohr-Coulomb criterion defines the shear stress limit at a given normal stress, beyond which the granular material fails. The stress at failure, from Mohr-Coulomb criterion is given by this linear equation, which is another expression of Eq. 1.16:

$$\tau = \mu\sigma + c, \quad \text{Eq. 1.24}$$

where  $c$  is the cohesion, which is defined as the shear resistance at zero normal stress. The failure of the granular material is occurred if the line defined by the Mohr-Coulomb criterion is

tangent to the Mohr circles (Nedderman, 1992). The Mohr-Coulomb criterion can be constructed by drawing Mohr circles for various stress conditions (see Fig. 1.11). The data can be obtained from triaxial compression test and shear tests. However, the experimental data can have a curved shape instead of a straight line, especially for cohesive granular material. The parameters  $\mu$  and  $T_s$  (the tensile strength, see Eq. 1.16) can be determined at small stresses where the variation is linear (Mitarai and Nori, 2006).

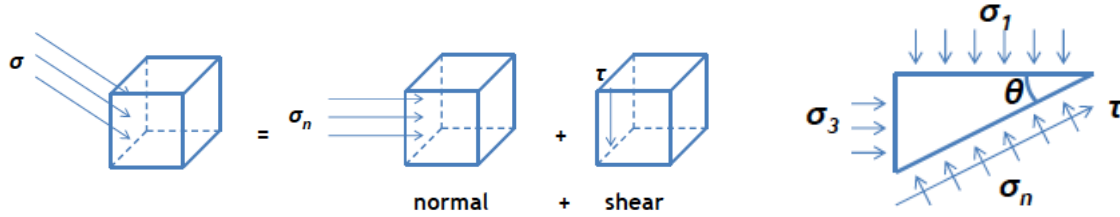


Fig. 1.9. Left, schema of a finite elementary volume of a granular material with stresses applied on it. Right, two dimensions representation of the elementary volume with the principal stresses  $\sigma_1$  and  $\sigma_3$  (Hare, 2015).

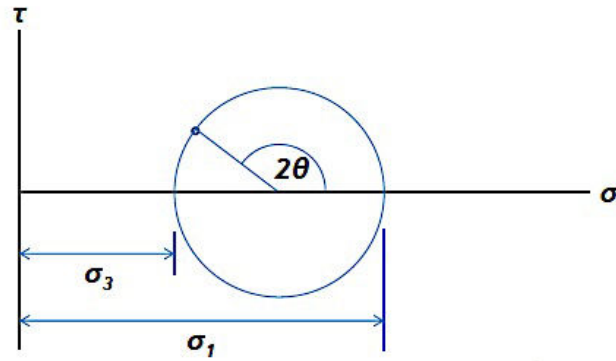


Fig. 1.10. Schema of Mohr circles defined by the two principal stresses  $\sigma_1$  and  $\sigma_3$  and the angle  $\theta$  (Hare, 2015).

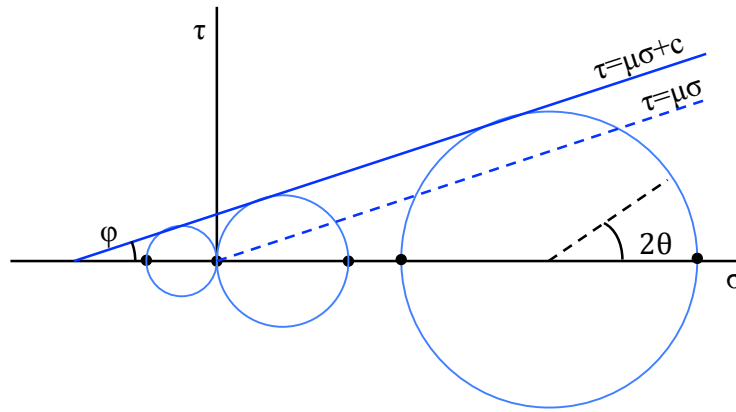


Fig. 1.11. Schema of Mohr circles and Mohr-Coulomb criterion for non-cohesive granular material (dashed line) and cohesive granular material (continuous line) (Mitarai and Nori, 2006).

#### 1.4.4.3. Flow properties of granular material

As mentioned above, shear testers can be used in order to characterise the flow properties of granular materials. Many shear testers and shear procedures have been developed. Among these testers, Jenike, Schulze and FT4 testers are well known and well used. They allow to control the shearing plane and the external forces applied to the granular material and provide straightforward measurement of the flow properties used for practical applications. However, it has been reported that the results obtained from the shear test depends on the shear testers and the shear procedure (Schwedes and Schulze, 1990).

In this subsection we present the principle of the shear test and the properties measured by the shear testers. Generally, the shear test consists of measuring the shear stress,  $\tau$ , of a granular material with normal stress,  $\sigma$ , applied on it. The measured shear stress depends on the preconsolidation stress,  $\tau_c$ , initially applied to the granular material sample and affects its bulk density. This step is necessary to obtain reproducible results. Running a shear test at a different normal stress, preceded by identical preconsolidation step, gives a maximum shear stress,  $\tau_s$ , observed by the peak in Fig. 1.12. The plot of  $\tau_s$  as a function of  $\sigma$  gives a curve called the “yield locus” and characterise the conditions that cause the flow of the granular material (Johanson, 2003). Increasing the preconsolidation load leads to increase the bulk density and, consequently, the yield locus changes; for the same normal stresses, higher shear stresses,  $\tau_s$ , are necessary to reach the yield locus (Schwedes and Schulze, 1990). The shear stress obtained at the plateau,  $\tau_D$ , can be also investigated. The impact of the consolidation on the  $\tau_D$  values is less relevant compared to  $\tau_s$ . The plot of  $\tau_D$  as a function of  $\sigma$  gives a curve called the “dynamic locus” and characterise also the steady-state flow (Collet, 2010). Moreover, the dynamic locus allows also to characterise the frictional interactions by determining the dynamic friction coefficient according to Coulombs’ law (See Eq. 1.24). In the following study we investigate the  $\tau_D$  values and will be denoted by  $\tau$ .

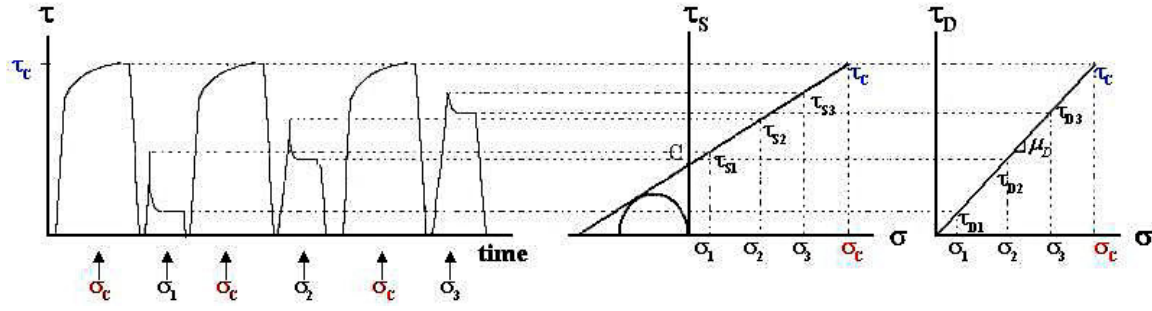


Fig. 1.12. Descriptive diagram of the shear test (Collet, 2010).

#### 1.4.5. Stick-slip motion

The stick-slip friction is a very common phenomenon occurred when two solids are sliding against each other (e.g., squeaking door or chalk on a blackboard). It is described as an alternative motion between sticking and sliding of the two surfaces in contact, inducing a friction force changes and leading to an oscillations with constant or varying frequency. During the sticking phase, the material accumulates the elastic energy of the system and then releases it during sliding as kinetic energy and accompanied by an acoustic energy in some cases (Robbins, 1999; Capone *et al.*, 1992). For the granular material, the stick-slip is occurred during powder handling such as emptying of silos or mixing. It is also observed and heard for the shear tests as a vibration of the apparatus, noise emission and instability of the signal. The stick-slip appears as a result of the characteristic of the apparatus and the granular material.

The stick-slip motion can be described by the movement of a body connected to a spring of a stiffness  $k$  and sliding over a horizontal plane at constant velocity,  $v$ , entrained by a tangential force  $F_t$  (see Fig. 1.13). The body is motionless while friction coefficient does not reach the maximum value  $\mu_s$ :

$$kx < \mu_s Mg, \quad \text{Eq. 1.25}$$

where  $x$  is the spring elongation and  $M$  is the mass of the body. Then, after the threshold is reached, the equation of motion is given as:

$$M\ddot{x} + kx = \mu_d Mg; (\mu_d < \mu_s). \quad \text{Eq. 1.26}$$

When the velocity is zero, the motion is again governed by the static friction coefficient  $\mu_s$  as:

$$kx = \mu_s Mg. \quad \text{Eq. 1.27}$$

Using this model, the stick-slip motion is represented by a sinusoidal signal with a pulse of  $\omega_0 = \sqrt{k/M}$  and a line segment (see Fig. 1.13). This description gives a simple analysis of the stick-slip motion, however experiments demonstrated the limitation of this model since the



static friction coefficient is also a time-dependent function and the dynamic friction coefficient depends on the velocity (Lubert, 2000). As mentioned above the stick-slip is observed for non-cohesive and cohesive granular material. In this study we will briefly discuss the effect of the liquid on the stick-slip signal in chapter 4.

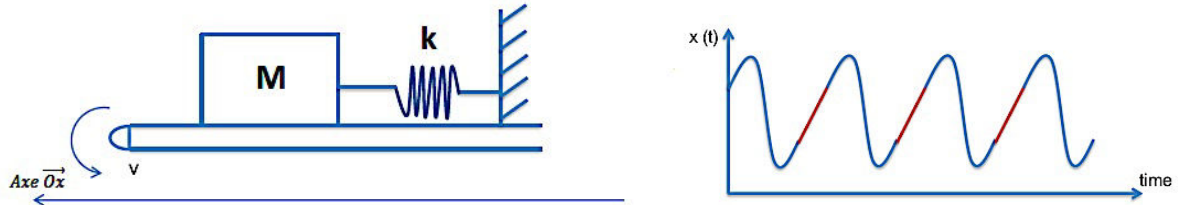


Fig. 1.13. Left, the stick-slip motion assimilated to the movement of a body pulled by a spring. Right, Representation of the stick-slip signal according to the model in Eq. 1.25 - Eq. 1.27. The signal is sinusoidal during sliding and linear during sticking.

## 1.5. Conclusions

The properties of the dry and wet granular materials have been briefly introduced in this chapter. Some other properties such as the deformation at the particle scale were not mentioned here but will be discussed in the next chapter regarding the discrete element method. The classic mechanical laws have been presented here but many other laws have been developed in the literature to characterise the granular material behaviour in certain situations and under certain conditions. We mainly limited this chapter to the mechanical laws that will be employed in this study.

### Conclusions (en Français)

Les propriétés des milieux granulaires secs et humides ont été brièvement présentées dans ce chapitre. D'autres propriétés telles que la déformation à l'échelle des particules n'ont pas été mentionnées ici, mais elles seront discutées dans le chapitre suivant concernant la méthode des éléments discrets. Les lois mécaniques classiques ont été présentées ici, mais d'autres lois spécifiques pour certaines situations et sous certaines conditions existent dans la littérature. Nous avons principalement limité ce chapitre aux lois mécaniques qui seront utilisées dans cette étude.

## References

- Adams, M.J. and Perchard, V., 1985. The cohesive forces between particles with interstitial liquid. *Ins. Chem. Eng. Symp.*, 91, 147-160.
- Albert, R., Albert, I., Hornbaker, D., Schiffer, P. and Barabasi, A., 1997. Maximum angle of stability in wet and dry spherical granular media. *Phys. Rev. E*, 56, R6271.
- Bocquet, L., Charlaix, E., Ciliberto, S. and Crassous, J., 1998. Moisture-induced ageing in granular media and the kinetics of capillary condensation. *Nature*, 396, 735-737.
- Collet, R., 2010. Critères de malaxabilités des milieux granulaires humides. Ph.D Thesis, University of Toulouse, Toulouse.
- Capone, G., d'Agostino, V., della Valle, S. and Guida, D., 1992. Stick-slip instability analysis. *Meccanica*, 27, 111-118.
- Fisher, R.A., 1926. On the capillary forces in an ideal soil; correction of formulae given by W. B. Haines. *J. Agr. Sci.*, 16, 492-505.
- Gras, J.P., 2011. Approche micromécanique de la capillarité dans les milieux granulaire : rétention d'eau et comportement mécanique. Ph.D Thesis, Université Montpellier II, Montpellier.
- Goldman, A.J., Cox, R.G. and Brenner, H., 1967. Slow viscous motion of a sphere parallel to a plane wall – I. motion through a quiescent fluid. *Chem. Eng. Sci.*, 22, 637-651.
- Hare, C., 2015. Bulk characterisation of powders. Course: powder charaterisaton chemical, physical and mechanical properties, University of Leeds, Leeds.
- Hornbaker, D., Albert, R., Albert, I., Barabasi, A. and Schiffer, P., 1997. What keeps sandcastles standing? *Nature*, 387, 765.
- Hotta, K., Takeda, K. and Linoya, K., 1974. The capillary binding force of a liquid bridge. *Powder Technol.*, 10, 231-242.
- Huntzicker, W.E., 2003. How newspapers reported a milling disaster 125 years ago. *Hennepin History*, 62, 18-34.
- Israelachvili, J.N., 1991. Intermolecular and surface forces. Academic Press, London.
- Iveson, S.M., 2002. Limitations of one-dimensional population balance models of wet granulation processes. *Powder Technol.*, 124, 219-229.
- Iveson, S.M., Litster, J.D., Hapgood, K. and Ennis, B.J., 2001. Nucleation, growth and breakage phenomena in agitated wet granulation processes: a review. *Powder Technol.*, 117, 3-39.
- Johanson, K., Rabinovich, Y., Moudgil, B., Breece, K. and Taylor, H., 2003. Relationship between particle scale capillary forces and bulk unconfined yield strength. *Powder Technol.*, 138, 13-17.
- Klein, N.S., Bachman, J., Aguado, A. and Toralles-Carbonari, B., 2012. Evaluation of the wettability of mortar component granular materials through contact angle measurements. *Cem. Concr. Res.*, 42, 1611-1620.
- Lian, G., Thornton, C. and Adams, M.J., 1998. Discrete particle simulation of agglomerate

impact coalescence. *Chem. Eng. Sci.*, 53, 138-147.

Lian, G., Thornton, C. and Adams, M.J., 1993. A theoretical study of the liquid bridge force between rigid spherical bodies. *J. Colloid Interface Sci.*, 161, 3381-3391.

Lubert, M., 2000. Aptitude à l'écoulement d'un milieu granulaire : exploitation des instabilités de cisaillement et évaluation de vieillissement. Ph.D Thesis, Université de Provence, Marseille.

Maugis, D., 1987. Adherence of elastomers: Fracture mechanics aspects. *J. Adhesion Sci. Technol.*, 1, 105-134.

Mazon, T.G., Levine, A.J., Ertas, D. and Halsey, T.C., 1999. The critical angle of wet sand piles. *Phys. Rev. E*, 60, R5044-R5047.

Mazzone, D.N., Tardos, G.I. and Pfeffer, R., 1986. The effect of gravity of the shape and strength of a liquid bridge between two spheres. *J. Colloid Interface Sci.*, 113, 544-556.

Mikami, T., Kamiya, H., and Horio, M., 1998. Numerical simulation of cohesive powder behavior in a fluidized bed. *Chem. Eng. Sci.*, 53, 1927-1940.

Milewski, J.V., 1987. Handbook of fillers and reinforcements for plastics. Van Nostrand-Reinhold Co, New York.

Mitarai, N. and Nori, F., 2006. Wet granular materials. *Adv. Phys.*, 55, 1-45.

Mizuno, M., Fukaya, A. and Jimbo, G., 1991. The estimation of packing characteristics by centrifugal compaction of ultrafine. *KONA Powder Part.* 9, 19-27.

Nedderman, R.M., 1992. Statics and kinematics of granular materials. Cambridge University Press, 352.

Newitt, D.M. and Conway-Jones, J.M., 1958. Contribution to the theory and practice of granulation. *Trans. Inst. Chem. Eng.*, 36, 422-442.

Onoda, G.Y. and Liniger, E.G., 1990. Random loose packings of uniform spheres and the dilatancy onset. *Phys. Rev. Lett.*, 64, 2727.

Pierrat, P. and Caram, H.S., 1997. Tensile strength of wet granular materials. *Powder Technol.*, 91, 83-93.

Pietsch, W., 1991. Size enlargement by agglomeration. John Wiley and Sons, Chichester.

Pietsch, W., 2002. Agglomeration process: phenomena, technologies, equipment. Wiley-VCH, Weinheim.

Pitois, O., Moucheront, P. and Château, X., 2000. Liquid bridge between two moving spheres: an experimental study of viscosity effects. *J. Colloid Interface Sci.*, 231, 26-31.

Robbins, M.O., 1999. Jamming, friction and unsteady rheology. *Cond-mat/9912337*.

Rumpf, H., 1962. The tensile strength of granules and agglomerates. *Intersci. Publ.*, 379-418.

Saleh, K. and Guigon, P., 2009. Mise en oeuvre des poudres – granulation humide : bases et théorie. *Techniques de l'ingénieur*, J2253 V1, 1-14.

Schulze, D., 2008. Powders and bulk solids: behavior, characterization, storage and flow. Springer-Verlag Berlin Heidelberg.

Schwedes, J. and Schulze, D., 1990. Measurement of flow properties of bulk solids. *Powder*

Technol., 61, 59-68.

Scott, G.D., 1962. Packing of spheres: Packing of equal spheres. *Nature*, 193, 465.

Scott, G.D. and Kilgour, D.M., 1969. The density of random close packing of spheres. *Brit. J. Appl. Phys.*, 2, 863-866.

Seville, J.P.K., Willett, C.D. and Knight, P.C., 2000. Interparticle forces in fluidisation: a review. *Powder Technol.*, 113, 261-268.

Tegzes, P., Albert, R., Paskvan, M., Barabasi, A., Vicsek, T. and Schiffer, P., 1999. Liquid-induced transitions in granular media. *Phys. Rev. E*, 60, 5823-5826.

Visser, J., 1989. An invited review: Van der Waals and other cohesive forces affecting powder fluidization. *Powder Technol.*, 58, 1-10.

Yang, R.Y., Zou, R.P. and Yu, A.B., 2000. Computer simulation of the packing of fine particles. *Phys. Rev. E.*, 62, 3900.

Yang, R.Y., Zou, R.P. and Yu, A.B., 2001. Effect of capillary force on the packing of particles: a numerical study. *Proc. 6<sup>th</sup> International Congress on Chemical Engineering*, Melbourne, Australia, paper 175.

Yang, R.Y., Zou, R.P. and Yu, A.B., 2003. Effect of material properties on the packing of fine particles. *J. Appl. Phys.*, 94, 3025.

Yu, A.B., Feng, C.L., Zou, R.P. and Yang, R.Y., 2003. On the relationship between porosity and inter-particle forces. *Powder Technol.*, 130, 70-76.

Yuan, Y. and Lee, T.R., 2013. Contact angle and wetting properties. *Surface science techniques*. In: Bracco, G. and Holst, B. ed. *Surface science techniques*. Springer-Verlag Berlin Heidelberg, 3-34.

Wakeman, R.J., 1975. Packing densities of particles with log-normal size distributions. *Powder Technol.*, 11, 297-299.

Willett, C.D., 1999. The micromechanics of wet particulate materials. Ph.D Thesis, University of Birmingham, Birmingham.



## Chapter 2. Introduction to the discrete element method (DEM)

---

### Résumé:

Dans ce chapitre, nous présentons une étude bibliographique de la méthode des éléments discrets. Cette méthode de simulation permet de simuler la dynamique d'un ensemble de particules moyennant la seconde loi de Newton. Les forces de contact, utilisées pour le calcul du mouvement de particules, sont obtenues à partir d'une légère interpénétration, autorisée par le modèle, et qui traduit une certaine déformation de la matière. Nous présentons ainsi différents modèles de force de contact : le Modèle de Hertz-Mindlin pour le contact élastique, le modèle de Thornton pour le contact élastique-plastique, le modèle de JKR pour le contact élastique avec adhésion, le modèle de Luding et le modèle de Pasha pour le contact élastique-plastique avec adhésion. Ces différents modèles impliquent l'utilisation de certains paramètres qui dépendent de la propriété de matériau dans la simulation. Ainsi, nous discutons l'influence de ces paramètres sur la simulation notamment, la raideur élastique, le coefficient de restitution, le coefficient de glissement et le coefficient de roulement.

### Abstract:

This chapter presents an introduction to the discrete element method. This method allows the study of the dynamic of a particle assembly using the Newton's second law of motion. The contact force involved in the computing of the particle motion is determined by allowing a slight interpenetration between particles, which expresses the deformation of the material. Different contact models will be given in this chapter: Hertz-Mindlin's model for elastic contact, Thornton's model for elasto-plastic contact, JKR's model for elastic adhesive contact, Luding's and Pasha's models for elasto-plastic and adhesive contact. These different models imply the use of some parameters, which depend on the material properties, such as the elastic stiffness, the restitution coefficient, the sliding friction and the rolling friction. Thus, the influence of these parameters on the simulation results is discussed.

## 2.1. Introduction

The discrete element method (DEM), called also the distinct element method, was introduced by Cundall (1971) and further developed by Cundall and Strack (1979). It is a numerical method to study the dynamics of particles. This method consists in considering the particles as individual bodies and the interactions in between as external forces acting on them. DEM gives a microscopic and macroscopic descriptions of the granular material behaviour. Two approaches are commonly used in DEM: soft sphere and hard sphere (Zhu *et al.*, 2007 and Zhu *et al.*, 2008). The soft-sphere method allows particles to slightly interpenetrate each other and the contact force are then calculated from the deformation at the contact (overlap). The dynamic of particles is then determined from these contact forces by using the Newton's second law of motion. In the hard-sphere method, the dynamic of particles is defined from a sequence of collisions. Only binary collision is allowed in this method with no sustained contact. This method is more accurate for rapid granular flow (Zhu *et al.*, 2007). On the contrary, the soft-sphere method has been extensively used to study different areas of the granular material handling processes such as (compaction, mixing, fluidization, hopper flow...). In this chapter, we focus on the soft-sphere approach. First, a general introduction of the principle of the discrete element method is given. Secondly, we present the equation of motion and some of the contact models, which are commonly used in the literature. Finally, we discuss some of the input parameters in the simulations.

## 2.2. Principle of DEM

DEM consists in evaluating the inter-particle forces based on the deformation of particles in contact between themselves and with the environment. This method is often used with spherical particles, dimensionally stable but allowed to slightly interpenetrate each other. The forces acting on the particles are calculated from the interpenetration (overlap). This unrealistic deformation of particles in contact was introduced because of the complexity of the real deformation. The movement of the particle assembly is obtained by solving the equation of motion applied to the individual particle, which depends on the overlap with neighbouring particles.

The algorithm of DEM can be summarised in 5 steps as shown in Fig. 2.1. First, an initialisation of positions, velocities and orientations of particles is required; this consists in identifying the geometry and the dynamic of the powder-handling system, positioning the particles numbered from 1 to  $n$  and specifying the particle properties (size, density, shear modulus...). The second step consists of detecting the contact between particles and calculating the overlap distance and the resulting contact forces. In the case of spherical particles the contact is identified if the sum of the radii of two particles is larger than the distance between the two centres of spheres. This step is costly in terms of CPU time and depends on the number of particles involved. The third and the fourth steps consist in calculating the forces and torques in play on each particle and to integrating the equation of motion in order to obtain the position of the particle on the next step. The last step consists in updating the list of neighbouring particles, which allows to reduce the possible contact between particle to a limited number of particle and, therefore, to reduce the computational time.

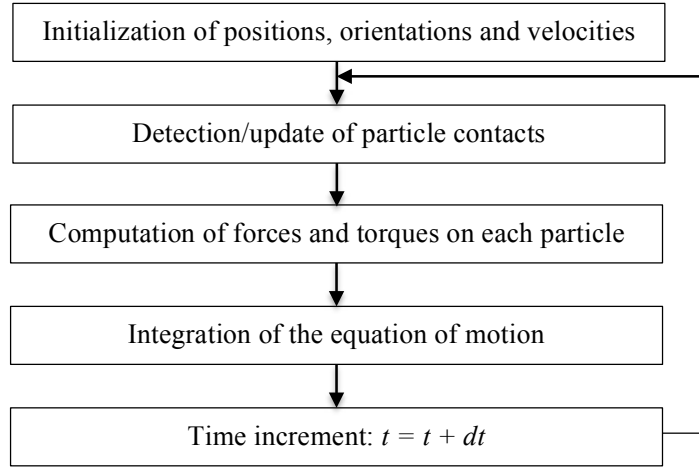


Fig. 2.1. Simple diagram to explicit the algorithm of DEM.

### 2.3. Equations of motion

The movement of the particle is obtained by integrating the Isaac Newton's second law of motion for translational and rotational degrees of freedom, given by the following equations:

$$m_i \frac{d^2 x_i}{dt^2} = F_i \text{ and } I_i \frac{d\omega_i}{dt} = \Gamma_i. \quad \text{Eq. 2.1}$$

The first term of Eq. 2.1 is the expression of the translational coordinate of particle motion, where  $m_i$  is the mass of the particle  $i$ ,  $x_i$  is its position and  $F_i$  is the total force exerted on it.  $F_i$  includes contact forces and external forces such as gravitational force as given by this relationship:

$$F_i = \sum_{j \neq i} F_{ij} + F_{ext,i}, \quad \text{Eq. 2.2}$$

where  $F_{ij}$  is the force exerted by the particle  $j$  on  $i$  and  $F_{ext,i}$  is the external force exerted on  $i$ .

The second term of Eq. 2.1 is the equation for the rotational coordinate of motion, resulting from the torque acting on the two particles at the contact point, with  $I_i$  is the particle mass moment of inertia,  $\omega_i$  is its angular velocity and  $\Gamma_i$  is the total torque acting on it due to rolling and torsion.

In order to solve the differential equation above we need to calculate the forces in play. Some of the contact force model will be given in the next sections.

### 2.4. Simulation time-step

The motion of one particle is not only affected by the direct mechanic contact with neighbours, but also by the Rayleigh waves due to the movement of the other particles far away. This wave



propagates through the surface of the particulate system and causes instability. In order to avoid this instability and to ensure realistic estimation of contact forces in play, the simulation time-step should be sufficiently shorter than the Rayleigh time-step in such a way that the disturbance of motion of particles propagates only to the nearest neighbours (Ning and Ghadiri, 2006). Therefore, the time-step is estimated as a percentage of the Rayleigh time. The latter is given by this equation (DEM-Solutions, 2015):

$$t_R = \frac{\pi R \left(\frac{\rho}{G}\right)^{1/2}}{0.1631\nu + 0.8766}, \quad \text{Eq. 2.3}$$

where  $R, \rho, G$  and  $\nu$  are, respectively, the particle radius, the density, the shear modulus and the Poisson's ratio. According to this relationship the Rayleigh time and hence the time-step is dependent on the particle properties; it increases by increasing the particle size and the density and decreases by increasing the shear modulus. For a heterogeneous particle assembly, the time-step should be the smallest among those obtained for different parameters, e.g. for polydisperse granular material, the time-step is calculated from the smallest radius.

## 2.5. Forces in DEM

The interactive forces between particles occur as a result of collisions or simple contact between each other (contact force). However, it is possible that interact between each other without physical contact (non-contact force). The contact and non-contact forces affect the motion of the single particle and have to be considered when evaluating forces in the equation of motion.

### 2.5.1. Non-contact forces

A brief introduction of the non-contact forces was given in the previous chapter such as electrostatic forces, Van-der-Waals forces, capillary forces and viscous force. These forces may manifest as attractive or repulsive interaction between particles and can be introduced as an additional force in some contact force models.

### 2.5.2. Contact forces

In order to express the contact forces, we consider two particles,  $i$  and  $j$ , in contact as shown in Fig. 2.2. The contact force  $F_{ij}$  is decomposed into two components:

$$F_{ij} = F_n n + F_t t, \quad \text{Eq. 2.3}$$

where  $F_n$  and  $F_t$  are the normal and tangential components respectively, and  $n$  and  $t$  are the unit vectors pointing in the normal and tangential directions respectively. These forces are calculated from the overlap of the two particles. The normal overlap denoted  $\delta_n$  is given by

$$\delta_n = (r_i + r_j) - |x_i - x_j|, \quad \text{Eq. 2.4}$$

where  $x_i$  and  $x_j$  are the centre positions of the particles  $i$  and  $j$  respectively, with  $r_i$  and  $r_j$  are their radii respectively. The particles are in contact if  $\delta > 0$  and it is assumed that it exists a repulsive force between particles. We introduce also the relative velocity of the point of contact as:

$$v_{ij} = v_j - v_i + \omega_j r_j - \omega_i r_i, \quad \text{Eq. 2.5}$$

where  $v_i$  and  $\omega_i$ , and  $v_j$  and  $\omega_j$  are the linear and angular velocities of particles  $i$  and  $j$ , respectively.

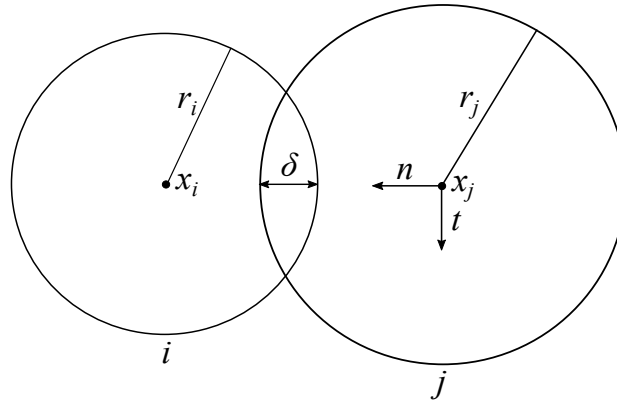


Fig. 2.2. Sketch of two particles  $i$  and  $j$  overlapped.

It exists many contact models in the literature to calculate the normal and tangential forces based on theories of contact mechanics. Following, we present some models given for different types of contact: elastic, elasto-plastic, elastic-adhesive and elasto-plastic-adhesive.

### 2.5.2.1. Elastic contact model

- **Linear spring-dashpot model**

This model gives a simple expression of the contact force between two soft spheres (Cundall and Strack, 1979). The contact force is decomposed into normal and tangential components as shown in Eq. 2.3. The normal component is given as the sum of an elastic force of contact and a force associated to the loss of kinetic energy or sometimes to the plastic deformation at contact, which may occur at high normal force. This model is assimilated to a system composed of a spring conservative force ( $F_n^S$ ) associated to a dashpot dissipative force  $F_n^D$  (see Fig. 2.3). The total normal contact force is given by this expression:

$$F_n = F_n^S + F_n^D = k_n^* \delta_n + D_n^* v_n \quad \text{Eq. 2.6}$$

where  $k_n^*$  is the normal stiffness spring coefficient and  $D_n^*$  is the normal damping coefficient. The superscript (\*) indicates that the value used is an equivalent value of the two particles in contact (see Appendix 2.1). The normal velocity is given by:

$$v_n = (v_{ij}n_{ij})n_{ij}, \quad \text{Eq. 2.7}$$

where  $n_{ij}$  is the normal unit vector along the contact line pointing from particle  $i$  to particle  $j$  (Helio and Neire, 2013).

The tangential component is given in analogy to the normal force component and with respect of Coulomb's friction criterion:

$$F_t = \begin{cases} k_t^* \delta_t + D_t^* v_t & , F_t < \mu F_n \\ \mu F_n & , F_t \geq \mu F_n \end{cases} \quad \text{Eq. 2.8}$$

where  $\delta_t$  is the tangential displacement between particles  $i$  and  $j$  (Garg *et al.*, 2012),  $\mu$  is the sliding friction coefficient. The relative tangential velocity is given as:

$$v_t = v_{ij} - v_n. \quad \text{Eq. 2.9}$$

The normal stiffness spring  $k_n$  and the normal damping coefficient  $D_n$  are expressed as:

$$k_n = \frac{m^*}{t_c^2} (\ln^2 e_n + \pi^2), \quad \text{Eq. 2.10}$$

$$D_n = -2\sqrt{m^* k_n} \beta, \quad \text{Eq. 2.11}$$

where  $\beta$  is defined as:

$$\beta = \frac{\ln e_n}{\sqrt{\ln^2 e_n + \pi^2}}, \quad \text{Eq. 2.12}$$

where  $e_n$  is the normal restitution coefficient,  $t_c$  is the collision duration and  $m^*$  is the equivalent mass. The calculation of the restitution coefficient and the collision duration can be found in this reference (Shäfer *et al.* (1996)).

The tangential stiffness coefficient is assumed to be  $k_t = 2/7 k_n$  (Shäfer *et al.* (1996)) and the tangential damping coefficient is assumed to be  $D_t = 1/2 D_n$  (Silbert *et al.* (2001)).

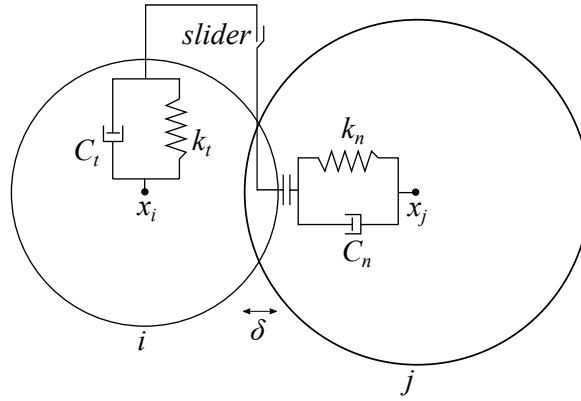


Fig. 2.3. Mapping of the linear normal contact model by means of a linear spring-dashpot model (reproduced from the schema given by Tagami and Horio (2003)).

- **Hertz-Mindlin model**

The Hertz-Mindlin model is a non-linear model based on the Hertzian contact theory (Hertz, 1882). In analogy to the linear spring-dashpot model, the normal force is given by:

$$F_n = F_n^S + F_n^D = k_n^* \delta_n^{3/2} + D_n^* v_n \quad \text{Eq. 2.13}$$

where the normal stiffness coefficient  $k_n$  and the normal damping coefficient are expressed as (Tsuji *et al.*, 1992):

$$k_n = \frac{4}{3} E^* \sqrt{r^*} \quad \text{Eq. 2.14}$$

$$D_n = -2 \sqrt{\frac{5}{6}} \beta \sqrt{2 E^* \sqrt{r^*} \delta_n m^*}, \quad \text{Eq. 2.15}$$

where  $E^*$  and  $r^*$  are the equivalent Young's modulus and the equivalent radius, respectively (see Appendix 2.2).

And the tangential contact force is expressed by:

$$F_t = \begin{cases} k_t^* \delta_t^{3/2} + D_t^* v_t & , F_t < \mu F_n \\ \mu F_n & , F_t \geq \mu F_n \end{cases} \quad \text{Eq. 2.16}$$

where the tangential stiffness coefficient  $k_t$  and the tangential damping coefficient are expressed as:

$$k_t = 8 G^* \sqrt{r^* \delta_n} \quad \text{Eq. 2.17}$$

$$D_t = -2 \sqrt{\frac{5}{6}} \beta \sqrt{k_t m^*} v_t, \quad \text{Eq. 2.18}$$

where  $G^*$  is the equivalent shear modulus (see Appendix 2.2).

The torque,  $\Gamma$ , is given as a function of the rolling friction coefficient,  $\mu_R$ , as follow (Zhou *et al.*, 1999):

$$\Gamma = \mu_R F_n X, \quad \text{Eq. 2.19}$$

where  $X$  is the distance between the centre of mass of the particle and the contact point.

### 2.5.2.2. Elasto-plastic contact model

Thornton's model (Thornton, 1997) gives the normal contact force of an elastic and plastic deformation at the contact between two spheres. The normal contact force is expressed differently at loading and unloading phases because of the hysteresis plastic deformation: During loading, the model follows Hertz equation up to a yield displacement after which the contact is plastically deformed and the normal force is given by a linear equation as follow:

$$F_n = k_n^* \delta_y + \pi p_y r^* (\delta_n - \delta_y), \quad \text{Eq. 2.20}$$

where  $k_n^*$  is the spring stiffness coefficient given by Eq. 2.14 and  $\delta_y$  is the yield displacement given by this equation:

$$\delta_y = \frac{\pi^2 r^*}{4 E^{*2}} p_y^2, \quad \text{Eq. 2.21}$$

where  $P_y$  is the contact yield stress, which can be measured experimentally from the yield stress  $\sigma_y$ , and it depends on the Poisson's ratio of the material (Rathbone, 2015; Johnson, 1985).

During unloading, the behaviour is assumed as elastic and the normal force follows the Hertz model again (see Fig. 2.4). However, to account for the flatterer occurred after the plastic deformation, the equivalent radius for the unloading contact,  $r_{un}^*$ , have to be calculated depending on the maximum force  $F_{max}$  and the maximum deformation  $\delta_{max}$ .

$$r_{un}^* = r^* \frac{k_n^* \delta_{max}^{3/2}}{F_{max}} \quad \text{Eq. 2.22}$$

The normal contact force, during unloading, is given by this equation based on Hertz model:

$$F_n = k_{un}^* (\delta - \delta_{min})^{3/2}, \quad \text{Eq. 2.23}$$

where  $k_{un} = 4/3 E^* \sqrt{r_{un}^*}$ , and  $\delta_{min}$  is the permanent plastic deformation given by

$$\delta_{min} = \delta_{max} \left( 1 - \frac{r^*}{r_{un}^*} \right). \quad \text{Eq. 2.24}$$

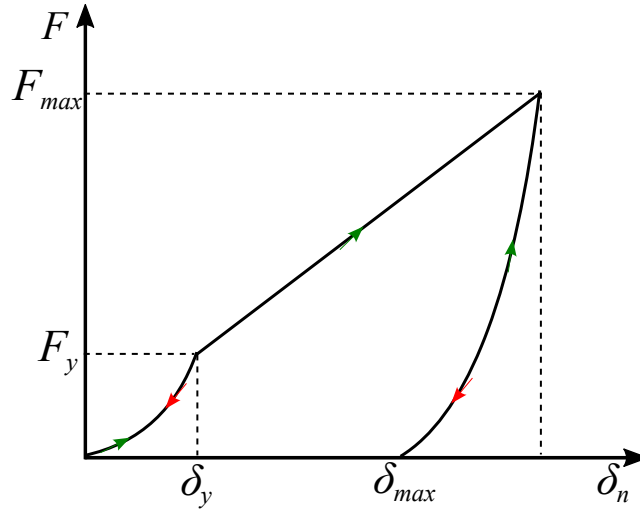


Fig. 2.4. Normal force – normal overlap diagram of Thornton's model (Thornton, 1997).

### 2.5.2.3. Elastic-adhesive contact model

- **JKR normal contact model**

This model introduced by Johnson, Kendall and Roberts (JKR) is based on the theory of Hertz extended to the case of two elastic-adhesive spheres. Another term, which gives the adhesive force, is added to the model of Hertz. The contact area considered by JKR model is larger than that considered by Hertz. The attractive forces are assumed to be located only in the contact area. Fig. 2.5 shows schematically the force – contact area relationship of JKR model. We can see that at the contact area, the normal force takes a certain value given by  $8/9 F_c$ , where  $F_c$  is the pull-of-force, i.e. the force necessary to separate the two particles attracted due to adhesion force and is given by (Johnson *et al.*, 1971):

$$F_c = \frac{3}{2} \pi r^* \gamma, \quad \text{Eq. 2.25}$$

where  $\gamma$  is the surface energy.

During loading, the spheres occur an elastic deformation at the contact area and the velocity decreases to reach zero at the maximum contact force. After that, the stored elastic energy is converted into kinetic energy and the spheres tend to reach their initial state at zero overlap. However, further work is required to separate the adhered spheres. The separation is obtained at a contact force equivalent to  $5/9 F_c$  (Johnson, 1985).

The normal contact force in JKR model is given as a function of the contact area as follow:

$$F_n = \frac{4E^* a^3}{3r^*} - \sqrt{8\pi\gamma E^* a^3}. \quad \text{Eq. 2.26}$$

The relationship between the contact area,  $a$ , and the normal overlap,  $\delta_n$ , is expressed as:

$$\delta_n = \frac{a^2}{r^*} - \sqrt{\frac{2\pi\gamma a}{E^*}}. \quad \text{Eq. 2.27}$$

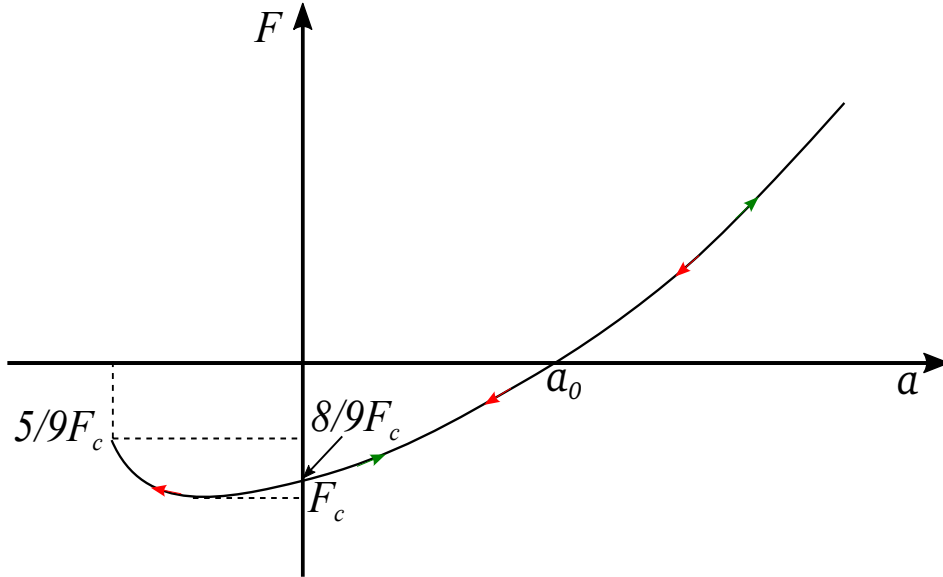


Fig. 2.5. Normal force – contact area diagram of JKR model (Johnson *et al.*, 1971).

- **Tangential model for elastic-adhesive contacts**

The tangential force may influence the normal force due to the tangential displacement induced (Savkoor and Briggs, 1977). Savkoor and Briggs demonstrated that the contact radius could be modified to take into consideration this tangential displacement

$$a^3 = \frac{3r^*}{4E^*} \left( F_n + 2F_c \pm \sqrt{4F_n F_c + 4F_c^2 - \frac{F_t^2 E^*}{4G^*}} \right), \quad \text{Eq. 2.28}$$

where  $F_t$  is the tangential force and can be evaluated from the elastic model described above.

The equation shows that the increase of the tangential force leads to reduce the contact area. Savkoor and Briggs assumed that this reduction is maybe due to a peeling phenomenon, which can be occurred during the tangential displacement. This phenomenon is completed when the tangential force reach a critical value,  $F_{tc}$ , given by:

$$F_{tc} = 4 \sqrt{\frac{(F_n F_c + F_c^2) G^*}{E^*}}. \quad \text{Eq. 2.29}$$

The contact area at the critical tangential force is then given as:

$$a^3 = \frac{3r^*}{4E^*}(F_n + 2F_{tc}). \quad \text{Eq. 2.30}$$

Savkooor and Briggs assumed that an increase of the tangential force beyond  $F_{tc}$  leads to reduce the contact area to the one given from the Hertzian equation:

$$a^3 = \frac{3r^*}{4E^*}F_n. \quad \text{Eq. 2.31}$$

Thornton and Yin (1991) considered that there is a smooth transition from peeling to sliding behaviour at the critical tangential force  $F_{tc}$ . They assumed that if  $F_{tc}$  is smaller than the tangential force required to cause a sliding between the two spheres, a micro-slip could be occurred. In this situation the tangential force is given as follow:

$$F_t = \mu(F_n + 2F_c) \left[ 1 - \left( 1 - \frac{\delta}{\delta_s} \right)^{\frac{3}{2}} \right], \quad \text{Eq. 2.32}$$

where  $\delta_s$  is given as:

$$\delta_s = 3\mu \frac{F_n + 2F_c}{16G^*a}. \quad \text{Eq. 2.33}$$

When the sliding is occurred, the tangential force is given as:

$$F_t = \mu(F_n + 2F_c). \quad \text{Eq. 2.34}$$

#### 2.5.2.4. Elasto-plastic and adhesive contact model

- **Luding's normal contact model**

As an alternative to the spring-dashpot model introduced above another so-called the linear hysteretic spring model, which take into consideration adhesive forces and elasto-plastic deformation that may occur at the contact between two spheres, was proposed by Luding *et al.* (2008). This model gives an expression of the normal force as follow:

$$F_n = \begin{cases} k_p \delta_n, & \text{loading} \\ k_e(\delta_n - \delta_0), & \text{un/reloading,} \\ -k_c \delta_n, & \text{unloading} \end{cases} \quad \text{Eq. 2.35}$$

Fig. 2.6 shows the normal force – normal overlap curves during loading and unloading paths. First, the initial normal force,  $F_0$ , takes a certain negative value when the two spheres come into contact due to the attractive forces (e.g. Van-der-Waals). During loading, a plastic deformation is considered at the contact area; a linear increase of the normal force with the overlap  $\delta$  is occurred, where  $k_p$  is the slope of the line. This curve defines the maximum force obtained for the maximum overlap  $\delta_{max}$ . During unloading, the force decreases linearly with the elastic stiffness  $k_e$ , to reach zero value at an overlap  $\delta_p$ . Reloading at any time leads to increase



the force along the line with slope  $k_e$  to the maximum value at  $\delta_{max}$  and then to follow again the line of slope  $k_p$  and  $\delta_{max}$  has to be adjusted again. Unloading below  $\delta_p$  leads to an attractive force until reaching the minimum force  $f_{cp}$ , at the minimum overlap  $\delta_{cp}$ . Further-unloading leads to reduce the attractive force following the adhesive branch with slope  $-k_c$ . Reloading for  $\delta < \delta_{cp}$ ,  $F_n$  follows a linear line parallel to the elastic line which demonstrates the hysteretic feature of this model.

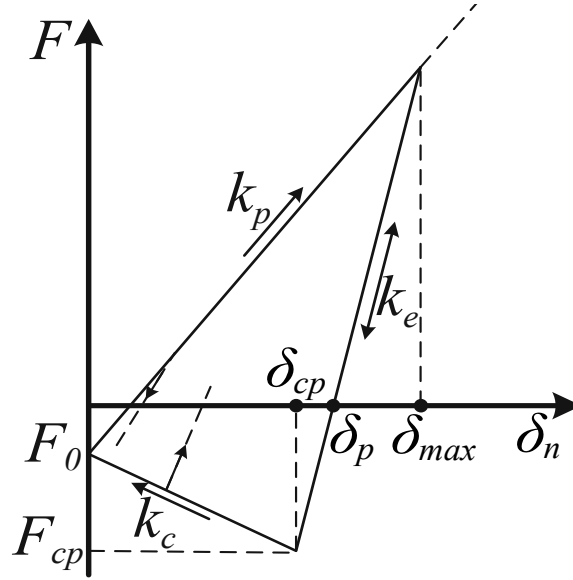


Fig. 2.6. Schematic diagram of the elasto-plastic and adhesive model of Luding (Luding, 2008).

- **Pasha's normal contact model**

Pasha *et al.* (2014) proposed an elasto-plastic and adhesive model based on the model of Luding (2008) and the model of Walton and Johnson (2009). Fig. 2.7 shows the normal force – normal overlap curves for loading and unloading paths. Initially, the contact force takes a negative value when the two spheres come into contact. This force is given by  $F_0 = 8/9 F_c$ , where  $F_c$  is the JKR pull-off force. During loading, the contact is plastically deformed following the line with slope  $k_p$ . The contact force is given by this equation:

$$F_n = k_p \delta_n - \frac{8}{9} F_c, \quad \text{Eq. 2.36}$$

During unloading, the contact is elastically deformed following the line with slope  $k_e$  and the contact force is given by this equation:

$$F_n = k_e (\delta_n - \delta_p), \quad \text{Eq. 2.37}$$

where  $k_e$  is the elastic stiffness and  $\delta_p$  is the plastic deformation reached when the force is zero (see Fig. 2.7). The unloading line continues until a pull-off force  $F_{cp}$  is reached at  $\delta_{cp}$ . For further unloading, the contact force follows the line with negative elastic stiffness and is given by this equation:

$$F_n = -k_e (\delta_n - 2\delta_{cp} + \delta_p). \quad \text{Eq. 2.38}$$

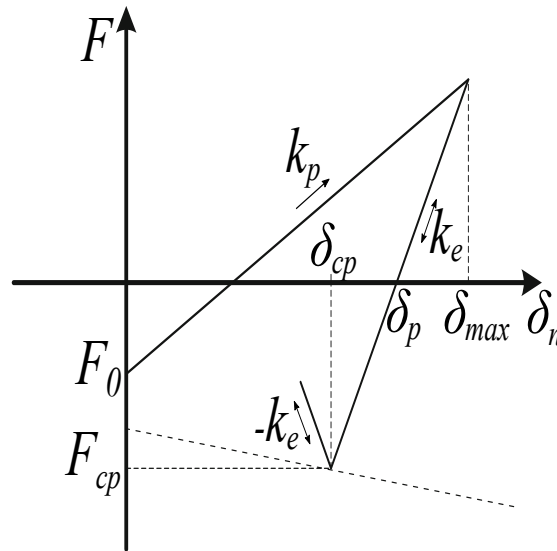


Fig. 2.7. Schematic diagram of the elasto-plastic and adhesive model of Pasha *et al.* (Pasha *et al.*, 2014).

- **Luding's tangential contact model**

The tangential force proposed by Luding (2008) is similar to the linear spring dashpot model. In order to account for the adhesion force into the tangential contact model, the limit of the tangential force is deduced by modifying the Coulomb's law considering a positive force contribution:

$$F_{t,limit} = \mu(F_n + F_c\delta_n). \quad \text{Eq. 2.39}$$

## 2.6. Input parameters for the simulation

As can be seen from the different models introduced above, the contact force expressions imply parameters, which depend on the material properties such as the Young's modulus, the restitution coefficient, the sliding friction and the rolling friction. These properties can be either estimated from theoretical models or measured experimentally and are used as input parameters for the simulation. In this section we discuss some of these parameters:

### 2.6.1. Contact stiffness

The elastic properties of the material (Young's modulus and Poisson's ratio) are used to calculate the contact stiffness (see Eq. 2.14 and Eq. 2.15). The stiffness plays an important role on impact collisions since it affects the normal overlap (Malone and Xu, 2008). It was observed that reducing the stiffness leads to increase the contact time in order to conserve the collision energy (Lommen *et al.*, 2014). The normal overlap increases as a result of the contact time increase and this may produce inaccurate results from the simulation. Lommen *et al.* (2014) have demonstrated that bulk properties such as bulk stiffness and bulk restitution can change as a result of the stiffness variation.

### 2.6.2. Coefficient of restitution

The restitution coefficient is defined as the ratio of the relative velocity before and after collision impact. It expresses the degree of conservation of kinetic energy after collision between particle – particle and particle geometry section in the simulation. This value is used to calculate the damping coefficient as it can be observed in Eq. 2.11 and Eq. 2.12. Weir and Tallon (2005) have reported that the coefficient of restitution is a function of the relative impact velocity and hence it is important to well estimate its value depending on the velocity for the simulation. However, it was observed that this coefficient is constant at relatively low velocity. The coefficient of restitution can be calculated experimentally by drop test experiments easy to perform. It can be also calibrated from the simulation by varying the input value if we have an idea about the expected results.

### 2.6.3. Coefficient of sliding friction

The sliding friction coefficient is defined as the ratio of the tangential force during sliding to the normal force. In the simulation, this parameter is involved in the calculation of the tangential force when the tangential stiffness exceeds the sliding friction coefficient (see Eq. 2.8). This means that if the tangential stiffness is high enough, the sliding friction may prevails

during most of the contact. Indeed this parameter is of crucial importance since it affects the shear stress magnitude and variation (Persson and Frenning, 2013). It is complicated to estimate the value of the sliding friction coefficient theoretically, since it depends on many of the material properties. It is, therefore, advisable to measure this value experimentally in order to be used as input parameter for the simulation.

#### **2.6.4. Coefficient of rolling friction**

The rolling friction is the resisting moment due to the rolling at the contact between particle – particle or particle – geometry. It depends on the material properties, the shape of particle and the contact surface. In the simulation, this parameter can be used to produce a rolling resistance of the sphere as a technique for modelling the particle shape in order to reduce the computational time (Wensrich and Katterfeld, 2012). Indeed, the rolling friction reduces the angular velocity by reducing the torque on particle during collision, which can be caused by the non-spherical shape or surface roughness of particles in real experiment (Bharadwaj *et al.*, 2010). It has been reported that the rolling friction coefficient has an impact on the stress at low packing fraction of the granular material in the simulation (Persson and Frenning, 2013).

### **2.7. Conclusions**

The chapter is an introduction to the discrete element method, which was used to study the behaviour of the granular material in my Ph.D. works. The different contact models presented in this chapter are intended to compare between them and to decide which one is suitable for our study. The Hertz-Mindlin model was chosen since it was successfully used in the simulation of glass beads in steady-state conditions in the literature. Moreover, this model is available in EDEM<sup>TM</sup>, which is the software used for our simulation. Another model, which implies the liquid bridge force, was also used to study the wet granular material behaviour. More details about this model will be presented in chapter 5.

### **Conclusions (en Français)**

Le chapitre est une introduction à la méthode des éléments discrets, qui a été utilisée pour étudier le comportement du milieu granulaire dans ce travail. Les différents modèles de contact présentés dans ce chapitre ont pour but de comparer et de décider lequel est approprié pour notre étude. Le modèle Hertz-Mindlin a été choisi car il a été utilisé avec succès dans la simulation de billes de verre en régime d'écoulement stationnaire. En outre, ce modèle est disponible dans EDEM<sup>TM</sup>, qui est le logiciel utilisé pour la simulation. Un autre modèle, impliquant les forces capillaires, a également été utilisé pour étudier le comportement du milieu granulaire humide. Plus de détails sur ce modèle seront présentés au chapitre 5.

## References

- Bharadwaj, R., Ketterhagen, W.R. and Hancock, B.C., 2010. Discrete element simulation study of a freeman powder rheometer. *Chem. Eng. Sci.*, 65, 5747-5756.
- Cundall, P.A., 1971. A computer model for simulating progressive, large-scale movements in blocky rock systems. *Proceedings of the international Symposium on Rock Mechanics*. Nancy, France, 129-136.
- Cundall, P.A. and Strack, O.D.L., 1979. A discrete numerical model for granular assemblies. *Geotechnique*, 29, 47-65.
- DEM\_Solutions, 2015. EDEM 2.7 User Guide. DEM Solutions Limited, Edinburgh, 1-133.
- Garg, R., Galvin, J., Li, T. and Pannala, S., 2012. Open-source Mfix-DEM software for gas-solids flows: Part I-Verification studies. *Powder Technol.*, 220, 122-137.
- Helio, P.N. and Meire, P.S.B., 2013. Linear and nonlinear Hertzian contact models for materials in multibody dynamics. 22<sup>nd</sup> international congress of mechanical engineering (COBEM), Ribeirao Preto, SP, Brazil.
- Hertz, H., 1882. Über die Berührung fester elastischer Körper. *J. für die reine und angewandte Mathematik*, 92, 156-171.
- Johnson, K.L., 1985. *Contact Mechanics*, Cambridge University Press, Cambridge, UK.
- Johnson, K.L., Kendall, K. and Roberts, A.D., 1971. Surface energy and the contact of elastic solids. *Proc. R. Soc. Lond. A*, 324, 301-313.
- Lommen, S., Schott, D. and Lodewijks, G., 2014. DEM speedup: Stiffness effects on behavior of bulk material. *Particology*, 12, 107-112.
- Luding, S., 2008. Cohesive, frictional powders: contact models for tension. *Granular Matter* 10, 235-246.
- Malone, K.F. and Xu, B. H., 2008. Determination of contact parameters for discrete element method simulations of granular systems. *Particology*, 6, 521-528.
- Ning, Z. and Ghadiri, M., 2006. Distinct element analysis of attrition of granular solids under shear deformation. *Chem. Eng. Sci.*, 61, 5991-6001.
- Pasha, M., Dogbe, S., Hare, C., Hassanpour, Ali. and Ghadiri, M., 2014. A linear model of elasto-plastic and adhesive contact deformation. *Granular Matter*, 16, 151-162.
- Persson, A. and Frenning, G., 2013. The influence of rolling friction on the shear behaviour of non-cohesive pharmaceutical granules – An experimental and numerical investigation. *Eur. J. Pharm. Sci.*, 49, 241-250.
- Rathbone, D., Marigo, M., Dini, D. and van Wachem, B., 2015. An accurate force-displacement law for the modelling of elastic-plastic contacts in discrete element simulations. *Powder Technol.*, 282, 2-9.
- Savkoor, A.R. and Briggs, G.A.D., 1977. The effect of tangential force on the contact of elastic solids in adhesion. *Proc. R. Soc. Lond. A*, 356, 103-114.
- Shäfer, J., Dippel, S. and Wolf, D.E., 1996. Force schemes in simulations of granular

materials. *Journal de Physique I France*, 6, 5-20.

Silbert, L.E., Ertas, D., Grest, G.S., Halsey, T.C., Levine, D. and Plimpton, S.J., 2001. Granular flow down an inclined plane: Bagnold scaling and rheology. *Phys. Rev. E*, 64, 051302.

Tagami, N. and Horio, M., 2003. A computational study of fluidized beds with particle size distribution. The second Asian particle technology symposium (APT 2003), Penang, Malaysia.

Thornton, C., 1997. Coefficient of restitution for collinear collisions of elastic-perfectly plastic spheres. *J. Appl. Mech.*, 64, 383-386.

Thornton, C. and Yin, K.K., 1991. Impact of elastic spheres with and without adhesion. *Powder technol.*, 65, 153-166.

Tsuji, Y., Tanaka, T. and Ishida, T., 1992. Lagrangian numerical simulation of plug flow of cohesionless particles in a horizontal pipe. *Powder Technol.*, 71, 239-245.

Walton, O.R. and Johnson, S.M., 2009. Simulating the effects of interparticle cohesion in micron-scale powders. *AIP Conf. Proc.*, 1145, 897-900.

Weir, G. and Tallon, S., 2005. The coefficient of restitution for normal incident, low velocity particle impacts. *Chem. Eng. Sci.*, 60, 3637-3647.

Wensrich, C. M. and Katterfeld, A., 2012. Rolling friction as a technique for modelling particle shape in DEM. *Powder Technol.*, 217, 409-417.

Zhou, Y.C., Wright, B.D., Yang, R.Y., Xu, B.H. and Yu, A.B., 1999. Rolling friction in the dynamic simulation of sandpile formation. *Physica A: statistical mechanics and its applications*, 269, 536-553.

Zhu, H.P., Zhou, Z.Y., yang, R.Y. and Yu, A.B., 2007. Discrete particle simulation of particulate systems: Theoretical developments. *Chem. Eng. Sci.*, 62, 3378-3396.

Zhu, H.P., Zhou, Z.Y., yang, R.Y. and Yu, A.B., 2008. Discrete particle simulation of particulate systems: A review of major applications and findings. *Chem. Eng. Sci.*, 63, 5728-5770.

## Appendices

### Appendix 2.1. Equivalent stiffness coefficient and damping coefficient

The normal equivalent stiffness coefficient,  $k_n^*$ , and the tangential equivalent stiffness coefficient,  $k_t^*$ , of two particles  $i$  and  $j$ , respectively, is given as follow:

$$k_n^* = \frac{k_n^i k_n^j}{k_n^i + k_n^j},$$

$$k_t^* = \frac{k_t^i k_t^j}{k_t^i + k_t^j},$$

where  $k_n^i$  and  $k_n^j$  are the normal stiffness coefficients and  $k_t^i$  and  $k_t^j$  are the tangential stiffness coefficient of the particles  $i$  and  $j$ , respectively.

The normal equivalent damping coefficients,  $D_n^*$ , and the tangential equivalent damping coefficient,  $D_t^*$ , of two particles  $i$  and  $j$ , respectively, is given as follow:

$$\frac{1}{D_n^*} = \frac{1}{D_n^i} + \frac{1}{D_n^j},$$

$$\frac{1}{D_t^*} = \frac{1}{D_t^i} + \frac{1}{D_t^j},$$

where  $D_n^i$  and  $D_n^j$  are the normal damping coefficients and  $D_t^i$  and  $D_t^j$  are the tangential stiffness coefficients of the particles  $i$  and  $j$ , respectively.

### Appendix 2.2. Equivalent radius, mass, Young's modulus and shear modulus

In the case of contact between two materials with different properties such as the particle size and the mechanic properties, an equivalent value can be used.

The equivalent radius,  $r^*$ , is calculated as:

$$\frac{1}{r^*} = \frac{1}{r_i} + \frac{1}{r_j},$$

where  $r_i$  and  $r_j$  are the radii of particles  $i$  and  $j$ , respectively. For a contact between particle and geometry section, the radius of the geometry takes an infinite value.

The equivalent mass,  $m^*$ , is calculated as:

$$\frac{1}{m^*} = \frac{1}{m_i} + \frac{1}{m_j},$$

where  $m_i$  and  $m_j$  are the masses of particles  $i$  and  $j$ , respectively. For a contact between particle and geometry section, the mass of the geometry takes an infinite value.

The equivalent Young's modulus,  $E^*$ , is given by this equation:

$$\frac{1}{E^*} = \frac{1 - \nu_i^2}{E_i} + \frac{1 - \nu_j^2}{E_j},$$

where  $E_i$  and  $E_j$  are the Young's modules of particles  $i$  and  $j$ , respectively, and  $\nu_i$  and  $\nu_j$  are the Poisson's ratios of particles  $i$  and  $j$ , respectively.

The equivalent shear modulus,  $G^*$ , is given by this equation:

$$\frac{1}{G^*} = \frac{E_i}{2(1 + \nu_i)} + \frac{E_j}{2(1 + \nu_j)},$$

where  $G_i$  and  $G_j$  are the shear modules of particle.





## Chapter 3. Materials and methods

---

### **Résumé:**

Ce chapitre présente les matériels et méthodes utilisés pour caractériser les propriétés de milieu granulaire et de liquide. Le dispositif du test de cisaillement et la méthode utilisée pour étudier le comportement au cisaillement de milieu granulaire humide sont décrits. Les techniques pour mesurer les paramètres d'entrée pour la simulation en se basant sur des matériaux modèles sont aussi décrites.

### **Abstract:**

In this chapter, the materials and methods used to characterise the granular material and liquid properties are presented. The shear test device and method used to study the shear behaviour of dry and wet granular materials is described. The techniques used to obtain the input parameters for the simulation based on model materials are also described.

### 3.1. Materials and characterisations

#### 3.1.1. The granular materials

The material used in this study consists of glass beads provided by Sovitec<sup>®</sup>. The glass beads are used in the experiments as supplied without any surface treatments but sieved to obtain narrow size distributions. Two different sizes of glass beads were used in the experimental part of the study (chapter 4): 70-110  $\mu\text{m}$  and 12-40  $\mu\text{m}$  in diameter. These sizes are chosen relatively small to enhance the effect of the capillary forces vis-a-vis the gravitational forces. The characterisation of the glass beads properties will be discussed in the next section. Another size of glass beads of 2 mm  $\pm$  0.2 in diameter, from Verrerie Villeurbannaise, was used for experiments in chapter 5. The glass beads were used to provide the input parameters for the simulations and to compare the results of the shear test from experiments with that from simulations. The size of particles was chosen relatively large in order to gain in the computational time and to facilitate the characterisation at the particle scale. Some experimental analysis of these glass beads, such as the mechanical properties and the sliding friction of particle, will be given next.

#### 3.1.2. Characterisation of the granular materials

##### 3.1.2.1. The density

The true density of the granular material  $\rho_s$  was measured using helium pycnometer AccuPyc II 1330 Micromeritics<sup>®</sup>. The technique consists of measuring the volume occupied by the particles inside a chamber using the gas displacement method. Knowing the mass of the sample,  $m$ , the true density,  $\rho_s$ , can be calculated as:

$$\rho_s = \frac{m}{V_s}, \quad \text{Eq. 3.1}$$

where  $V_s$  is the volume of the solid, which excludes the volume of pores in the sample.

The apparent density  $\rho$  was calculated by measuring the volume occupied by a given mass of glass beads in the measurement shear cell of the FT4 Powder Rheometer<sup>®</sup>. The apparent density is determined from the mass and the apparent volume,  $V_a$ , as:

$$\rho = \frac{m}{V_a}. \quad \text{Eq. 3.2}$$

The FT4 device allows measuring the apparent density for a controlled normal stress applied to the glass beads sample, which gives more precise measurement of the density compared to the shear cell of Schulze. Fig. 3.1 shows the procedure used to measure the density of the glass beads. The idea is to perform measurements for conditions similar to the granular material under shearing. The glass beads sample is first poured into the measurement cell and the granular bed is homogenized using the blade in order to get rid of large gaps, which can be occurred during filling, especially in the case of wet samples (see step 1 and 2 in Fig. 3.1). Next, the required normal stress is applied to the granular bed (Step 3). Finally, the apparent

volume is measured during shearing while the applied normal stress is maintained constant (step 4). We use the apparent volume obtained at steady-state to calculate the apparent density. This apparent density has been measured for two different normal stresses: low at 1 kPa and high at 12 kPa. We performed measurements of the density for dry and wet glass beads in order to study the variation of the voidage fraction with the liquid fraction increasing.

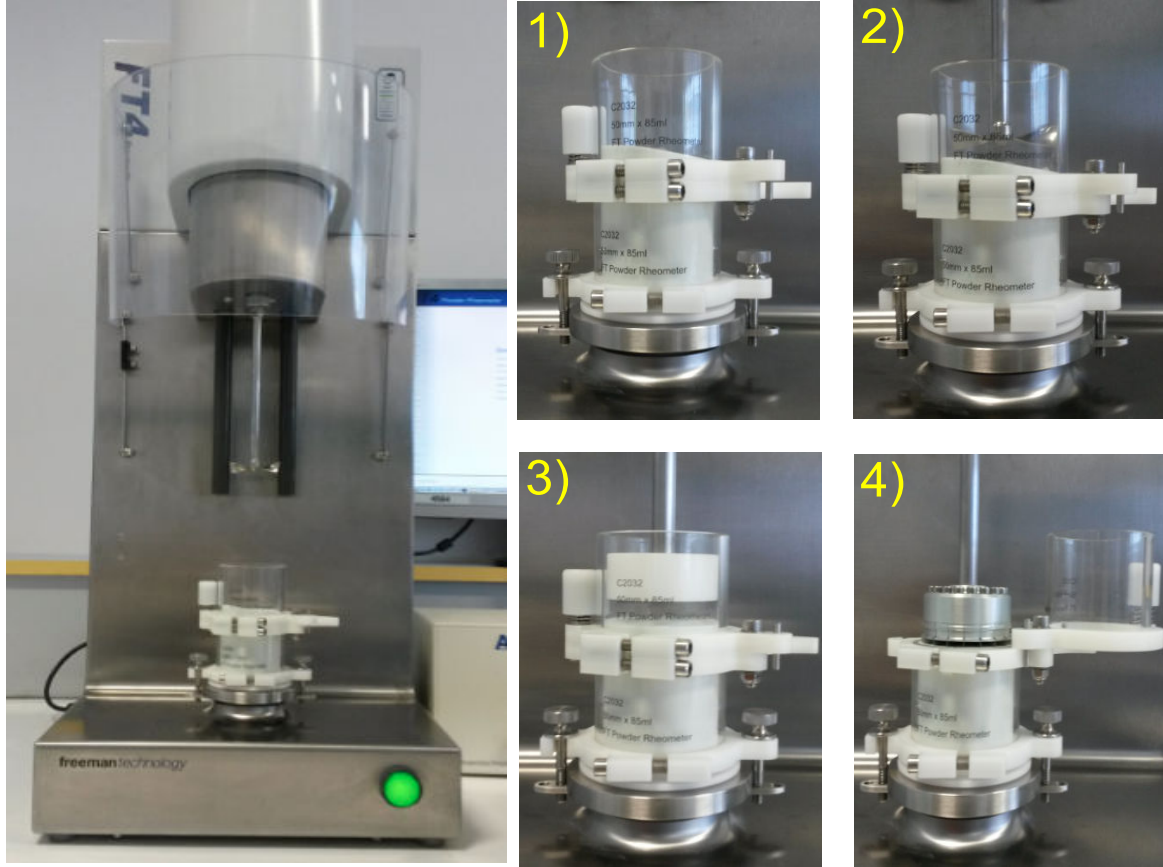


Fig. 3.1. Measurements of the apparent density of glass beads for different applied normal stresses using Freeman Technology FT4.

### 3.1.2.2. The voidage fraction

The voidage fraction is calculated from the true density and the apparent density at different normal stress applied to the granular material. In the dry case, the voidage fraction is calculated as:

$$\varepsilon = 1 - \frac{\rho}{\rho_s}. \quad \text{Eq. 3.3}$$

For the wet case, the volume occupied by the liquid is also considered and the expression of the wet voidage fraction will be introduced and discussed in the next chapter.

The X-ray tomography is a potential technique for the analysis of the bulk properties of a granular material, in particular the voidage fraction. This technique allows by image analysis not only to estimate the voidage fraction but also to get information about the distribution of the voids in the granular bed, in particular for cohesive powder. The analysis of the glass beads of 70-110  $\mu\text{m}$  was performed using Phoenix Nanoatom<sup>®</sup> X-ray tomography, CIRIMAT, Toulouse. A sample of glass beads was putted in a small transparent gelatine capsule of 6 mm in diameter and manually slightly packed to avoid large gaps due to the filling process. We performed analysis of the glass beads 70-110  $\mu\text{m}$ , dry and wet, with different liquid fractions. The use of the PEG 400 as a liquid to wet the glass beads was an advantage since it was detected in this analysis. The technique allows to achieve a large number of radiography in different angle of the sample and to combine them in order to obtain a 3D construction of the sample. This requires the use of software capable of processing such a large number of images in a reasonable time. In this study, the voidage fraction was analysed from the 2D radiography and the images were treated using Matlab<sup>®</sup>. Different images, representing different sections of the sample, were treated to estimate an average value of the voidage fraction. Further information of the image analysis will be given in chapter 4.

### **3.1.2.3. The particle surface analysis**

The surface of the glass beads, as supplied, was observed using two techniques: the Scanning Electron Microscope (SEM) and the Atomic-Force Microscopy (AFM). The SEM images of the glass beads 12-40  $\mu\text{m}$  and 70-110  $\mu\text{m}$  show a rough surface. The observed roughness is caused by the impurities adhered to the surface and also due to manufacturing defects in the form of microscopic cavities or bumps. Several SEM observations were performed in order to measure the size of the asperities. From the obtained images (see Fig. 3.2), an average height of the asperities is observed to be in the range of 1 to 2  $\mu\text{m}$ . The AFM allows analysing the surface roughness by measuring the interactive forces between the AFM cantilever (a force tensor) and the surface of the sample. The measurements were performed with a Raman-AFM microscopy, alpha300 RA, WITec GmbH, in GALA platform. A number of glass beads were glued to a glass microscope slide and the roughness of the free surface of beads was measured using contact mode. Similar values to the one estimated by SEM were also obtained from AFM. We consider an average value of  $1.5 \pm 0.5 \mu\text{m}$ . The analysis was performed to have an idea about the surface roughness of the glass beads used for experiment, since it may affect the capillary forces at low liquid content. Moreover, the formations of liquid bridges are also affected by the surface roughness and some models to estimate the capillary forces require the estimation of the size of asperities.

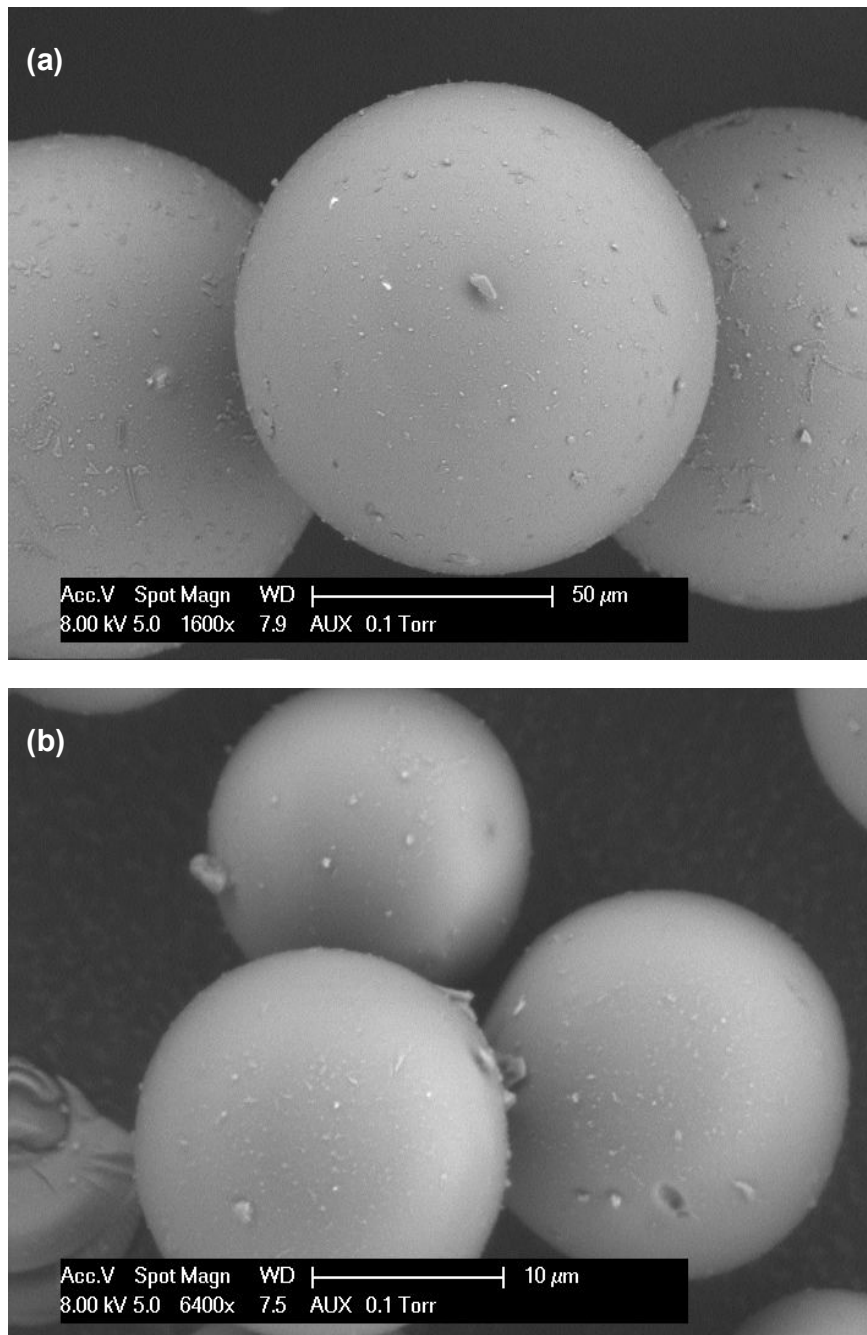


Fig. 3.2. Electron microscope scan images of the glass beads showing the asperities on the particle surface. (a) 70-110  $\mu\text{m}$  glass beads and (b) 12-40  $\mu\text{m}$  glass beads.

### 3.1.3. Wetting the granular material

The glass beads were wetted using Polyethylene glycol of 400 g molar weight (PEG 400) provided by Alfa Aesar. This liquid has been chosen since it wets well the glass beads and has also a low volatility compare to water, which helps to work with small liquid fractions with small risk of evaporation of liquid. The characteristics of the PEG 400 are given in Table 3.1

and the measurement methods are given in the next section. The polyethylene glycol is also slightly hygroscopic, non-toxic and non-hazardous.

The glass beads were mixed with various quantities of PEG 400, using a Kenwood planetary mixer (see Fig. 3.3). The procedure of mixing is really important since it can affect the distribution of liquid in the granular material, in particular at low liquid fraction. However, the mixing is not the focus of this study. Though, we ensure that the liquid and the glass beads were mixed for enough time and in a similar manner for all samples. The fraction of liquid is expressed as a volume ratio ( $V_R\% = \text{volume of liquid} / \text{total volume of particles}$ ). The fractions of liquid investigated in this study vary from 0.01% to 20% for the partially state of saturation, so-called pendular state. It is increased then from 20% to 60% in order to investigate more saturation states (funicular and capillary states).

Table 3.1. Properties of polyethylene glycol 400: density, viscosity, surface tension and angle of contact with the glass beads.

Properties of PEG 400	Values
Density ( $\text{g/cm}^3$ ) at 20°C	1.128
Viscosity (mPa.s) at 25°C	99.01
Surface tension (mN/m) at 23.5 °C	56.74
Angle of contact (°) (with the glass beads)	0



Fig. 3.3. Kenwood planetary mixer used to mix the glass beads with the PEG 400.

### 3.1.4. Characterisation of the liquid

#### 3.1.4.1. The surface tension

The surface tension of PEG 400 was measured based on Wilhelmy plate method, using a Tensiometer K12, Krüss®. This method consists of measuring the force exerted by the

meniscus formed at the interface of a vertically suspended plate touching the surface of the liquid. This force is related to the surface tension of the liquid according to this equation (Denis, 1997):

$$F_m = 2l\gamma_L, \quad \text{Eq. 3.4}$$

where  $F_m$  is the force exerted by the meniscus,  $l$  is the wetted length of the plate and  $\gamma_L$  is the surface tension of the liquid.

#### 3.1.4.2. The viscosity

The viscous force plays an important role in the wet granular material behaviour. A relatively low viscous liquid is chosen here since we are focusing on the capillary forces. Moreover, the experimental shear test is performed at low rotational speed of the shear cell, which limits the effect of the viscosity. The dimensionless capillary number ( $C_a = \mu v / \gamma$ ) can be used to compare the viscous effect to the capillary effect. In the case of PEG 400, with a surface tension of 56.74 mN/m, a dynamic viscosity of 99.01 mPa.s (Han *et al.*, 2008) and an approximated value of the velocity of particles taken as the rotational velocity of the shear cell (0.0005 m/s), the capillary number is estimated to be less than 0.01. This demonstrates that the capillary force prevails over the viscous force.

#### 3.1.4.3. The contact angle

The contact angle characterises the wettability of a material by a liquid. The contact angle of PEG 400 in the glass beads was evaluated using the drop shape analyser DSA30, Krüss®. This method consists of depositing a droplet of liquid on the granular bed and following the kinetics of the contact angle. A large contact angle was observed at first contact of the droplet with the surface of the granular bed (about 122°), but this angle rapidly drop to 0° when the liquid covers the surface of the beads.

The wettability of the PEG 400 to the glass beads was also analysed from SEM observations. Fig. 3.4 displays the surface of two glass beads of 2 mm in diameter wetted with small quantity of PEG 400 (VR = 1%). It can be observed that the liquid wets well the glass beads since it is spread on the surface.



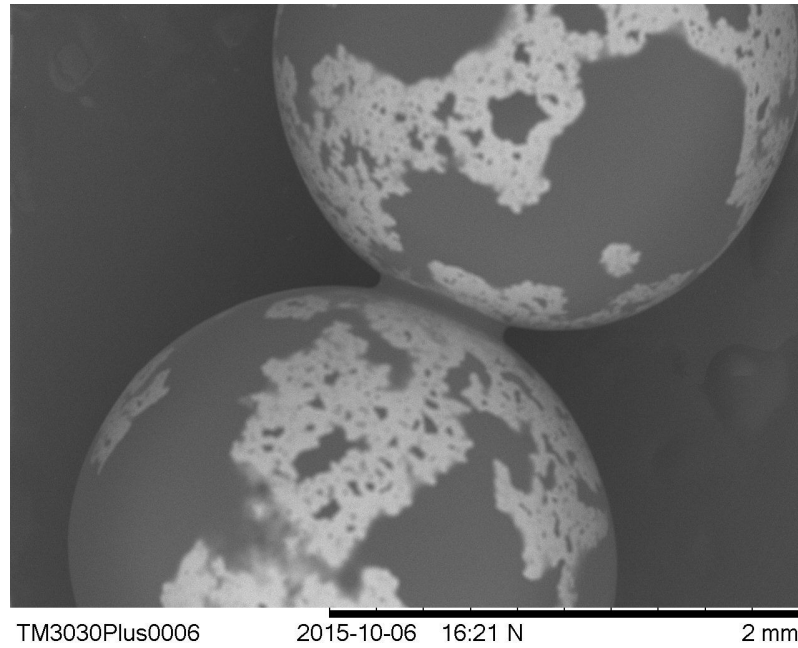


Fig. 3.4. Surface of two glass beads of 2 mm in diameter wetted with polyethylene glycol 400 for small liquid fraction ( $V_R = 1\%$ ).

## 3.2. Characterisation of the flow behaviour of the granular material

### 3.2.1. The angle of repose

The reduction of the size of particle can increase the cohesion due to the Van-der-Waals forces in play. The increase of the cohesion of the granular material can be observed by looking at the angle of repose. We performed measurements of the angle of repose for the glass beads 70-110  $\mu\text{m}$  and 12-40  $\mu\text{m}$  in the dry case using the Hosokawa Powder Tester PT-N. The test consists in pouring the powder through a funnel with an outlet of 5 mm over a support of 12 cm diameter. After avalanches, the angle of repose of the heap can be measured. Fig. 3.5 shows a relatively small angle of repose for the glass beads 70-110  $\mu\text{m}$  with well-shaped surface of the heap. However, an irregular shape of the glass beads heap of 12-40  $\mu\text{m}$  is observed. The measured values of the angle of repose are given in Table 3.2. We observe an increase of the angle of repose for the smaller beads and hence the estimated static friction is higher.

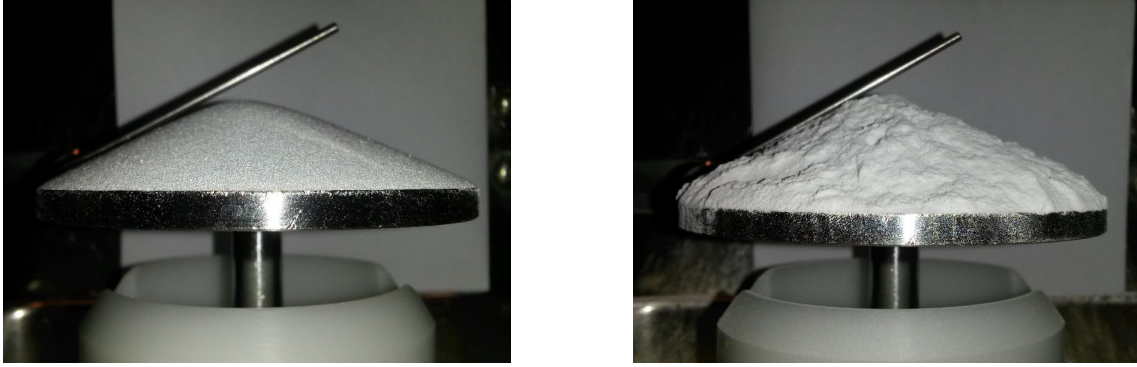


Fig. 3.5. Measurements of the angle of repose of dry glass beads using Hosokawa tester. (Left) glass beads of 70-110  $\mu\text{m}$  and (right) glass beads of 12-40  $\mu\text{m}$ .

Table 3.2. Values of the angle of repose and the static friction coefficient from Hosokawa test.

Glass beads	Angle of repose	Static friction coefficient
70-110 $\mu\text{m}$	24.5°	0.46
12-40 $\mu\text{m}$	30.4°	0.58

### 3.2.2. The shear test in steady-state conditions

Schulze shear cell was used to study the flow properties of dry and wet glass beads (see Fig. 3.6). This equipment consists of an annular chamber with an inner diameter of 10 cm and an outer diameter of 20 cm. Normal force  $N$  is applied through an annular lid, so as to exert a normal stress. A counterweight system exerts an against force  $F_A$  is used to balance the weight of the lid and other parts connected to it in order to be able to apply low normal stresses (Schulze, 2008). A smaller shear cell was used in chapter 5 for the experimental and the simulated study in order to speed up the simulation by reducing the number of particles. This shear cell has an annular chamber with an inner diameter of 6 cm and an outer diameter of 12 cm. More details about the geometry parameters of this device will be given in chapter 5.

To run a shear test, the chamber is filled with the sample and rotates at a constant rotational velocity  $\omega$  of 2.3 mrad/s. The bottom of the chamber and the lower side of the lid are rough due to the presence of small bars, which prevent wall slippage. The shear plane occurs below the bars of the lid, therefore the weight of the particles between the bars is taken into consideration when calculating the normal stress  $\sigma$  acting on the sheared surface. We used:

$$\sigma = \frac{Mg}{A} + \rho gh, \quad \text{Eq. 3.5}$$

where  $M$  is the normal loading weight,  $g$  is the gravitational constant,  $A$  is the area of the lid and  $h = 4 \text{ mm}$  is the height of the bars. The value chosen for the apparent density  $\rho$  is that

measured after filling the chamber, disregarding any volume variation due to the normal loading since the second term of Eq. 3.5 is small compared to the stress due to the loading mass in our experiments.

The shearing process consists of measuring the mean tangential stress  $\tau$  from the torque applied by the rotating powder on the powder kept fixed together with the lid; and obtained by the two force sensors  $F_1$  and  $F_2$ , which hold it (see Fig. 3.6). This measurement is repeated for various normal stresses. The relationship used to calculate the shear stress,  $\tau$ , as a function of  $F_1$  and  $F_2$  is given as:

$$\tau = \frac{3(F_1 + F_2)l}{2\pi(R_e^3 - R_i^3)} \quad \text{Eq. 3.6}$$

where  $l$  is the distance from the axis of rotation of the shear cell and the end of a rod connected to a force sensor,  $R_e$  and  $R_i$  are the external and the internal radii of the shear cell respectively.

The experiments were performed for the dry and wet glass beads with various liquid fractions of PEG 400. For each sample, a range of normal loads was used from 24 kg to 1 kg by removing 1 kg each step after tangential discharge. For a given normal load, the sample was sheared for about one minute. After a peak, a plateau value or an oscillatory steady-state regime is obtained.

In the following, a mean value of the shear stress at steady-state is calculated from the diagram (shear stress–time) and then used to study the flow properties of dry and wet glass beads (see Fig. 3.6).

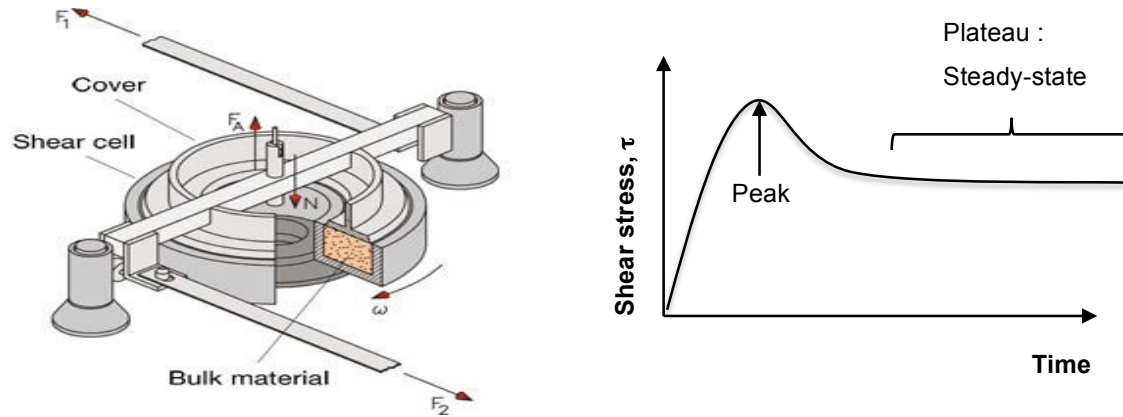


Fig. 3.6. (left) Schematic representation of the annular shear cell. (right) Schematic representation of shear stress – time diagram from the shear test.

### 3.3. Characterisation of the properties of glass beads (2 mm) for the input parameters for the simulation

#### 3.3.1. Nanoindentation test

The nanoindentation allows characterising the mechanical properties of materials. This technique was used to measure the hardness and the Young's modulus of the glass beads to be used for the simulation. The experiment was performed using NanoTest from Micro Materials Ltd, Wrexham, UK. The method consists of applying a load by the indenter on the surface of the glass bead and measuring the depth of penetration. The load is applied from zero to a defined maximum value and the other way around. Fig. 3.7 shows the load – displacement curves of four tests, each corresponds to a maximum load value (see Table 3.3). The hardness is defined as the maximum load divided by the projected contact area of indentation. The Young's modulus is determined from the slope of load – displacement curve for unloading and at maximum load (Fischer-Cripps, 2011). The Young's modulus is given by:

$$E = \frac{1}{2} \frac{\sqrt{\pi}}{\sqrt{A}} \frac{dP}{dh}, \quad \text{Eq. 3.7}$$

where  $E$  is the Young's modulus,  $A$  is the projected contact area and  $dP/dh$  is the slope of curve.

The measured values of the Hardness and the Young's modulus for each test are summarized in Table 3.3. An Average value of about 68 GPa is estimated for the Young's modulus of glass beads.

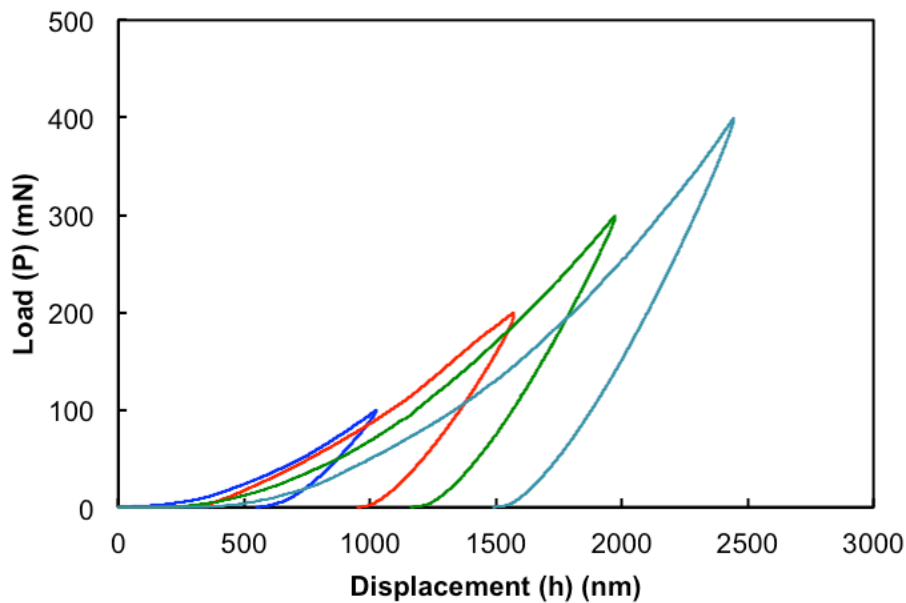


Fig. 3.7. Load – displacement curves of the nanoindentation test for four defined maximum loads.

Table 3.3. Values of the nanoindentation parameters measurements (max load and max depth) and the calculated Hardness and Young's modulus E.

Indent	Max load (mN)	Max depth (nm)	Hardness (GPa)	E (GPa)
<i>1</i>	<i>100</i>	<i>1026</i>	<i>5.97</i>	<i>76.60</i>
<i>2</i>	<i>200</i>	<i>1571</i>	<i>5.25</i>	<i>70.43</i>
<i>3</i>	<i>300</i>	<i>1975</i>	<i>5.16</i>	<i>66.20</i>
<i>4</i>	<i>400</i>	<i>2445</i>	<i>4.46</i>	<i>60.52</i>

### 3.3.2. Particle sliding friction

The friction of a single glass bead of 2 mm in diameter was studied using Nano-crush device from Micro Materials Ltd, Wrexham, UK (see Fig. 3.8). This technique is a 'pin-on-disk' method and consists of measuring the friction force of one particle sliding against a rotating base. The friction test was performed for glass beads as supplied, i.e. without any surface treatment; and also with glass beads washed by acetone and then dried in order to remove impurities on the surface. A polished steel and glass slide were used on the top of the rotating base. Friction measurements were performed for glass-steel and glass-glass contacts. Table 3.4 recapitulates the different friction tests performed. The friction force has been measured for sufficient time to reach the steady-state regime and for different applied normal forces ranging from 0.5 N to 8 N. The sliding friction coefficient is obtained from linear regression of the friction force – normal force data. The experiments were first performed for dry glass beads, then, to study the effect of liquid on the friction force, the beads were slightly wetted using polyethylene glycol (PEG 400), so it forms a liquid bridge at the contact surface. During the sliding of the bead upon the slide, we monitored that the liquid bridge is maintained. However the volume of liquid is inevitably reduced under the effect of wettability of the surface of the slide. We assumed that reduction of the liquid bridge volume does not affect the measured friction force. The different measurements will be discussed in chapter 5.

Table 3.4. Resume of the friction tests performed by the nano-crush device with the correspondents notation, which will be used for figures in chapter 5.

Friction test	Notation
Glass bead – steel slide	g-s
Glass bead – glass slide	g-g
Acetone washed glass bead –glass slide	wg-g
Glass bead – steel slide – liquid bridge (PEG 400)	g-s-liq
Glass bead – glass slide – liquid bridge (PEG 400)	g-g-liq

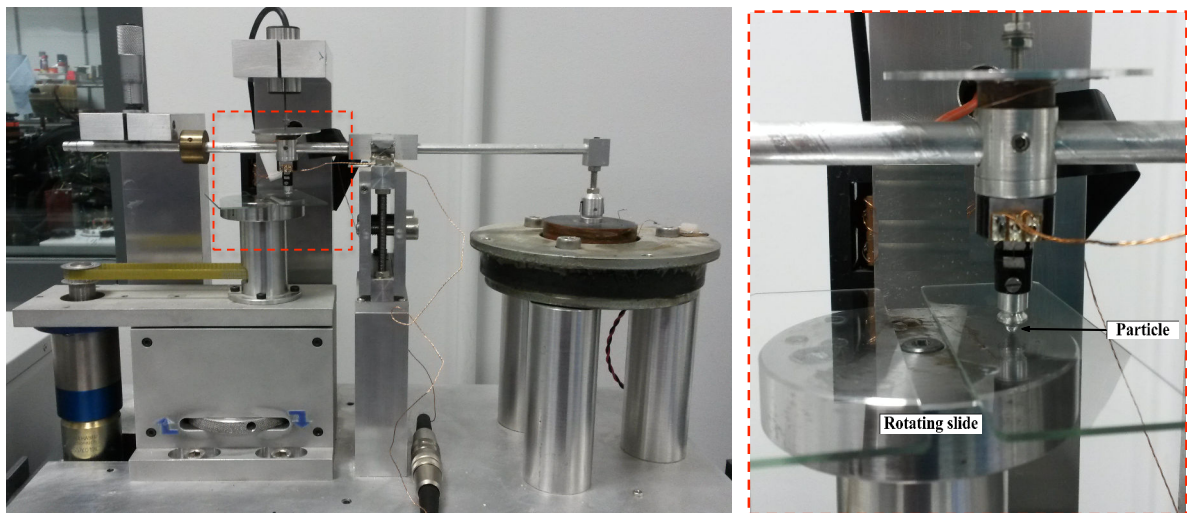


Fig. 3.8. (left) Photograph of the nano-crush device used to perform the friction test of the glass beads.  
(right) Zoom in showing a glass bead sliding upon a rotational glass slide.

## References

Denis, J., Briant, J. and Hipeaux, J.C. 1997. Physico-chimie des lubrifiants. Edition Technip  
Duran J., Sables, poudres et grains, Eyrolles Sciences.

Fischer-Cripps, A.C., 2011. Nanoindentation. Springer, New York Dordrecht Heidelberg  
London.

Han, F., Zhang, J., Chen, G. and Wei, X., 2008. Density, viscosity, and excess properties for  
aqueous poly(ethylene glycol) solutions from (298.15 to 323.15) K. J. Chem. Eng. Data, 53,  
2598-2601.

Schulze, D., 2008. Powders and bulk solids. Springer-Verlag, berlin Heidelberg.

## Chapter 4. Experimental study of the shear behaviour of wet granular material

---

### Résumé:

Dans ce chapitre, nous étudions la résistance en écoulement d'un milieu granulaire humide en fonction de la quantité de liquide introduite et de la contrainte normale qu'il subit. Nous avons mené une étude expérimentale pour des billes de verre sphériques et mono-disperses (70-110  $\mu\text{m}$ ) en présence d'un liquide non volatil et non visqueux (le polyéthylène glycol 400) afin de mettre en évidence l'effet des forces capillaires qui s'exercent entre les grains.

Les expériences ont été faites sur une cellule de cisaillement annulaire et pour une gamme de contraintes appliquées allant de presque 0.5-12 kPa. Les résultats donnent la variation de contrainte de cisaillement en régime stationnaire en fonction de la contrainte normale pour des fractions de liquide (volume de liquide/volume de solide) allant de très faible saturations où le liquide forme des ponts liquide au point de contact à l'occupation complète de l'espace entre les grains.

Dans une première partie, nous avons étudié le cas d'un milieu granulaire faiblement humide où le liquide incorporé entre les particules sous forme de ponts capillaires. La résistance au cisaillement dépend à la fois de la concentration de liquide et de la contrainte normale appliquée. On distingue trois régimes : A faible quantité de liquide (inférieure à 0,1%), le comportement est frictionnel (contraintes de cisaillement et normale sont proportionnelles), avec une friction légèrement accrue par rapport au cas sec (quelques pourcents). En augmentant la quantité de liquide: A forte contrainte normale (au-delà de 4 kPa), le comportement apparent est frictionnel et cohésif, avec une cohésion augmente avec la quantité de liquide puis tend vers une saturation ; A faible contrainte normale, la cohésion apparente est faible et le coefficient de friction augmente avec la concentration de liquide puis tend vers une saturation. Un modèle théorique a été utilisé afin de donner des explications plutôt microscopiques au comportement macroscopique observé. Cette partie est une prise partielle de l'article publié à *Powder Technol.*, 278, 65-71 avec autorisation de l'éditeur.

Dans une deuxième partie, nous avons étudié l'effet de la taille sur le comportement au cisaillement de milieu granulaire. Des billes de verre de 12-40  $\mu\text{m}$  de diamètre a été utilisé en conservant à peu près les mêmes proportions de liquide que avant. Le comportement observé est frictionnel pour les fractions de liquide de 0 à 20% avec un coefficient de friction apparent qui augmente avec la quantité de liquide. Deux régimes ont été identifiés : Une augmentation



faible pour  $V_R < 1\%$  et une augmentation plus élevée au delà de 1%. Le régime de saturation n'est pas atteint même à 20%, contrairement aux billes de plus grande taille.

Dans une troisième partie, un état de saturation plus important a été exploré, allant jusqu'au remplissage total des pores entre les billes de 70-110  $\mu\text{m}$ . Nous identifions des changements de régime de cisaillement selon les fractions de liquide. L'effet de la contrainte normale est aussi observé pour les quantités larges de liquide. La porosité de milieu granulaire diminue linéairement pour les fractions de liquide entre 20% et 60%, cependant une augmentation a été observée aux plus faibles fractions.

Ces observations indiquent que la prise en compte des effets capillaires dans un milieu granulaire nécessite deux paramètres : Quantité de liquide mais aussi contrainte de confinement. La dépendance de la contrainte de cisaillement avec ces derniers n'a pas la linéarité observée à l'état sec, non-cohésif. Toutes ces observations sont plus détaillées dans la suite.

### **Abstract:**

In this chapter, the shear behaviour of wet granular material is studied. We investigate the effect of the liquid content and the applied normal stress on this behaviour. An experimental study was carried out for glass beads of 70-110  $\mu\text{m}$  in diameter, mixed with various amounts of polyethylene glycol 400 as liquid.

An annular shear cell was used to carry out the experiments, for a large range of applied normal stress from about 0.3 kPa to 12 kPa. The results give the variation of the shear stress at steady-state as a function of the normal stress for a wide range of liquid fraction (volume of liquid/volume of solid). The incorporated liquid goes from forming bridges at the contact point to completely filling the space between grains.

At first, a partially state of saturation was studied where liquid bridges were formed. The shear behaviour depends on the amount of liquid and the applied normal stress. Three regimes are observed: at low liquid fractions (up to 0.1%), the behaviour is frictional (shear stress proportional to the normal stress) with a slightly higher friction coefficient compared to the dry one. At higher liquid fractions: at high normal stress (more than 4 kPa), an apparent cohesion is observed and the behaviour may be interpreted as frictional, with the same friction coefficient plus an additional normal stress due to the capillary forces between the beads; at low normal stress the apparent cohesion is less and may be qualitatively explained by the diminution of broken capillary contacts during shearing when the voidage fraction of the granular bed increases. This result is corroborated by a theoretical approach estimating the capillary forces. This part is a partial reproduction of the paper published in *Powder Technol.*, 278, 65-71 with authorization of the publisher.

Secondly, the effect of the particle size on the shear behaviour of wet granular material is investigated. Small glass beads of 12-40  $\mu\text{m}$  in diameter are used for this cause and almost the same liquid fractions are investigated. The observed shear behaviour is frictional for the liquid

fractions from 0 to 20% with an apparent friction coefficient increasing as the liquid fraction increases. Two regimes were identified: a small increase for small liquid fractions up to 1% and a significant increase beyond that. The saturation regime is not yet observed at 20% liquid fraction in contrary to what was observed with larger size of glass beads.

Finally, more saturation states are explored going up to completely filling the space between beads of 70-110  $\mu\text{m}$ . Different regimes are identified depending on the liquid fraction. The effect of the normal loading is also observed at the large liquid fractions. Regarding the voidage fraction, it is linearly decreasing as the liquid fraction increases in the range of 20% to 60%. However, it is increased for smaller liquid fractions (less than 20%).

These observations emphasize two parameters to take into consideration for the study of the capillary effect: the liquid fraction and the normal loading. More details will be given in the following in this chapter.

## 4.1. Introduction

The effect of small amounts of liquid on the behaviour of the granular material has been extensively studied. It is now clearly understood that the cohesive behaviour is caused by the liquid bridges formed at the contact points between particles. Many authors have focused on the understanding of this behaviour. Many models to calculate the capillary forces from liquid bridges now exist in the literature. Most of these models give a good estimation of the capillary forces. Rumpf (1962) studied the relationship between tensile strength and capillary forces, and proposed a model to estimate this tensile strength. This model will be used in this study to evaluate the tensile strength of the wet glass beads. Hornbaker *et al.* (1997), Fraysse *et al.* (1999) and Bocquet *et al.* (2002) focused on the static properties of granular material. They demonstrated the influence of small amounts of liquid on the angle of repose. They observed that the surface angle of repose increases with the quantity of liquid. The angle is related to the maximal ratio between shear and normal stresses. However, the relationship between the angle of repose and the cohesion is not clearly understood yet (Mitarai and Nori, 2006). In these studies, the flow of granular material occurs at low levels of normal stress since they are located close to the free surface. This is not the case in the quasi-static and dynamic states studies performed in shear cells or mixers, where the applied or established normal stresses may influence the flow properties (Oulahna *et al.*, 2012 and Rondet *et al.*, 2013). Most of these studies focus on the yield criterion in the case of quasi-static experiments in shear cells or are not able to quantify or vary the normal stresses in steady-state flows in mixers. None of these works explore the relationship between steady-state shear – normal stresses for different normal loadings applied to the wet granular material.

In this chapter, we focus on the effects of both liquid content and normal loading on the shearing behaviour of wet glass beads, in steady-state situations. We also investigate the voidage fraction variation of the granular material for a large range of liquid contents. This chapter contains three main parts. In the first part, we focus on the situation of partially wet glass beads of 70-110  $\mu\text{m}$  in diameter. The effect of liquid on the shear behaviour is investigated. The capillary forces and the tensile strength are also theoretically estimated and compared with the experimental results. In the second part, we study the effect of the particle size on the shear behaviour. Smaller size glass beads are used, in the range of 12-40  $\mu\text{m}$  in diameter, and the results are compared with the larger size glass beads. In the third part, we investigate other saturation state of liquid than the pendular state.

## 4.2. Shear behaviour of partially wet granular material

### 4.2.1. Effect of liquid on the voidage fraction of the granular bed

In this section, we analyse the effect of liquid on the voidage fraction of the granular bed. The liquid fractions,  $V_R$  (volume of void divided by the total volume of the granular material, including solid, liquid and air), studied in this section vary from 0% to 20%. The voidage fraction is calculated by taking into consideration the volume occupied by the liquid. Thus, the voidage fraction,  $\varepsilon_{wet}$ , is given as

$$\varepsilon_{wet} = \frac{V_V}{V_T} = 1 - \frac{\rho}{\rho_s} \frac{1 + V_R}{1 + V_R \left( \frac{\rho_L}{\rho_s} \right)} \quad \text{Eq. 4.1}$$

where  $V_V$  and  $V_T$  are the volume of the void and the total volume of the granular material respectively and  $\rho$  is the bulk density and it is measured at low normal stress (the granular material is subjected to its own weight) and high normal stress (the granular material is consolidated with a normal stress of about 12 kPa). The method used to measure the voidage fraction was given in chapter 3.

Fig. 4.1 shows the variation of the voidage fraction of the granular bed as a function of the liquid fraction  $V_R$  in a semi-logarithmic scale. For a small liquid fraction, the voidage decreases slightly due to the lubrication at some contact points between particles. This lubrication leads to the rearrangement of the granular bed to occur denser configurations. When  $V_R$  increases, a clear increase of the void is observed from  $V_R$  around 0.05%. Indeed, when the amount of liquid reaches certain value, the capillary forces exceed the weight of the particles and become dominant. As a consequence, the liquid bridges created between particles are able to sustain a loose assembly of particles, with larger gaps in the granular media leading to a lower density configuration. Then, the voidage fraction tends to saturation from about 1% to 7% of  $V_R$ , where the increasing of liquid content may contribute to enlarge the volume of liquid bridges without having a great effect on the voidage fraction. The increase of the amount of liquid beyond 7% leads to a decrease in the voidage fraction since liquid progressively takes the place of the air.

These results corroborate those of Feng and Yu (1998) and Yu *et al.* (2003) regarding the relationship between the voidage fraction, capillary forces and liquid content. They found that the voidage fraction of glass beads of different sizes increases with the liquid content to reach a maximum value at a critical point. This increase was explained by the creation of liquid bridges when adding liquid to the granular material, which limits the particle motion to form packing and hence enlarge the voidage fraction. They also assumed that an increase of the amount of liquid (beyond the maximum quantities) leads to a decrease in the capillary forces and, as consequence, to a decrease in the voidage fraction.

Fig. 4.1 also shows a comparison of the voidage fraction at low and high normal stresses. The same variation described above is observed regardless of the effect of the normal stress. The increase of the normal stress decreases the value of the voidage fraction however it does not prevent the increase of the voidage caused by the capillary forces. The difference of the voidage fraction due to the normal stress is more pronounced at high liquid content.

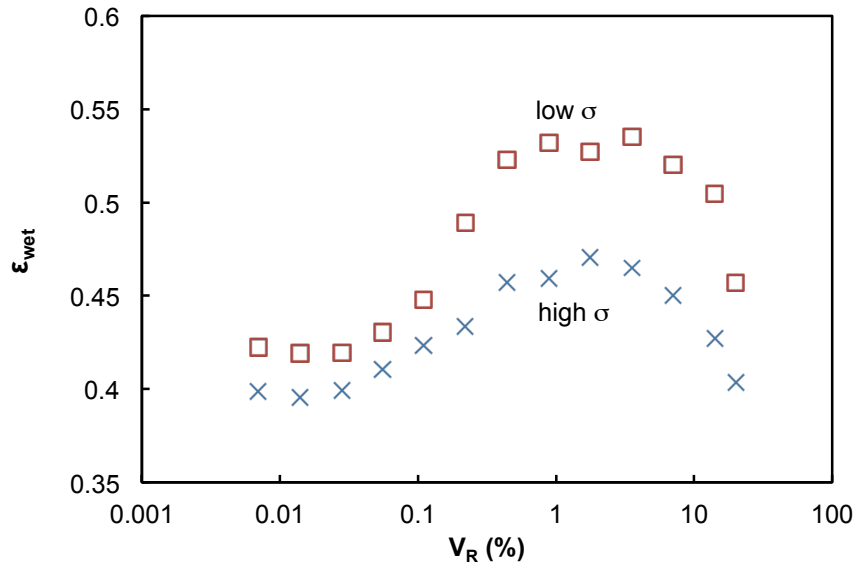


Fig. 4.1. The average voidage fraction versus the liquid fraction at low normal stress and at high normal stress after pre-consolidation at 12 kPa.

#### 4.2.2. Effect of liquid on the steady-state shear stress

We will now investigate the effect of a small amount of liquid on the steady-state flow. The glass beads, ranging from 70 to 110  $\mu\text{m}$  in diameter, are non-cohesive in dry conditions. The friction between the particles induces the shear resistance. In wet conditions, the shear resistance is also caused by the inter-particle forces, which also modify the texturization of the granular bed, as indicated by the voidage fraction measurements (see Fig. 4.1).

Fig. 4.2 illustrates the mean shear stress  $\tau$  versus the normal stress  $\sigma$  for different liquid fractions. The mean shear stress value is the mean value calculated from the shear stress signal during shearing at steady-state (see subsection 3.2.2 for more details about the mean value calculation and Appendix 4.2 for more details about the stick-slip effect). We observe that the data of the dry glass beads are perfectly linear. The variation of the shear stress – normal stress can be given by  $\tau = \mu_{dry}\sigma$  in agreement with the Coulomb's law. However, we observe that  $\tau$  is dependent on the liquid content as the curves are shifted relative to the dry case: the shear stress of wetted glass beads increases when the amount of liquid increases.

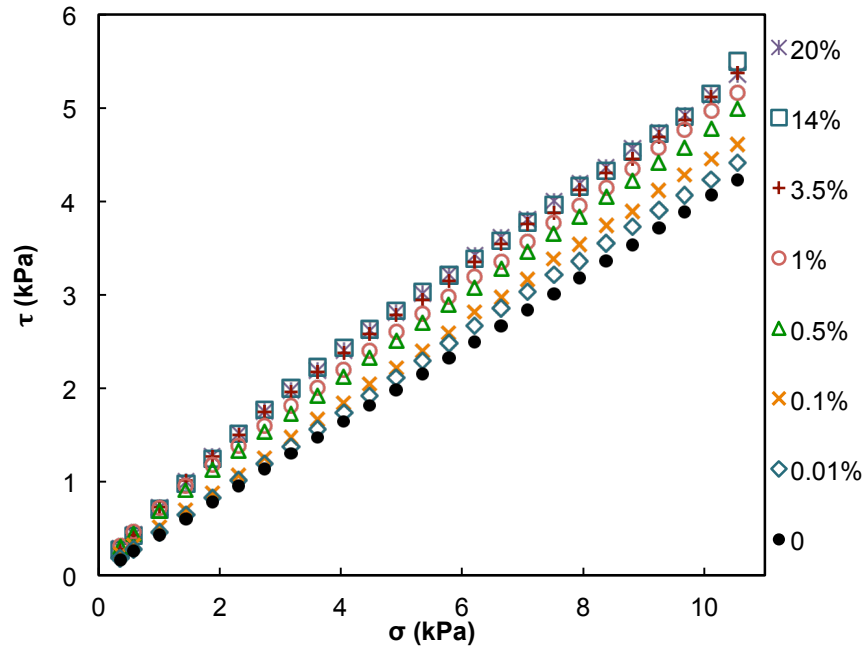


Fig. 4.2. Shear stress variation with the normal stress for dry and wet glass beads with a volume fraction ranging from 0.01% to 20%.

The shear resistance is also studied for a wide range of applied stresses, allowing us to check whether the apparent friction  $\tau/\sigma$  remains constant for a given liquid content or whether it also depends on the normal stress applied. For this purpose, enhancing the differences between the curves and focusing on the relative changes when introducing a given quantity of liquid, we define the relative shear stress  $\tau_r$  by subtracting the shear stress in dry conditions from the  $\tau$  measured for wet conditions:

$$\tau_r = \tau - \mu_{dry} \cdot \sigma \quad \text{Eq. 4.2}$$

$\tau_r$  is plotted versus  $\sigma$  in Fig. 4.3 for larger variation of the liquid fraction compared to the curves presented in Fig. 4.2.

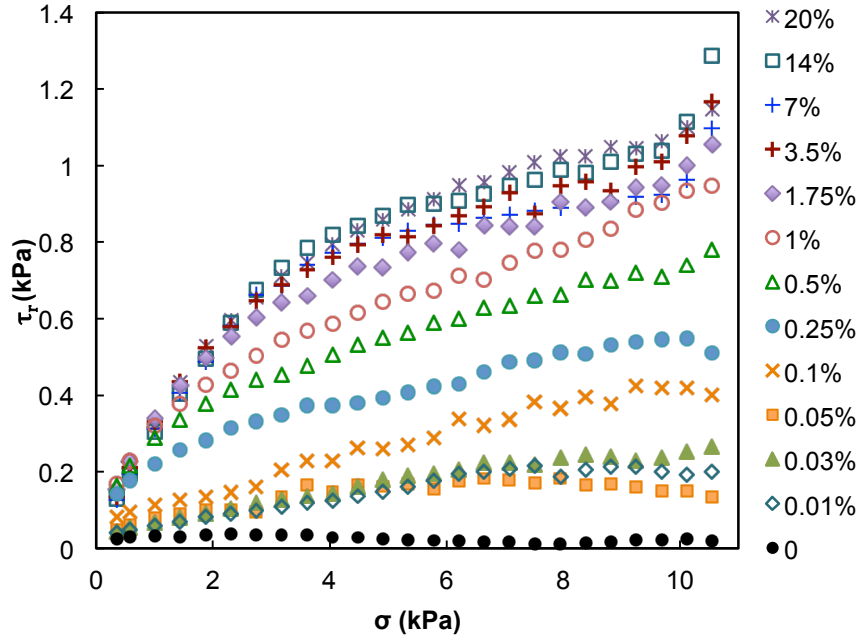


Fig. 4.3. Relative shear stress  $\tau_r$  as a function of the normal stress for dry and wet glass beads, for large variation of liquid fractions.

The observed curves show a clear variation of the shape depending on the normal stress and the liquid content, and may be classified within the following regimes:

**a) For small liquid content** — If the volume ratio of liquid is small, ranging from 0.01% to 0.05%, the observed behaviour is frictional. The steady-state shear stress is proportional to the normal stress:  $\tau = \mu_{wet}\sigma$ , where  $\mu_{wet}$  is the friction coefficient of the wet granular material. The observed curves show that the friction of slightly wet glass beads is a little higher than that observed for the dry case; The friction coefficient determined from curves  $\tau$ - $\sigma$  in Fig. 4.2 is equal to 0.42 instead of the 0.4 for dry glass beads, with no significant dependency on  $V_R$  within the range from 0.01% to 0.05% since the curves are superimposed.

When the liquid fraction increases further (beyond 0.1%), the curves show a slope variation, and data can be fitted using two straight lines: one at low normal stress ( $\sigma < 4$  kPa) and the other at high normal stress ( $\sigma > 4$  kPa). Hereinafter, the experimental results obtained will be explored separately at high and low normal stresses.

**b) High liquid content, high normal stress** — For  $\sigma > 4$  kPa, the shear-normal stresses relationship is linear, with a slope close to  $\mu_{wet}$ , that which is observed in the a) regime, but shifted upward in the  $\tau_r$ - $\sigma$  plane when the liquid content is increased, defining residual cohesion  $c$  or apparent traction  $T_s$  as:

$$\tau \approx \mu_{wet}\sigma + c(V_R) \approx \mu_{wet}(\sigma + T_s(V_R)), \quad \text{Eq. 4.3}$$

This enhanced shear resistance originates from the inter-particle forces due to the presence of liquid and may be interpreted as if these forces exert a supplementary pressure  $T_s$  on the shear

plane. Fig. 4.4 shows traction  $T_s$  versus  $V_R$  on a semi-logarithmic scale. In the following section, the values obtained will be compared to a theoretical prediction based on the estimation of the capillary forces between the particles.

**c) High liquid content, low normal stress** — For low normal stress, the shear resistance is observed to be below that extrapolated at high normal stress (*b*) and slightly greater than that for the lowest liquid content (*a*). In this regime, the shear resistance saturates or presents a maximum value for a given normal loading, when the liquid content is increased.

The apparent cohesion or traction remains low compared to the extrapolated one from the high normal stress values (see Fig. 4.4) while the apparent friction coefficient  $\mu_{\text{wet}}$  deduced from the slope of the curves  $\tau$ - $\sigma$  is greater than that observed in the *b*) regime.  $\mu_{\text{wet}}$  increases from approximately 0.42 to 0.6 and then tends towards saturation.

This phenomenon is explained qualitatively by the fact that the voidage fraction at low normal stress is higher than at high normal stress. Therefore, there is less contact between particles, fewer particles to separate in the shear plane and there is more rolling accommodation of the shear deformation, which reduces the number of broken liquid bridges per particle on the shear plane (see Fig. 4.6). This point will be discussed in the next subsection.

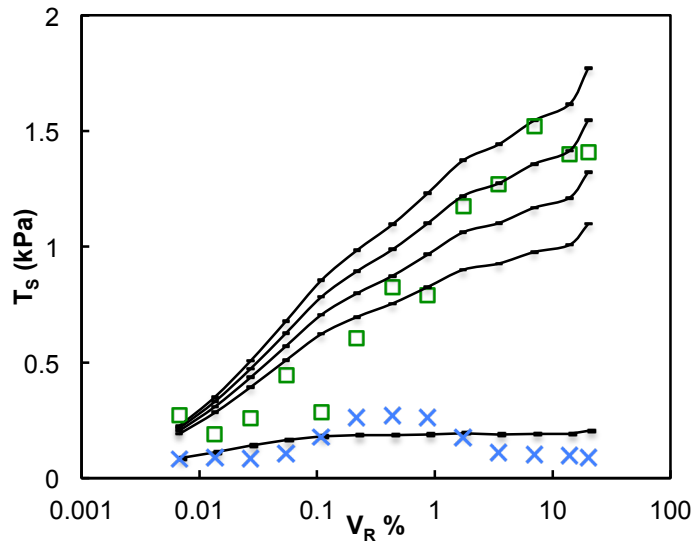


Fig. 4.4. Experimental and theoretical traction (tensile strength) as a function of the liquid fraction on a semi-logarithmic scale. Squares and crosses: experimental data for high normal stress ( $\sigma > 4$  kPa) and low normal stress ( $\sigma < 4$  kPa) respectively. Continuous lines: theoretical traction for different coordination numbers (1,5,6,7 and 8) shown from bottom to top in this figure.



#### 4.2.3. Theoretical estimation of the tensile strength using the Rumpf model

The tensile strength  $T_s$  represents the tensile force at failure divided by the cross section of the agglomerate. In the case of a random packing of monosized spherical particles in the pendular state, the tensile strength may be approximated by Rumpf relation (Rumpf, 1962) as follows:

$$T_s = \frac{1 - \varepsilon_{wet}}{\pi} k \frac{F_c}{d^2}. \quad \text{Eq. 4.4}$$

For wet granular media, the tensile strength is caused by the sum of liquid bridge forces  $F_c$  at contact points between the particles apart from the failure plane. The above equation also depends on the particle diameter,  $d$ , the wet voidage fraction,  $\varepsilon_{wet}$ , and the average coordination number,  $k$ . The latter may be empirically related to  $\varepsilon_{wet}$  according to this relationship (Pietsch, 2002):

$$k = \pi / \varepsilon_{wet}, \quad \text{Eq. 4.5}$$

leading to a coordination number between 7 and 8 for dense packing and around 6 to 7 for loose packing. Many models have been developed to determine the capillary force due to the presence of a liquid meniscus between two spheres. Some of these models have been discussed in subsection 1.3.3. We have shown that the toroidal model, proposed by Fisher (1926), gives a good approximation of the liquid bridge force for spherical particles with smooth surface. The boundary method, developed by Adams and Perchard (1985) consists in evaluating these forces at the sphere surface (Simons *et al.*, 1994). When the separation distance between the particles is zero, this approach predicts a decrease in the capillary force with an increase in the volume of liquid, which does not correspond to our experimental observations. Piesch (1968) proposed to resolve the decrease of the capillary force, adding a minimum value corresponding to the separation distance  $2a$  between two spheres, caused by the asperities on the surface of the particles and allowing the liquid to be incorporated in between (see Fig. 4.5). An approximate value of the minimum half-separation distance  $a$  was evaluated from scanning electron microscopy (SEM) by measuring the height of the asperities on the glass bead surface. Fig. 4.5-b shows an example of a SEM image showing two glass beads touching, in the presence of a small amount of liquid ( $V_R = 0.1\%$ ). The observation of the particle surface shows several asperities of a significant size. The half-separation distance was estimated to be between 1 and 2  $\mu\text{m}$ . This value is similar to other observations of the roughness of a 100  $\mu\text{m}$  glass bead by Atomic Force Microscopy (AFM), where the height of the surface roughness is approximately 1  $\mu\text{m}$  (Moller, 2007). A dimensionless half-separation distance,  $\delta = a/R$ , has been set to 0.03 and considered to be constant for all the experiments.

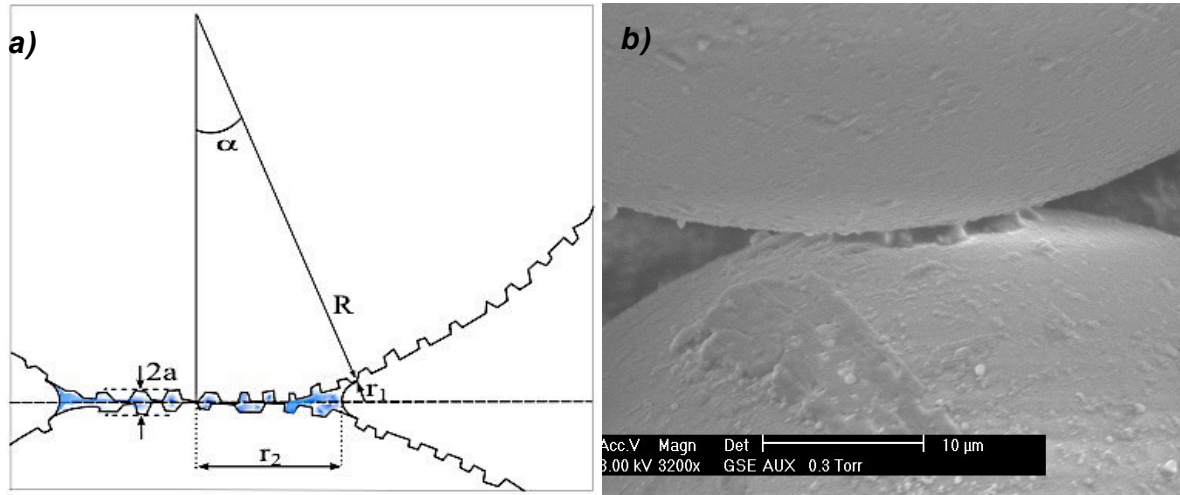


Fig. 4.5. (a) sketch of a liquid meniscus. (b) Electron microscope scan image of wet glass beads ( $V_R = 0.1\%$ ) showing the asperities on the particle surface and at the contact point.

The capillary force was subsequently determined using the Adams and Perchard (1985) equation which states

$$F_c = 2\pi R\gamma \sin^2 \alpha + \pi R^2 \sin^2 \alpha \Delta P, \quad \text{Eq. 4.6}$$

for a wetting contact angle equals to zero, which is the case here since the glass beads are fully wetted by the PEG 400. The capillary depression  $\Delta P$  is given by the Laplace equation as

$$\Delta P = \gamma \left[ \frac{1}{r_1} - \frac{1}{r_2} \right], \quad \text{Eq. 4.7}$$

where  $r_1$  and  $r_2$  are the main radii of curvature (see Fig. 4.5-a) and are given by

$$r_1 = R \left( (1 + \delta) \frac{1}{\cos \alpha} - 1 \right), \quad \text{Eq. 4.8}$$

$$r_2 = R \left( 1 + (1 + \delta) \tan \alpha - (1 + \delta) \frac{1}{\cos \alpha} \right), \quad \text{Eq. 4.9}$$

where  $\alpha$  is the half-filling angle (see Fig. 4.5-a). It was estimated from the relation proposed by Rabinovich (2005) for very small magnitude of separation distance:

$$\alpha^2 = 2 \sqrt{\frac{V}{\pi R^3}}, \dagger \quad \text{Eq. 4.10}$$

where  $R$  is the harmonic mean radius used to estimate the size of the glass beads ranging from  $R_m = 35 \mu\text{m}$  to  $R_M = 55 \mu\text{m}$  of radii ( $1/R = \frac{1}{2}(1/R_m + 1/R_M)$ ) and  $V$ , used to calculate the half-filling angle, is the liquid bridge volume. This volume is determined using the hypothesis of an homogeneous distribution leading to:

$$V = V_R \frac{\frac{\pi}{6} d^3}{\frac{\kappa}{2}}, \quad \text{Eq. 4.11}$$

The capillary forces have been estimated from the above equations and introduced into Eq. 4.4 in order to determine the tensile strength  $T_s$ .

Fig. 4.4 gives  $T_s$  as a function of the volume ratio  $V_R\%$  for various potential coordination numbers  $k$  (continuous lines), and compares these estimations with the experimental values (squares) introduced in the previous subsection. There is a semi-quantitative agreement between the theoretical estimations and the measured values, despite some scattering in the experimental dataset. At high normal loading, the experimental observations are quantitatively close to the estimated figures when the coordination number is between 5 and 8; a slightly lower value than 9, which was the value expected for densely packed of mono-disperse spheres. This is consistent with the observation of porosities higher than 0.36, indicating that the dense state is not reached, except at high normal loading and low liquid content ( $V_R < 0.1\%$ ).

This agreement suggests that the capillary contribution described by Eq. 4.3, has a magnitude, which corresponds to the breakage of all the wetted contacts between the particles on the shear plane, i.e. the value that is obtained if the packed bed is sheared into two rigid blocks sliding against each other (see Fig. 4.6).

This phenomenon is completely different to that observed in a low applied normal stress situation, where the weak compactness of the medium prevents the simultaneous rupture of capillary bridges. The experimental tensile strength  $T_s$  has a magnitude, which corresponds to only one or two capillary bridges broken per particle on the shear plane. This is lower than the number of contacts predicted for loose packing. This low value suggests that in a situation of loose packing, the shear deformation is accommodated by local rolling rearrangements, which maintains some of the wet contacts between particles (see Fig. 4.6).

---

<sup>†</sup> This equation was wrongly copied in the paper by Louati et al., (2015) as  $\alpha^2 = \sqrt{2 \frac{V}{\pi R^3}}$ . This has slightly affected the shape of the curves in Fig. 4.4, however it does not affect the results and discussions made from this graph.

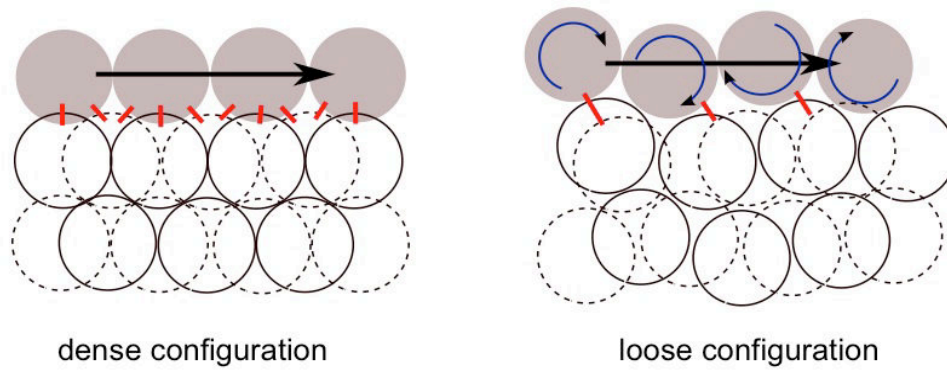


Fig. 4.6. Breakdown of the liquid bridges between particles apart from the shear plane and depending on the granular material configuration.

### 4.3. Effect of particle size on the shear behaviour of partially wet granular material

#### 4.3.1. Effect of particle size on the voidage fraction of the granular bed

It is known from the literature that the voidage fraction of mono-size spheres decreases for an increase in the particle size. This is true for a particle size smaller than a critical value beyond which the voidage fraction becomes independent on the particle size (Yu *et al.*, 1997). In this study, we compare the voidage fraction of two different sizes of glass beads. In the dry case, the voidage fraction of a loose packing of glass beads in the range of 12-40  $\mu\text{m}$  of diameter is about 0.45 and it is bigger than the one measured for 70-110  $\mu\text{m}$ , about 0.42. Fig. 4.7 shows the variation of the voidage fraction with the liquid fraction increasing up to 20%. The same variation is observed for the two different sizes of glass beads (as described in subsection 4.2.1) with large value of the voidage fraction for the small size. The effect of liquid on the voidage fraction is also more pronounced for small particle size. This was also observed for other size of glass beads (250  $\mu\text{m}$ , 1000  $\mu\text{m}$ , 2000  $\mu\text{m}$  and 4000  $\mu\text{m}$ ) in the work of Feng and Yu (1998) and Yu *et al.* (2003). In fact, by decreasing the size of particles, the capillary forces become more relevant compared to the gravitational forces and hence the effect on the voidage fraction is more pronounced. For the small size of glass beads (less than 100  $\mu\text{m}$ ), Van-der-Waals forces are present and they prevail the gravitational forces. This emphasizes the role of the capillary force, which overcomes the effect of both the gravitational and the Van-der-Waals force.

By increasing the fraction of liquid above 1% of  $V_R$ , the difference of the voidage fraction between the two sizes of glass beads becomes larger. This was also observed in Fig. 4.1, showing the variation of the voidage fraction at low and high normal stresses. This highlights the effect of the volume of liquid bridge increasing, which increases consequently the effect of the capillary forces.

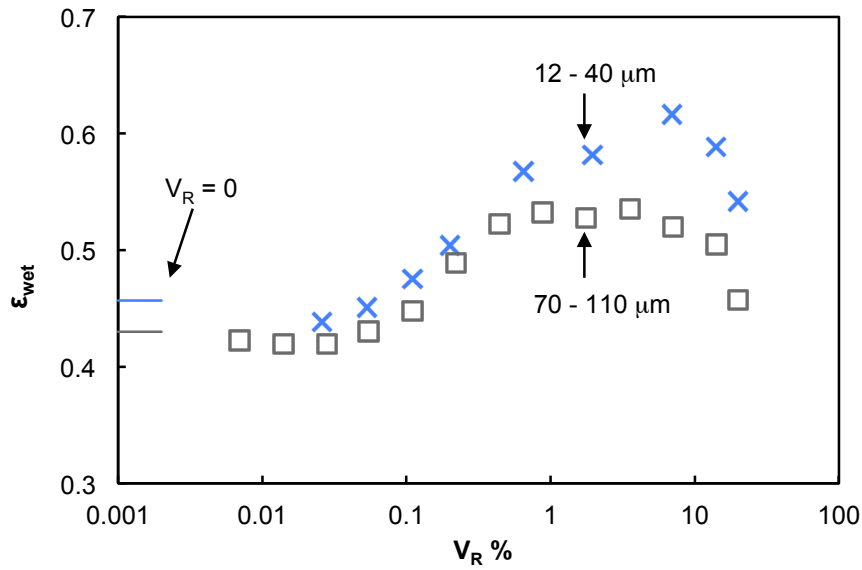


Fig. 4.7. Variation of the voidage fraction with the liquid fraction for two different sizes of glass beads: square for 12-40  $\mu m$ , cross for 70-110  $\mu m$ .

#### 4.3.2. Effect of particle size on the shear stress

The flow behaviour of the dry glass beads 12-40  $\mu m$  is more cohesive compared to the 70-110  $\mu m$ . This is observed by looking at the flow behaviour of the two samples of glass beads in a small container of 1000  $cm^3$ ; a free flowing is observed for the large size versus an avalanching flow for smaller one. The measurement of the apparent friction coefficient from the shear stress – normal stress curves gives 0.44 and 0.4 for small and large sizes respectively. The Van-der-Waals forces can increase the apparent friction in the dry case for small particles.

Fig. 4.8 shows the shear stress – normal stress for various liquid contents. We observe an increase of the shear stress by increasing the liquid fraction in the range of 0.03% to 20%. Generally, the observed curves show a linear relationship of the shear – normal stress for the different liquid fractions. We point out that curves may converge towards larger shear stress at high normal stress beyond 8 kPa, which makes data slightly drifting from linearity towards higher shear stress. However, we observed that the data were not linear for 70-110  $\mu m$  glass beads when the liquid fraction exceeds 1%; data were drifted towards lower shear stress (see Fig. 4.2). It is possible that higher normal stresses should be reached to obtain the same variation for the small glass beads.

The apparent friction coefficient is calculated from the slope of curves, for normal stress up to 8 kPa of the normal stress. Data are well fitted by linear regression with a coefficient of determination ( $R^2 > 0.998$ ) for all cases. The variation of the apparent friction coefficient with the liquid fraction is given in Fig. 4.9. This apparent friction coefficient increases by increasing the liquid fraction. However, we can distinguish two regimes: for small liquid content ( $V_R \leq 1\%$ ), the apparent friction is slightly increased with the liquid from 0.44 in the dry case to 0.5

at 1%. The apparent cohesion obtained by extrapolation of curves (as shown by Eq. 4.3) remains low and close to the dry case as it can be observed from Fig. 4.8. For higher liquid content ( $V_R > 1\%$ ), the increase of the apparent friction coefficient is more significant, e.g. it rises from about 0.5 at 1% to 0.65 at 20%. The regime resembles to the regime c) observed for 70-110  $\mu\text{m}$ . However, no saturation of the shear stress is yet observed for the small glass beads with the liquid fraction increasing; for liquid fraction up to 20%, the shear stress is still increasing with the liquid fraction. This may be explained by the fact that for the small beads the number of particles in the shear cell is much larger. An estimation of the number of glass beads in the shear cell shows that the small glass beads are 70 times the number of the big ones. Thus, the number of the coordination number by unit of volume is much larger and hence the number of liquid bridges formed at the contact points increase as well. We assume that the saturation of the shear stress is reached when the number of liquid bridges is completed. Indeed, the shear resistance gets rise from the number of liquid bridges broken under shearing. The saturation of the shear stress can not be reached while the number of liquid bridges is increasing with the liquid addition.

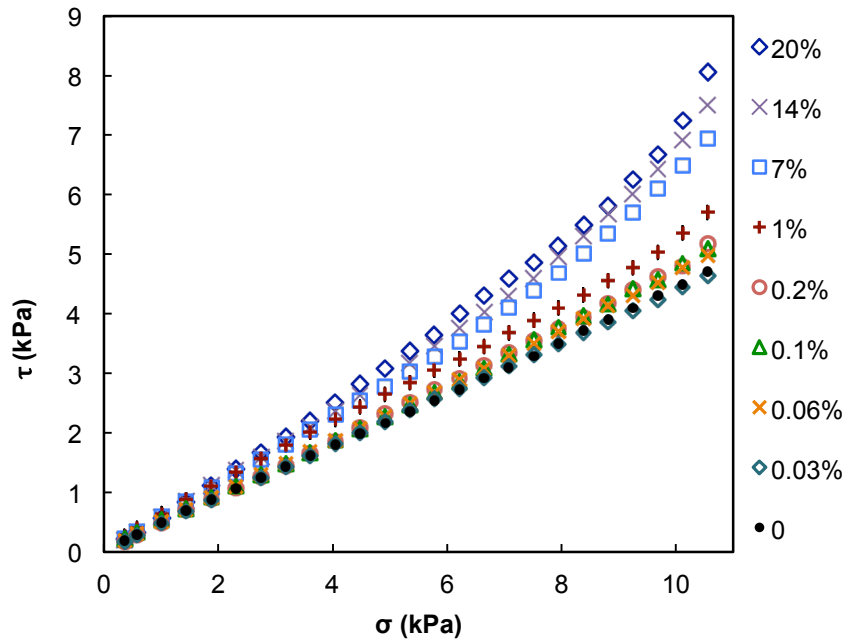


Fig. 4.8. Shear stress variation with the normal stress for dry and wet glass beads (12-40  $\mu\text{m}$ ) with a volume fraction ranging from 0.01% to 20%.

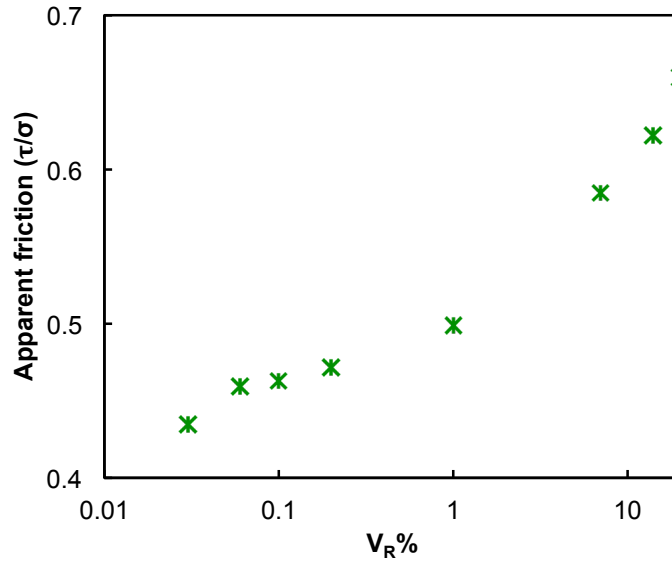


Fig. 4.9. Variation of the apparent friction coefficient with the liquid fraction.

#### 4.3.3. Theoretical estimation of the tensile strength using the Rumpf model

The tensile strength of wet granular material depends on the capillary force as shown in the model of Rumpf (Eq. 4.4). It was also discussed in subsection 4.2.3 how the liquid fraction and the packing density affect largely the tensile strength. However, there is another parameter, which is as important in the estimation of the tensile strength: the particle size. It is reported in the literature that fine particles have higher strength than large particles (Lu *et al.*, 2007). However, we have seen that both the liquid saturation and the packing density are also affected by the particle size decrease. In this section, the tensile strength of 12-40  $\mu\text{m}$  glass beads is estimated from the model of Rumpf and compared to the results of 70-110  $\mu\text{m}$  glass beads.

Although the size of particles is smaller, the size of the asperities observed by AFM is very close to the one observed for 70-110  $\mu\text{m}$ . A dimensionless half-separation distance of 0.06 is considered in this case. We recall that this value step in the calculation of the main radii of the liquid bridge curvature necessary to compute the capillary force and then the tensile strength. The capillary force increases with the particle size increasing, however the tensile strength is inversely proportional to the particle size.

Fig. 4.10 shows the calculated tensile strength  $T_S$  as a function of the volume ratio  $V_R$  (%) for various potential coordination numbers  $k$  (continuous lines). We clarify that the irregularities of the theoretical curves (continuous lines) are caused by the values of the voidage fraction used in Eq. 4.4, which correspond to the experimental values measured for different liquid fractions. On one hand, as expected, the observed values of  $T_S$  are higher than the one observed for 70-110  $\mu\text{m}$  glass beads (Fig. 4.4). This can be explained by the fact that the number of contact per unit of surface increases for a decrease in the particle size (Carr, 1967) and consequently the number of liquid bridges increases too. Therefore, higher tensile forces are

required to produce rupture of the liquid bridges in the shearing plane. On the other hand, the experimental data (crosses) has value whose magnitude corresponds to a low number of capillary bridges broken. In fact, it was observed that the small glass beads have looser packing density compared to the bigger glass beads (see Fig. 4.7). Therefore, higher normal stresses (beyond 11 kPa) are needed to reach denser packing density and hence higher tensile strength, which should correspond to the upper continuous lines in Fig. 4.11. This may also explain the profile of shear stress – normal stress curves of small glass beads (Fig. 4.8), which resembles to the profile of curves at low normal stress ( $\sigma < 4$  kPa) of big glass beads (Fig. 4.2) (regime *c*) in subsection 4.2.2); a slope variation can be obtained at higher normal stress (beyond 11 kPa).

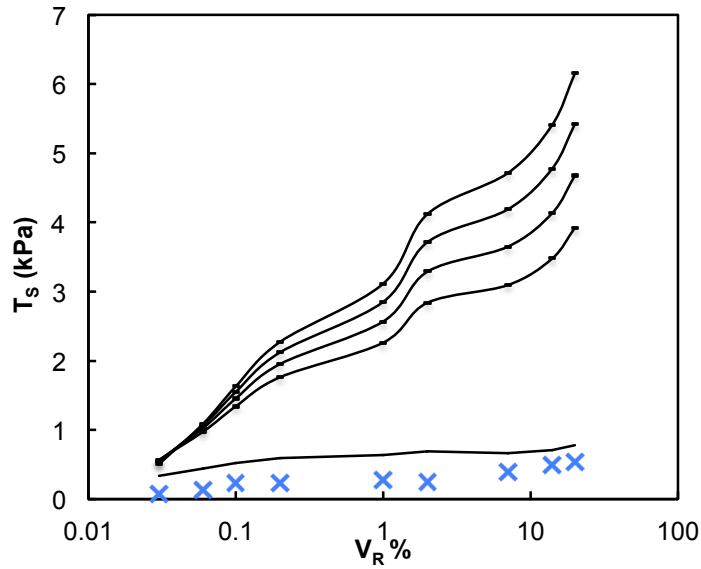


Fig. 4.10. Experimental and theoretical traction (tensile strength) as a function of the liquid fraction on a semi-logarithmic scale. Crosses: experimental data for the normal stress given in Fig. 4.8. Continuous lines: theoretical traction for different coordination numbers (1, 5, 6, 7 and 8) shown from bottom to top in this figure.

#### 4.4. Investigation of more saturation states of liquid

In the pendular state, where the liquid bridges are mainly formed at the contact point between particles, it was shown that the cohesive force acts through the liquid bridges. The capillary force depends on the quantity of the liquid and hence on the number of liquid bridges. It depends also on the volume of liquid bridges. In the funicular state, some of the gaps are filled with liquid; the cohesion acts through the suction at the liquid-air interface together with the remained liquid bridges. In the capillary state, almost all the gaps are filled with the liquid; the cohesion is only ensured by the suction at the liquid-air interface. Therefore, depending on the quantity of liquid, the texturization of the granular material changes. We expect also that the mechanical behaviour of the granular material for the different states changes. In this section, the effect of liquid of different saturation states is investigated. The glass beads of 70-110  $\mu\text{m}$  are considered here and the liquid fraction is extended to up to 60%. The variation of the voidage fraction, as shown in Fig. 4.1, will be discussed for more liquid fractions. Moreover,



the voidage fraction will also be analysed from X-ray tomography images. The mechanical properties of the different states of saturation will be analysed from the shear stress measurement.

#### 4.4.1. Effect of liquid on the voidage fraction

The effect of liquid on the voidage fraction is now investigated for different saturation states of liquid, i.e. pendular, funicular and perhaps capillary state. Data in Fig. 4.1 are extended to more liquid fractions up to 60%. The latter is almost the maximum liquid fraction that can be held by the granular material before reaching the slurry state. It can be estimated from this relationship ( $V_R \approx \varepsilon/(1 - \varepsilon)$ ) that the slurry state is reached at almost 70% of liquid fraction, for a voidage fraction of ( $\varepsilon = 0.41$ ). It was explained for the small liquid fractions, up to 20%, that the voidage fraction depends on the capillary force. For larger liquid fractions, the capillary force arises from the suction at the interface air-liquid. Yu *et al.* (2003) reported that, after a critical value of the liquid fraction, the voidage fraction might decrease. It is assumed that the capillary forces might vanish beyond that maximum value (Schubert, 1984). Fig. 4.11 shows that  $\varepsilon_{\text{wet}}$  is decreasing linearly by increasing the liquid fraction ranging from 20% to 60%. The linearity of data is observed at low and high normal stresses applied upon the wet granular bed during measuring of the voidage fraction. This assumes that the granular material skeleton is invariable and the addition of liquid simply fills the space between beads without much affecting the structure of the granular bed. In order to gain a qualitative and quantitative understanding of the voidage fraction variations with the liquid fraction, an X-ray tomography was carried out and will be discussed in the following.

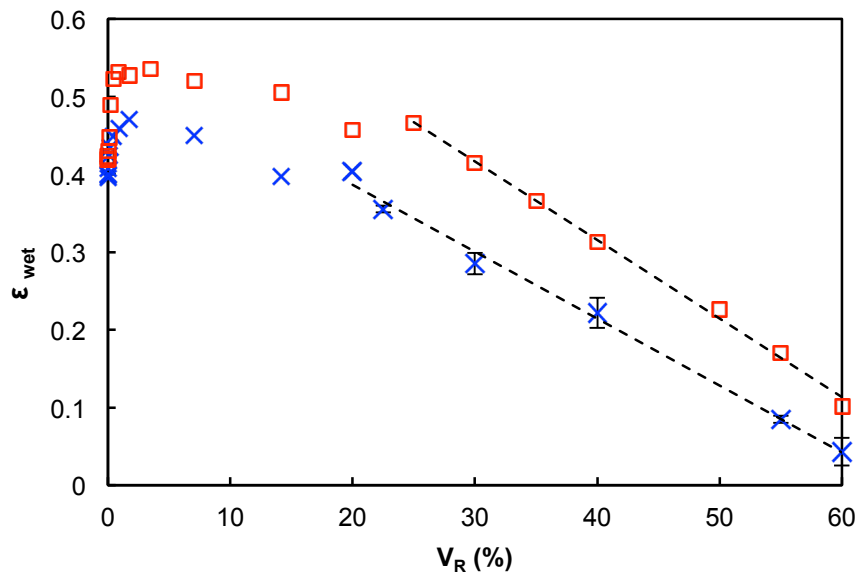


Fig. 4.11. Variation of the voidage fraction ( $\varepsilon_{\text{wet}}$ ) as a function of the liquid fraction. Crosses, for high normal stress (12 kPa) and squares, for low normal stress (1 kPa).

### X-ray tomography

The X-ray tomography technique is used to analyse the structure of the wet glass beads for different liquid fractions; in particular, to analyse the voidage fraction and the distribution of liquid in the granular assembly. Fig. 4.13-left shows 2D cross-sectional images of four samples of wet glass beads with different liquid fractions (0, 0.5%, 3.5% and 40%). These samples have been chosen because they have shown different voidage fraction values (see Fig. 4.1 and Fig. 4.11). From these images we will try to analyse the distribution of the voids in the granular assembly and its dependency on the liquid fraction. The bright areas correspond to the glass beads, the dark areas to the voids and the areas with intermediate intensities of grey to the liquid. It is not obvious to distinguish the three phases in the raw images (on the left). In order to do so, the histograms of the frequency of the intensity of the grey are determined for each sample (see Fig. 4.12). The three phases are clearly distinguished in the histogram of 40% of liquid fraction, i.e. three separated peaks are observed, and this is because the amount of liquid is large enough to give a peak. However, for the sample of 0.5% and 3.5% no peak was detected for the liquid phase due to the small amount of liquid. Yet, if we zoom in the raw images we can see other shades of grey around the bright areas (glass beads), which most likely correspond to the liquid phase. It can be observed in the histogram a large space between the two peaks, which most likely corresponds to the liquid phase. For the dry sample, one clear peak is observed for the glass beads and another small peak for the air phase.

In order to analyse qualitatively and quantitatively the images, a unique colour is attributed to each phase, i.e. white for the glass beads, black for the air and blue for the liquid. The liquid fraction (volume of liquid/volume of glass beads) was checked out for the image of 40% by counting the number of pixels (number of blue pixels/number of white pixels). The liquid fraction calculated is well estimated from the image analysis, about  $40 \pm 2\%$ . This means also that the liquid is evenly distributed in the granular material for high liquid content. For low liquid contents (0.5% and 3.5%), the peak of the liquid phase is not observed therefore the range of grey intensity values, which corresponds to the liquid, is defined such that the liquid fraction is conserved. The treated images are given in Fig. 4.13, on the right hand side, next to the corresponding raw images.

The observation of the treated images shows that the voidage fraction (black pixels) increases with the liquid content increasing. The dry case gives the densest configuration of the granular material since the particles are not cohesive. The observed voids are also evenly distributed in the dry granular material. By adding small amount of liquid (0.5%), small gaps of two or three times the size of the beads are formed and uniformly distributed. Further increase of the amount of liquid to 3.5% leads to increase the size of the gaps. The blue areas are observed at some contact points for the image of 3.5% but not that clear since the amount is yet small. However, it is clearly observed for 40% that the liquid exists at the contact points between beads and also occupies the spaces in between. Large agglomerates coexist with large gaps. The gaps and agglomerates have different sizes and seem to be not uniformly distributed in the granular assembly.

We now will try to quantitatively analyse the voidage fraction from the image analysis. For this aim, different images for each sample have been used in order to calculate an average value of the voidage fraction. The images were chosen in a way that they represent different zones of the sample from the bottom to the top of the capsule (see subsection 3.1.2.2 for the preparation of the sample). For each image, 16 zones have been selected to measure the voidage fraction in order to analyse the distribution of the void depending on the liquid fraction. The voidage fraction in each zone is calculated by counting the number of pixels, the black pixels (volume of void) divided by the number of black, white and blue pixels (total volume) gives  $\epsilon_{\text{wet}}$  as expressed in Eq. 4.1 and observed in Fig. 4.11. The variation of the calculated voidage fraction is in agreement with the variation observed in Fig. 4.11, i.e. the voidage fraction increases with small liquid fraction (0.5% and 3.5%) comparing to the dry case and decreases when the liquid content increases to 40% (see Table 4.1). In order to analyse the distribution of the void depending on the liquid, a relative standard deviation (RSD) is calculated. The RSD is the standard deviation of the values of the voidage fraction of the different selected zones divided by the mean value. We conclude from the values of RSD that the voids are evenly distributed in the dry case and at small liquid fractions (the RSD is about 5%). However, as expected, the increase of the amount of liquid leads to a non-uniformity of the voids in the granular bed (the RSD is about 15%). We conclude that, on the contrary to what was assumed before, large amount of liquid changes the structure of the granular material and not just fills the empty spaces. The liquid at 40% leads to the rearrangement of the glass beads by forming agglomerates and hence forming new gaps in between (see Fig. 4.14). Both gaps and agglomerates have different sizes, which make it hard to measure an average size.

Table 4.1: Values of the voidage fraction  $\epsilon_{\text{wet}}$  and the RSD for each liquid fraction.

<b>Liquid fraction</b>	<i>0</i>	<i>0.5%</i>	<i>3.5%</i>	<i>40%</i>
<b>Average <math>\epsilon_{\text{wet}}</math></b>	<i>0.31</i>	<i>0.46</i>	<i>0.45</i>	<i>0.15</i>
<b>RSD</b>	<i>5%</i>	<i>5.2%</i>	<i>3%</i>	<i>15%</i>

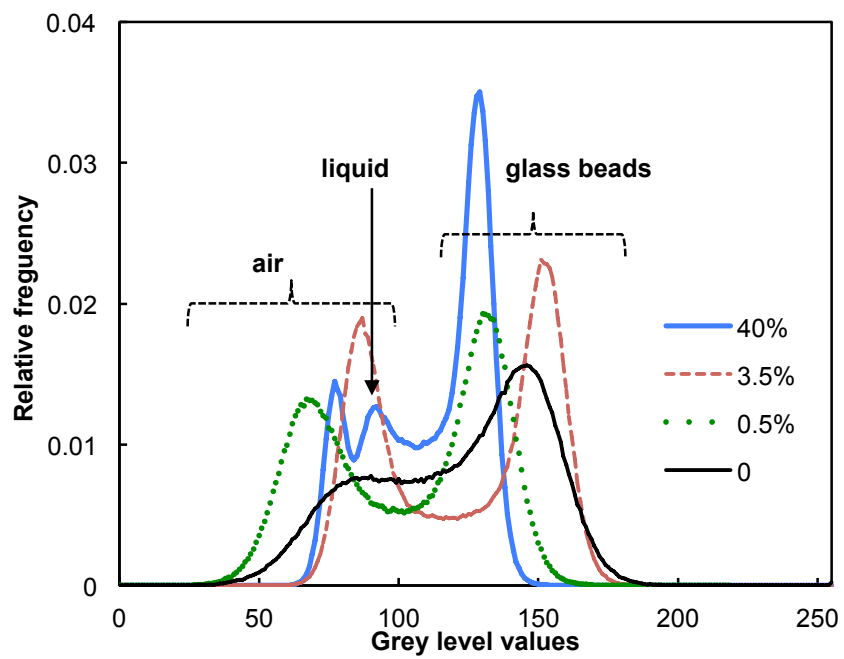
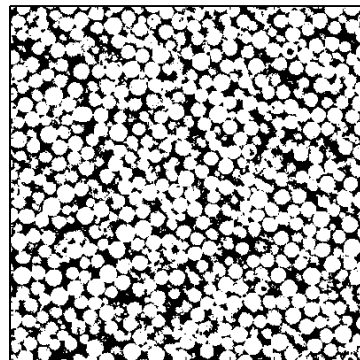
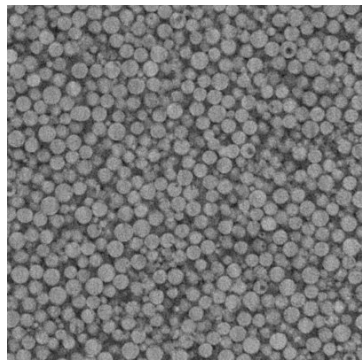
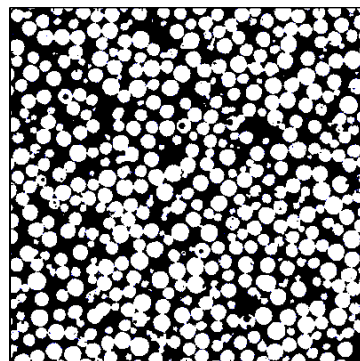
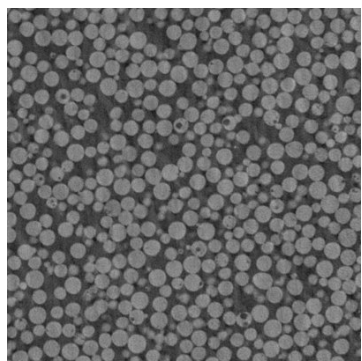


Fig. 4.12. Histograms of the frequency-intensity of grey levels from the raw images. Each peak is attributed to one phase of the wet granular material (glass beads, liquid or air).

dry



0.5%



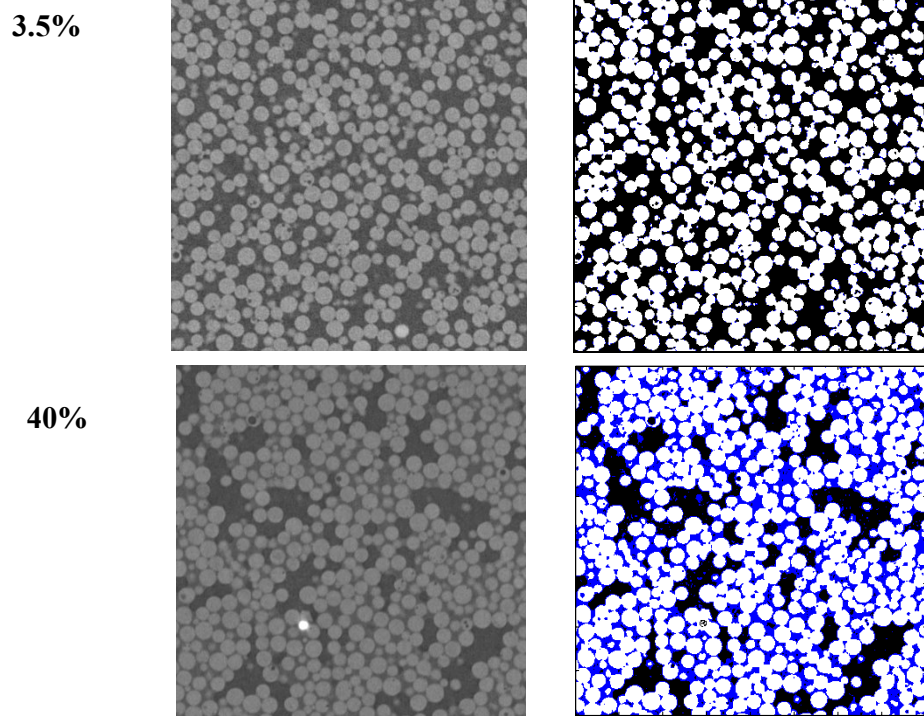


Fig. 4.13. 2-D cross sectional images of wet glass beads of 70-110  $\mu\text{m}$  with different liquid fractions (0, 0.5%, 3.5% and 40%, from the top to the bottom, respectively). On the left, the raw images and, on the right, the treated images. The latter allow to distinguish the three phases, i.e. black: air, white: glass beads, blue: liquid.

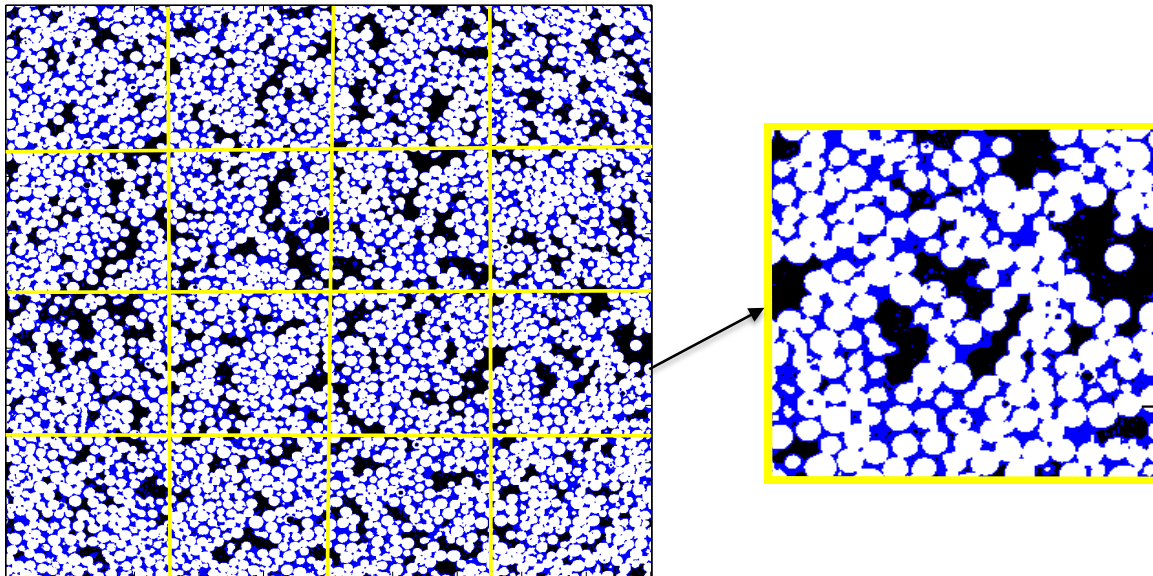


Fig. 4.14. An example of the cut image to define the different zones to calculate the voidage fraction.

#### 4.4.2. Effect of liquid on the shear stress behaviour

In this section, the effect of liquid on the shear behaviour of the glass beads of 70-110  $\mu\text{m}$  is studied for different saturation states of liquid. The shear stress response of the wet glass beads is calculated in the same manner as previously. We are still focusing on the shear stress at steady-state but we choose to present the data using a stress ratio. The latter is the shear stress divided by the corresponding normal stress. The presentation of the data in this manner helps to illustrate better the contribution of the capillary force on the shear stress. Also, it allows distinguishing different regimes of the stress ratio variation depending on the liquid fractions as you can see in Fig. 4.15. We can distinguish four regimes:

**a) For liquid fraction varying between 0.01% – 20%:** an overview of all the data shows that the stress ratio increases with the liquid fraction increasing and decreases by increasing the normal stress. A saturation of the stress ratio values is observed at high normal stress, i.e. the stress ratio becomes independent on the normal stress. Depending on the amount of liquid, this saturation is obtained at different values of the normal stress. Indeed, the value of the critical normal stress (value from which the saturation starts) increases with the liquid fraction. This assumes that the effect of the capillary force is more pronounced at low normal stresses applied to the granular material comparing to the frictional force. Also, the effect of the amount of liquid is more relevant at low normal stresses than at high normal stresses. Another saturation regarding the amount of liquid is observed for liquid fraction from about 3.5% to 20% as it was discussed previously.

**b) For liquid fraction varying between 25% – 40%:** the stress ratio is almost independent on the normal stress. An increase of the stress ratio is observed from 25% to 30% of liquid fraction, however no variation is observed between 30% and 40% where data are superimposed. The X-ray tomography for 40% shows that the regime corresponds to the funicular state of saturation where the glass beads form agglomerates with different gaps in between.

**c) For liquid fraction varying between 50% – 55%:** the stress ratio variation resembles to the one observed in regime a). In comparison with the variation in regime b), the stress ratio values increase at low normal stress but decrease at high normal stress. This means that by applying high normal stress to the wet glass beads, we reduce the voidage fraction and hence we get closer to the capillary regime where the capillary force decreases. The observation of the voidage fraction for 55% at high normal stress shows that the void only presents 10% of the total volume of the granular material (see Fig. 4.11).

**d) For liquid fraction of 60%:** the stress ratio decreases by increasing the normal stress. At high normal stress, the stress ratio joins the value obtained for the dry case. This means that the capillary regime is reached and overcame at high normal stresses since the stress ratio get back to the dry one, i.e. the gaps are totally filled by liquid and the capillary force vanished. Indeed the suction at the interface air–liquid is equal to zero.

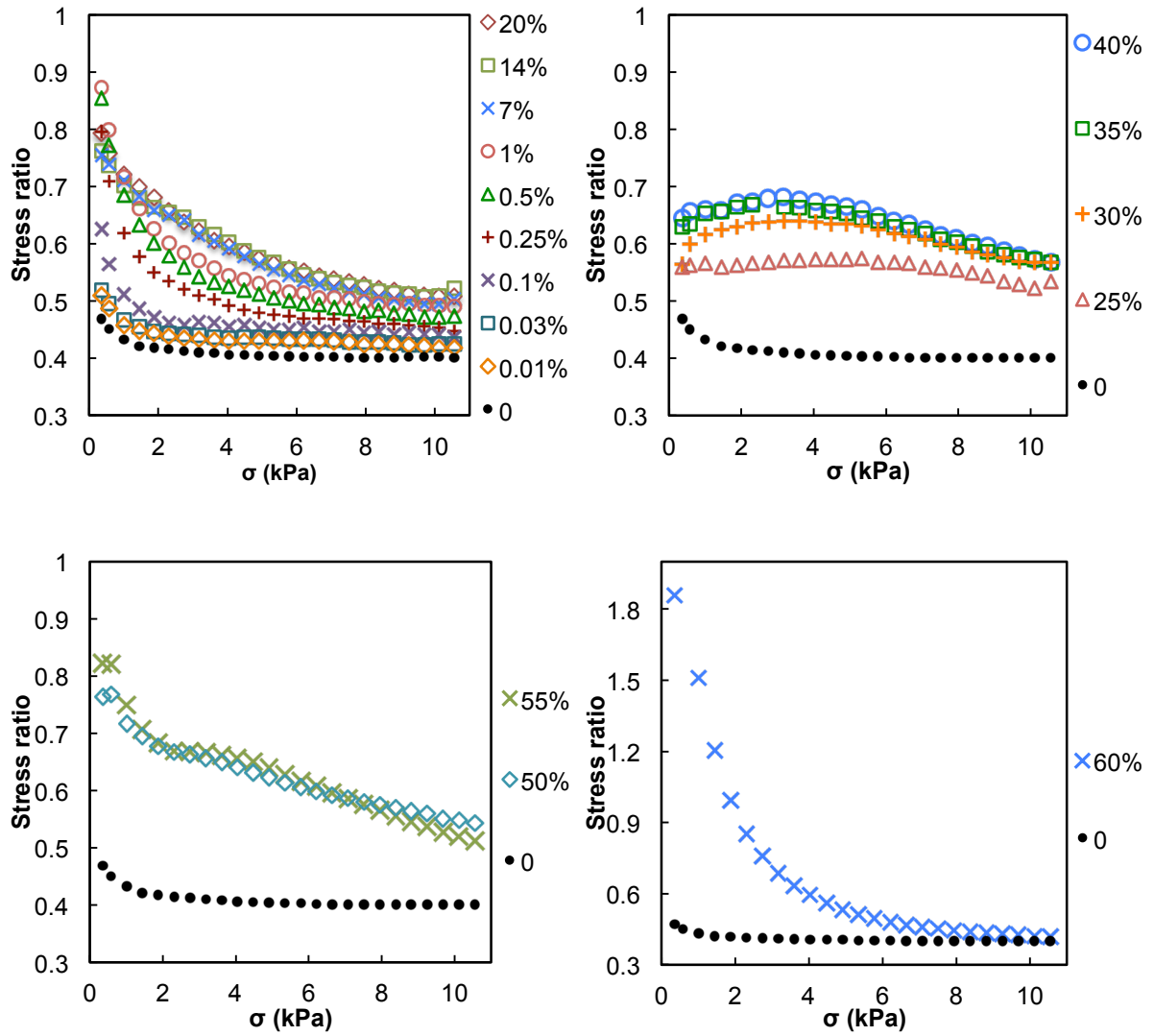


Fig. 4.15. The stress ratio (shear stress/normal stress) variation with the normal stress of different regimes depending on the liquid fraction.

Fig. 4.16 shows the variation of the mean value of the stress ratio calculated at high normal stress between 8 kPa and 11 kPa as a function of the liquid fraction in the range of 0.01% to 60%. The shear stress evolution of the wet glass beads can be analysed from this graph. First, an increase of the shear stress with the liquid is observed until saturation is reached. The stress ratio goes up from 0.4 to 0.5 just by adding 1% of liquid. After saturation, the shear stress increases again from about 0.5 to 0.6 when the liquid fraction goes from 20% to 40%. At around 40%, the maximum shear stress is observed and after that any increase of liquid leads to decrease the stress.

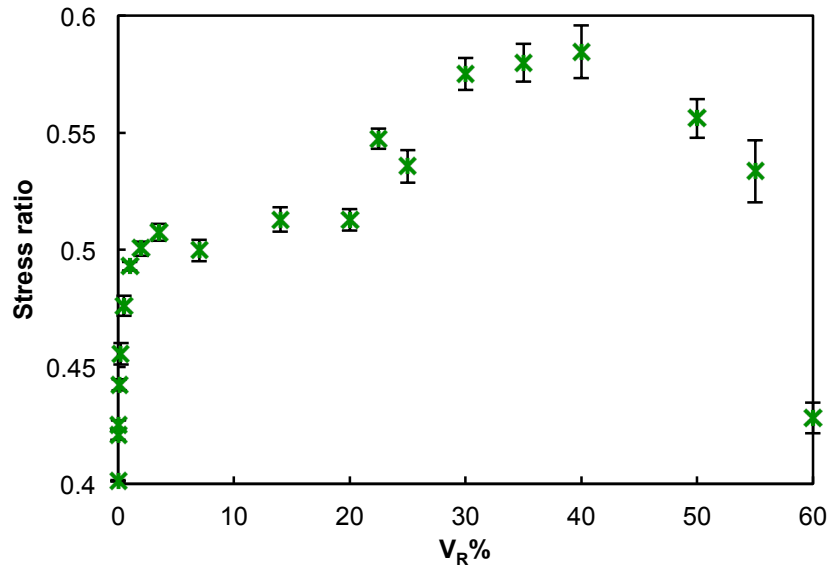


Fig. 4.16. Variation of the average stress ratio for normal stress between (8–11 kPa) with the liquid fraction.

#### 4.5. Conclusions

We have studied the shear resistance of wet glass beads, in a steady-state regime and for a wide range of applied normal stresses and liquid fractions. The experimental results show that the shear stress is dependent on both liquid fraction and applied normal stress.

First, we focused on a partially state of saturation of glass beads of 70–110  $\mu\text{m}$ . A non-linear relationship of the shear stress – normal stress was observed, implying three different regimes as discussed in section 4.2.2. In particular, a residual cohesion was observed at steady-state for enough liquid content. The other result of the addition of liquid is the increase in the voidage fraction of wet particle bed resulting from the emergence of gaps due to the formation of liquid bridges. After reaching a maximum value, the voidage fraction declines and tends to its initial value (the voidage fraction under dry conditions). In order to quantify the capillary forces, responsible of the shear resistance and the variation of the voidage fraction of the granular material, the tensile strength was evaluated from experimental data and theoretically estimated using the Rumpf model. The observed tensile strength is found to increase with the capillary forces when more liquid is added. However, the dependence of  $T_s$  on the coordination number leads to distinction between two states of wet granular medium. A dense configuration occurring at high-applied normal stress leads to an increase in the coordination number and then in the number of capillary bridges broken under traction. A loose configuration, at low applied normal stress, leads to a reduction in the coordination number and the preservation of some contact between particles under traction because of the rolling rearrangements. This leads to a reduction in the magnitude of the tensile strength.

Second, we analysed the effect of particle size on the shear behaviour of partially wet glass beads. It was observed that the saturation in liquid depends on the particle size. The voidage



fraction of wet glass beads increases by decreasing the particle size. And the shear stress response to the applied normal stress can be different. We have shown also that the tensile strength increases for the smaller particle size because of the increase in the contact number and the liquid bridges broken in the shearing plane. However, the lower packing density of the small glass beads leads to a lower tensile strength values estimated experimentally.

Third, we investigate the effect of more liquid fractions on the shear behaviour of glass beads of 70-110  $\mu\text{m}$ . The shear stress increases with the liquid up to a critical value and then decreases. The capillary force contribution on the shear stress vanishes at the capillary state of saturation. Regarding the voidage fraction, a linear decrease is observed for liquid fraction in the range of 20% to 60%. And the tomography analysis showed that the increase of liquid beyond the pendular state leads to the formation of agglomerates. The effect of liquid in the funicular and capillary regimes has been investigated further using theoretical models and compared with experiments. The theoretical and experimental approaches together provide a better understanding of the granular material behaviour under shearing. This part of the study will be published as open-access papers in a dedicated volume on the EPJ Web of Conferences (<http://www.epj-conferences.org>) prior to the beginning of the conference « Powder and Grains » on July 3, 2017.

## **Conclusions (en Français)**

Nous avons étudié la résistance au cisaillement des billes de verre humide, en régime stationnaire et pour une large gamme de contraintes normales appliquées et de fractions de liquide. Les résultats expérimentaux montrent que la contrainte de cisaillement dépend de la fraction de liquide et de la contrainte normale appliquée.

D'abord, nous nous sommes concentrés sur un état de saturation partiel en liquide des billes de verre de 70-110  $\mu\text{m}$ . Une relation non linéaire de contrainte de cisaillement - contrainte normale a été observée impliquant trois régimes différents, tel que discuté dans la section 4.2.2. En particulier, une cohésion apparente a été observée en régime stationnaire pour une teneur en liquide suffisante. Une augmentation de la porosité du lit granulaire humide a été également observée suite à la formation de ponts liquides. Après une valeur maximale, la porosité diminue et tend à la valeur initiale (la fraction de vide à l'état sec). Afin de quantifier les forces capillaires, responsables de la résistance au cisaillement et de la variation de la porosité, la résistance à la traction ( $T_s$ ) a été évaluée à partir de données expérimentales et modèles théoriques (modèle de Rumpf). La résistance à la traction augmente avec les forces capillaires suite à l'augmentation de la teneur en liquide. Nous distinguons deux régimes du comportement du milieu granulaire humide. Une configuration dense sous une contrainte normale élevée entraîne une augmentation du nombre de coordination ainsi que le nombre de ponts capillaires brisés sous traction. Une configuration lâche, à faible contrainte normale appliquée, conduit à une réduction du nombre de coordination et à la préservation de certains ponts liquide à cause de réarrangement de roulement des billes. Ceci conduit à une diminution de la résistance à la traction.

Ensuite, nous avons analysé l'effet de la taille des particules sur le comportement au cisaillement des billes de verre partiellement humides. Nous avons observé que la saturation en liquide dépend de la taille des particules. La porosité des billes de verre humides augmente en diminuant la taille des particules et un changement du régime de la réponse au cisaillement en fonction de la contrainte normale appliquée. Nous avons également montré que la résistance à la traction augmente pour les petites particules en raison de l'augmentation du nombre des ponts liquides brisés par unité de surface dans le plan de cisaillement. Cependant,  $T_s$  reste aussi faible à des faibles contraintes normale à cause d'une porosité élevée du lit granulaire.

Puis, nous avons étudié l'effet de l'augmentation de la fraction de liquide sur le comportement au cisaillement des billes de verre de 70 - 110  $\mu\text{m}$ . La contrainte de cisaillement augmente avec le liquide jusqu'à une valeur critique et diminue ensuite. La contribution de la force capillaire sur la contrainte de cisaillement disparaît à l'état capillaire de saturation. En ce qui concerne la porosité, une diminution linéaire est observée pour les fractions de liquide entre 20% et 60%. Et l'analyse tomographique a montré que l'augmentation du liquide au-delà de l'état pendulaire conduit à la formation des agglomérats. L'effet du liquide dans les régimes funiculaire et capillaire a été étudié plus en détail à l'aide de modèles théoriques et comparé à des expériences. Les approches théoriques et expérimentales permettent de mieux comprendre le comportement du matériau granulaire sous cisaillement. Cette partie de l'étude sera publiée sous forme de documents à accès libre dans un volume dédié sur le site Web des conférences de l'EPJ (<http://www.epj-conferences.org>) avant le début de la conférence «Powder and grains» en juillet , 2017.

## References

- Adams, M. and Perchard, V., 1985. The cohesive forces between particles with interstitial liquid. *Inst. Chem. Eng. Symp.*, 91, 147–160.
- Bocquet, L., Charlaix, É., and Restagno, F., 2002. Physics of humid granular media. *Comptes Rendus Phys.*, 3, 207–215.
- Carr, J.F., 1967. Tensile strength of granular materials. *Nature*, 213(5081), 1158–1159.
- Feng, C.L. and Yu, A.B., 1998. Effect of liquid addition on the packing of mono-sized coarse spheres. *Powder Technol.*, 99, 22–28.
- Fisher, R., 1926. On the capillary forces in an ideal soil; correction of formulae given by W. B. Haines. *J. Agric. Sci.*, 16, 492–505.
- Fraysse, N., Thomé, H., and Petit, L., 1999. Humidity effects on the stability of a sandpile. *Eur. Phys. J. B*, 11, 615–619.
- Hornbaker, D., Albert, R., Albert, I., Barabasi, A. and Schiffer, P., 1997. What keeps sandcastles standing? *Nature*, 387, 765.
- Louati, H., Oulahna, D. and de Ryck, A., 2015. Apparent friction and cohesion of a partially wet granular material in steady-state shear. *Powder Technol.*, 278, 65–71.
- Lu, N., Wu, B. and Tan, C., 2007. Tensile strength characteristics of unsaturated sands. *J. Geotech. Geoenviron. Eng.*, 133(2), 144–154.
- Mitarai, N. and Nori, F., 2006. Wet granular materials. *Advances in Physics*, 55, 1–45.
- Moller, P.C.F., and Bonn, D., 2007. The shear modulus of wet granular matter. *EPL journal*, 80, 1–5.
- Oulahna, D., Collet, R., and de Ryck, A., 2012. Mechanical resistance due to shearing of partially wet granular media. *KONA: Powder & particle journal*, 30, 109.
- Pietsch, W., 1968. Tensile strength of granular materials. *Nature*, 217, 736.
- Pietsch, W., 2002. *Agglomeration Process*, Wiley-VCH, Weinheim.
- Rabinovich, Y.I., Esayanur, M.S. and Moudgil, B.M., 2005. Capillary forces between two spheres with a fixed volume liquid bridge: theory and experiment. *Langmuir*, 21, 10992–10997.
- Rondet, E., Ruiz, T. and Cuq, B., 2013. Rheological and mechanical characterization of wet agglomerates processed in low shear mixer. *J. Food Eng.*, 117, 67–73.
- Rumpf, H., 1962. The strength of granules and agglomerates. *Intersci. Publ.*, 379–418.
- Schubert, H., 1984. Capillary forces: modeling and application in particulate technology. *Powder Technol.*, 37, 105–116.
- Seville, J.P.K., Willett, C.D. and Knight, P.C., 2000. Interparticle forces in fluidisation: a review. *Powder technol.*, 113, 261–268.
- Simons, S., Seville, J. and Adams, M., 1994. An analysis of the rupture energy of pendular liquid bridges. *Chem. Eng. Sci.*, 49, 2331–2339.

Yu, A.B., Bridgwater, J. and Burbidge, A., 1997. On the modelling of the packing of fine particles. *Powder Technol.*, 92, 185-194.

Yu, A.B., Feng, C.L., Zou, R.P. and Yang, R.Y., 2003. On the relationship between porosity and interparticle forces. *Powder Technol.*, 130, 70-76.

## Appendices: Observations of the Stick-slip motion

In this appendix, we investigate the stick-slip motion observed during our experimental study with the glass beads 70-110  $\mu\text{m}$ , for the dry and wet cases. This stick-slip motion can be observed in the shear stress signal as an oscillation, which depends on the applied normal stress and the liquid content. In the following, we analyse the shear stress signal, we discuss the choice of the steady-state shear stress value in the presence of the stick-slip motion and we show the effect of the liquid content and the normal stress on the amplitude of the stick-slip.

### Appendix. 4.1. The steady-state shear stress signal

The response of the shear stress signal for dry glass beads seems constant and reaches a plateau value for all the normal stresses applied, as shown in Fig. 1. This is not the case for wet glass beads sheared at a sufficiently high normal stress, for which an oscillatory stick-slip motion takes place. Such a stick-slip motion may be observed with a velocity-weakening friction coefficient if the granular bed-shear apparatus is not stiff enough (Schulze, 2003; Lubert, 2001). The amplitude of the signal increases with the normal stress applied to the granular material (see Fig. 1). It is also observed that the period of the oscillation increases with the normal stress and the response changes from sinusoidal wave at low normal stress to saw-tooth wave at high normal stress (see Fig. 2). This means that the sticking phase last longer at high normal stress since the granular material is more compacted and more liquid bridges are consequently needed to be broken. Nevertheless, this can be observed for dry granular material in the presence of inter-particle forces such as Van-der-Waals force. The sliding phase is more brutal at high normal stress compared to at low normal stress (see Fig. 2).

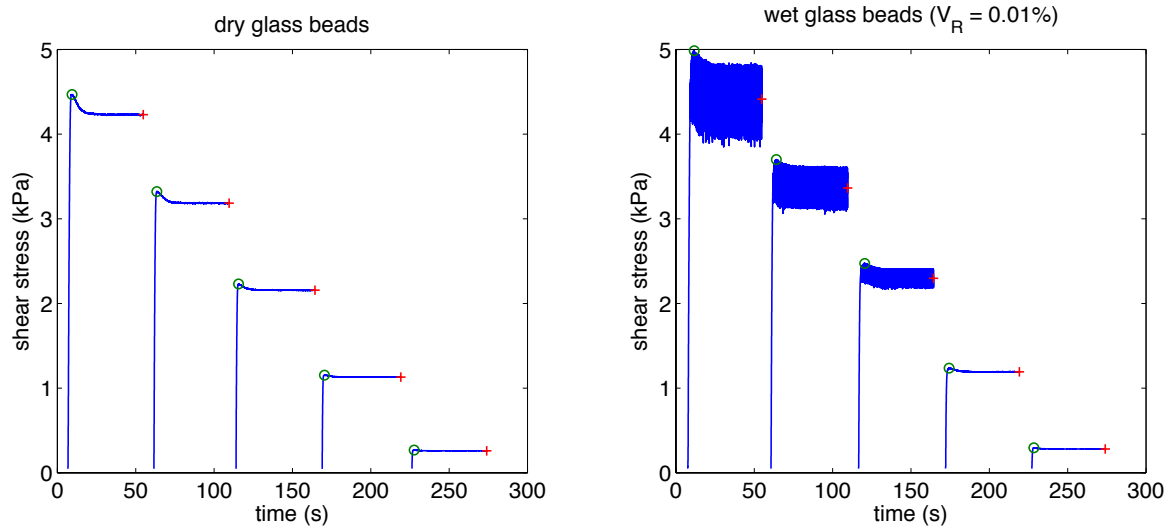


Fig. 1. Shear stress versus time during shearing for some normal loading (24 kg, 18 kg, 12 kg, 6 kg and 1 kg, from left to right). (left) Dry glass beads and (right) wet glass beads with  $V_R = 0.01\%$ . (circle) For the yield locus and (plus) for the mean shear stress at steady-state.

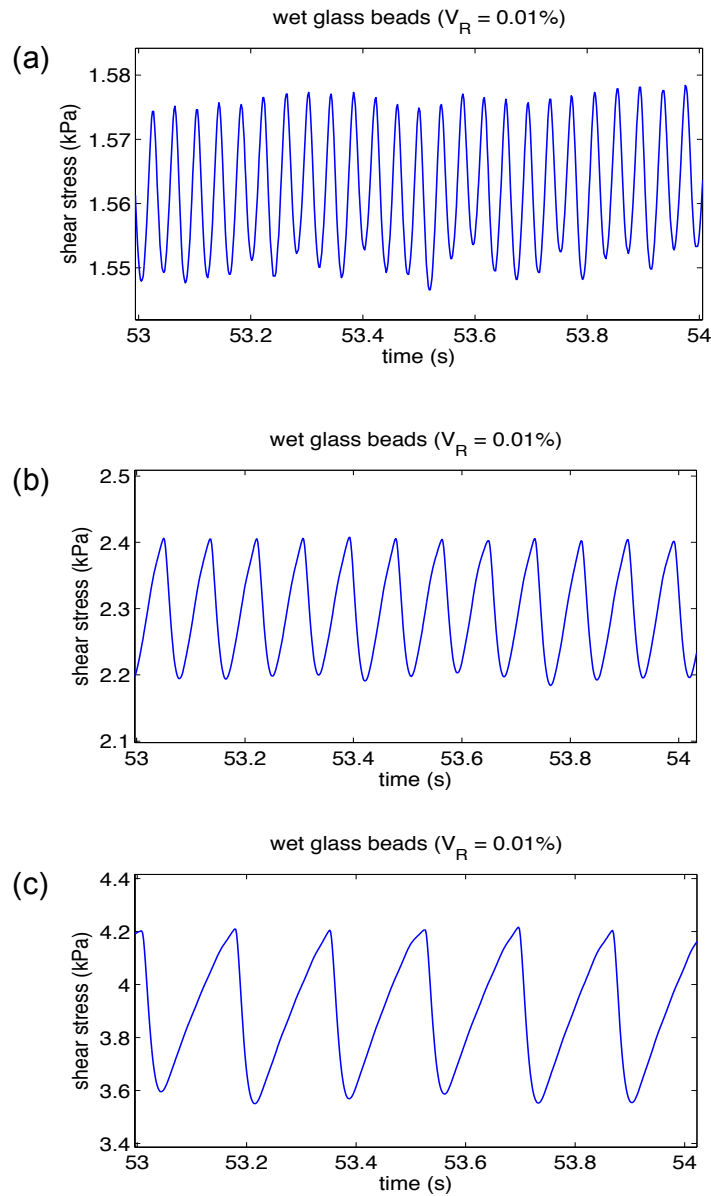


Fig. 2. Comparison of the stick-slip motion of wet glass beads ( $V_R = 0.01\%$ ) for different normal loadings applied to the granular material (a) at 8 kg, (b) at 12 kg and (c) at 21 kg.

#### Appendix. 4.2. The choice of the steady-state shear stress value

The oscillatory behaviour of the shear stress at steady-state is treated by computing the mean value  $\tau$  and the standard deviation  $\Delta\tau$ . Fig. 3 shows the mean signal (circles) and  $\tau \pm \Delta\tau$  for the sample with a volume fraction of 0.01%. As can be observed,  $\Delta\tau$  increases in an approximately linear relationship with normal stress to reach 0.3 kPa at about  $\sigma = 11$  kPa, after a threshold value of normal stress around 3 kPa. The shear stress oscillates within a maximum range of 10 %, and consequently only the mean value will be used afterwards. In the same Fig. 3, it may be observed that this mean value should be close to the constant value that would be observed for

a stiffer system, since it remains close to that extrapolated from the behaviour at low normal stress (continuous line). The standard deviation may increase by increasing the liquid fraction, which will be discussed in the next subsection.

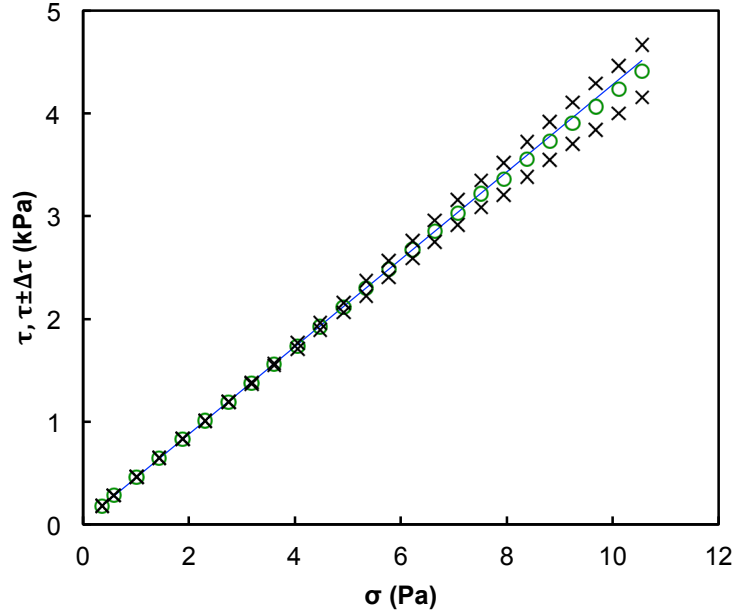


Fig. 3. Mean shear stress  $\tau$  (circles) and  $\tau \pm \Delta\tau$  (crosses) plotted as a function of the normal stress  $\sigma$  for a liquid fraction of 0.01%. The straight line is the extrapolated linear behaviour at low normal stress, without stick-slip.

#### Appendix. 4.3. Effect of the liquid fraction on the amplitude of the stick-slip response

Fig. 4 gives the standard deviation variation with the normal stress for various liquid fractions. This standard deviation gives an idea about the amplitude of the stick-slip response. The idea is to check whether a relationship between the amplitude of the stick-slip response and the liquid fraction can be established. We first investigate the unsaturated state of liquid up to 20% of the liquid fraction in Fig. 4-a. Generally, we observe an increase of  $\Delta\tau$  with the liquid fraction increasing. As mentioned above, the stick-slip appears after a threshold value of normal stress. We can also observe a regime change when the liquid fraction reaches a certain level. This change appears as an increase of the  $\Delta\tau$  values and an earlier appearance of the stick-slip at lower normal stresses. By increasing the liquid fraction beyond 20%, the  $\Delta\tau$  continues to increase at high normal stresses, however it is not always the case at low normal stresses (see Fig. 4-b). At 60% of the liquid fraction, when the capillary state is reached, the stick-slip effect decreases at high normal stress but increase at low normal stress. It was observed during the experiment that the wet granular material is drowned at high normal stress, which means that the system is approaching the slurry regime. This effect gradually disappears by decreasing the normal stress, which may explain the variation observed in Fig. 4-b.

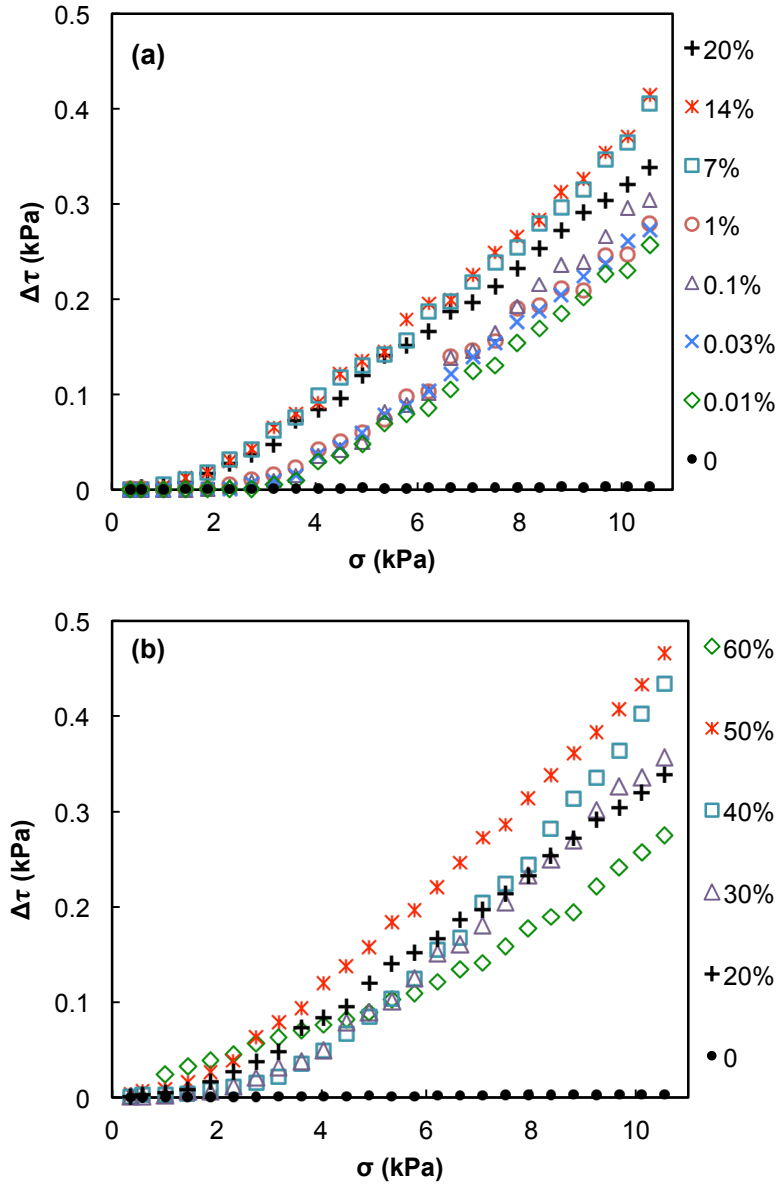


Fig. 4. The standard deviation,  $\Delta\tau$ , variation as a function of the normal stress for different liquid fraction. (a) unsaturated state of liquid  $V_R$  up to 20% (b) wet glass beads toward saturation of liquid,  $V_R$  in the range of 20% to 60%.

#### Appendix. 4.4. Conclusions

In this study we have shown that the mean value of the steady-state shear stress is appropriated to get ride of the stick-slip disturbance. The analysis of the stick-slip motion shows the influence of the liquid fraction on the signal response; the amplitude of the stick-slip motion, generally, increases with the liquid fraction. Moreover, the stick-slip motion appears earlier (at lower normal stress) for an increase in the liquid fraction. This simple analysis of the stick-slip motion shows that this undesirable effect can be used to analyse some aspect of the granular material behaviour and more investigation in this subject is required.





## Chapter 5. Discrete element analysis of the shear behaviour of dry and partially wet granular material

---

### Résumé:

Dans le chapitre précédent, nous avons analysé le comportement d'un milieu granulaire partiellement humide à partir des essais expérimentaux de cisaillement. Les résultats ont montré l'effet du liquide sur la contrainte de cisaillement et la porosité de milieu qui dépend à la fois de la fraction de liquide et de la contrainte normale appliquée. Nous nous sommes servis d'un modèle théorique pour estimer la traction et expliquer la résistance mécanique à partir des ponts liquides en jeu.

Dans le même contexte, la méthode numérique des éléments discrets (DEM) est utilisée dans ce chapitre afin d'acquérir une compréhension microscopique du comportement de milieu granulaire sec et humide. Dans ce but, nous avons mené en parallèle des tests de cisaillement expérimentaux et numériques. Des billes de verre de grande taille (2 mm de diamètre) ont été utilisées afin d'accélérer le calcul et de faciliter la caractérisation à l'échelle de particule. En premier lieu, nous avons mesuré expérimentalement le module de Young et la friction de glissement de particules pour obtenir les paramètres d'entrée pour la simulation. Dans un second lieu, nous avons analysé l'effet de la variation de ces paramètres sur le comportement macroscopique en simulation de milieu granulaire sec et humide. Nous avons observé que la diminution de la valeur de module de Young réduit le temps de calcul mais peut affecter les résultats obtenus. Pareillement, la variation de la friction de glissement de particule affecte le comportement de milieu granulaire. Cet effet est comparé dans le cas sec et humide de milieu granulaire. Dans un troisième lieu, nous nous sommes intéressés à l'effet de la fraction de liquide et de la contrainte normale appliquée dans la simulation. Nous avons observé que les forces capillaires sont plus significatives à faible contrainte normale en présence de forces de contact relativement faibles. L'évaluation de nombre de ponts liquides montre une augmentation de ces derniers avec l'augmentation de la contrainte normale puis une saturation à fortes valeurs.

### Abstract:

The behaviour of partially wet granular material has been studied using shear test experimentation in the previous chapter. The results show that the effect of the liquid on the shear stress and the voidage fraction depends on the liquid fraction and the normal stress

applied. A theoretical model was used to estimate the tensile strength and to explain the mechanical resistance of the wet granular material depending on the capillary forces in play.

In the same context, numerical simulations are carried out in this chapter by the use of the discrete element method (DEM) in order to gain a microscopic understanding of the shear behaviour of dry and wet granular material. For this purpose, experimental and simulated shear tests have been set up. Large glass beads, 2 mm in diameter, were used for speeding up the computations and to facilitate characterisation at the particle scale. Firstly, the Young's modulus and the sliding friction of glass beads were experimentally measured and compared with the literature. Secondly, the effects of the variation of these parameters on the macroscopic behaviour of dry and wet granular material were analysed in the simulation. It is observed that the decrease of the Young's modulus value decreases significantly the computations time but may affect the simulated results if it is too reduced. The variation of the particle sliding friction does also affect the stress ratio, the voidage fraction, the coordination number and the average velocity of particles. A comparison of this effect on the dry and wet granular material is discussed. Finally, the effect of the liquid fraction and the normal stress applied was analysed in the simulation. It is observed that the capillary forces are significant at low normal stress in the presence of relatively low normal contact forces. An increase of the number of liquid bridges with the normal stress is observed at low normal stresses (less than 5 kPa), however this number saturates at high normal stresses.

## 5.1. Introduction

The flow behaviour of granular materials has long been characterised by shear cell testing. The method has been successful in process equipment design, but has shortcoming in predicting the cohesive powder flow behaviour, such as arching. For a better understanding of complex phenomena, a microscopic analysis of the role of inter-particle forces, particle properties, environmental conditions and external forces is needed. Discrete element method (DEM) is an ideal method to gain a microscopic understanding of granular material phenomena. This method was first used for non-cohesive particles and many models have been developed to approach more realistic behaviour of granular materials. Models have been adapted later to study the cohesive state by including inter-particle forces in the equation of motion of particles or taking into consideration some external factors, such as liquid bridges in the case of wet granular material. Some models, intended for cohesive powder, now exist in the literature. However, an accurate model itself cannot guarantee realistic results from the DEM simulation. It is of crucial importance to properly define the input parameters of the individual particle properties such as the friction coefficient, Young's modulus and plastic yield stress, etc. In the literature, different research studies have been reported using glass beads as a model of spherical particles, yet a wide range of the input parameter values was used. Thus, experimental measurements of these parameters have been performed and discussed.

In this Chapter, we analyse the shear behaviour of dry and partially wet granular material. The first part is dedicated to study the effect of the Young's modulus and the particle sliding friction coefficient on the bulk behaviour. The second part is concerned with the analysis of the behaviour of partially wet glass beads in the presence of varying liquid loading. For this purpose, shear test experiments and simulations have been performed. The effect of the particle sliding friction on the stress ratio, the voidage fraction, the number of coordination (the number of liquid bridge in the wet case) and the velocity of particles are analysed. The effect of liquid on the shear behaviour of wet granular material is quantitatively evaluated.

## 5.2. Materials and methods

### 5.2.1. Shear test experiment

The shear behaviour of dry and partially wet glass beads has been studied experimentally using the small shear cell of the experimental Schulze shear tester for comparison purposes. The shear cell geometry dimensions and the rotational speed are given in Table 5.1. The shear test was performed for different applied normal stresses from about 12 kPa to 1 kPa. More descriptions of the shear test procedure can be found in chapter 3. Glass beads of 2 mm ( $\pm 0.2$  mm) in diameter have been used in this work. This relatively large size was chosen in order to facilitate the characterisation of the granular materials. The density of the glass beads is  $2.54 \text{ g.cm}^{-3}$  and the voidage fraction is 0.43 in the dry conditions.

To study the effect of liquid on the shear behaviour of the granular material, the beads were mixed with small quantities of PEG 400 such that the liquid forms liquid bridges. The fraction of liquid amount is expressed as a volume ratio ( $V_R\% = \text{volume of liquid} / \text{total volume of}$

particles) and is ranging from 1% to 7%. A granular bond number  $Bo$  was calculated in order to compare the capillary force to the gravitational force. This number is the ratio of the maximum capillary force and the weight of the particle ( $Bo = 3\gamma/2R^2\rho g$ ) (Nase *et al.*, 2001). In this case, the magnitude of the capillary force is estimated to be about 4 times that of the gravitational force.

Table 5.1: The shear cell geometry parameters and rotational speed.

Parameters	Values
External radius (cm)	6
Internal radius (cm)	3
Height of bars (cm)	0.4
Height of the bed (cm)	2
Rotational speed (rpm)	0.05

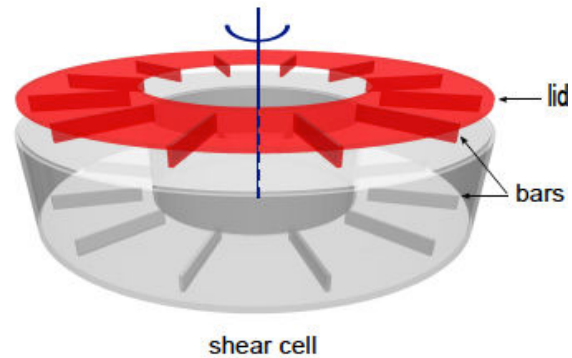


Fig. 5.1. Shear cell designed for the simulation. It has the same geometry dimensions as the shear cell used for experiment.

### 5.2.2. Shear test simulation

The simulation was performed using EDEM<sup>TM</sup> software (version 2.7) from DEM\_Solutions Ltd, Edinburgh, UK. The shear test simulation was performed in a similar way to the experiment; the shear cell geometry dimensions, the number of particles in the shear cell and their size and density were based on experimental data. The particle size distribution of the simulated glass beads is given in Fig. 5.2.

The input parameters of the material properties are given in Table 5.2. As already mentioned the coefficient of sliding friction and the Young's modulus of glass beads have been measured experimentally. The coefficient of sliding friction of glass–steel contact has also been measured (the steel is the material of the chamber and the lid of the shear cell). The rest of parameters have been used from the literature after reviewing their effect in the simulation: the coefficient of restitution is decisive for simulation with high impact velocities. In this work, the rotational speed of the shear cell is relatively low and hence the coefficient of restitution does not affect significantly the motion of particle. The glass–glass coefficient of restitution found in the literature is between 0.6 – 0.95 (Baharadwaj *et al.*, 2010) and for our simulation the value of 0.6 was chosen and was kept constant. The coefficient of rolling friction depends on the particle shape and surface properties. Typical value of spherical glass beads in the literature is in the range of 0 – 0.01 (Zhou *et al.*, 1999; Zhou *et al.* 2002; Stewart, 2001). A value of 0.01 has been chosen for glass–glass and glass–steel contacts.

To run a shear test simulation, the chamber was first filled with particles under the action of their weights. After the particles were settled down, the required normal stress is applied to the particle bed by moving down the lid over the granular material. The normal stress is maintained constant during the shearing process by controlling the movement of the lid. The rotational speed of the experimental shear cell is about 0.05 rpm. This speed was increased for the simulation to 1 rpm in order to reduce the simulation time, i.e. the steady-state regime is reached within a short time by increasing the rotational speed. It has been reported by Tardos *et al.* (2003) that the shear stress is independent on the shear rate for the so-called slow frictional regime (quasi-static regime). The latter is ensured for a dimensionless shear rate,  $\bar{v}$  up to 0.2. This shear rate depends on the particle diameter,  $d$ , and the gravitational acceleration,  $g$ , and it is given by this relationship:

$$\bar{v} = v * \sqrt{d/g}. \quad \text{Eq. 5.1}$$

For a particle with a diameter of 2 mm and a rotational speed not exceeding 1 rpm, the dimensionless shear rate is ( $\bar{v} < 0.005$ ), this means that we are largely under the limit value of the frictional regime. Nevertheless, a comparative simulation was run for a shear cell rotational speed of 0.05 rpm to check out if there is any effect on the shear stress response. At low speed the simulation takes long time to reach the steady-state regime but converges toward the same average value of the shear stress obtained for high speed (see Appendix 5.1). Reducing the rotational speed of the shear cell allows to gain in the simulation time since we focus on the steady-state regime.

Table 5.2. The input parameters of the particle properties in the simulation.

Variables	Values
Number of particles	28000
Young's modulus (GPa)	to be varied
Poisson's ratio	0.3
Coefficient of restitution	0.6
Sliding friction coefficient (p-p)	to be varied
Sliding friction coefficient (p-w)	0.46
Rolling friction coefficient	0.01

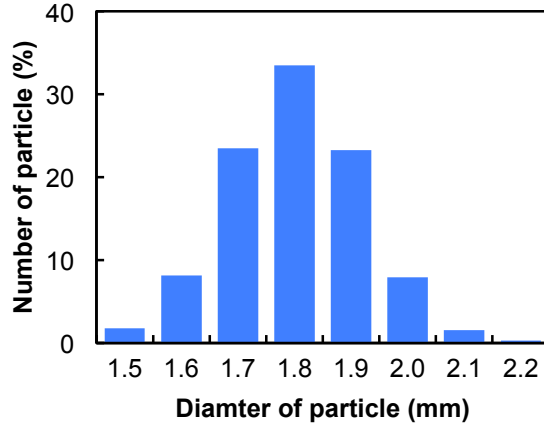


Fig. 5.2. The particle size distribution in the simulation.

### 5.2.3. Models used for the simulation

- **Hertz-Mindlin model**

In order to study the shear behaviour of dry granular material, the well-known Hertz-Mindlin model was used. The expressions of the contact forces implied in this model were given in chapter 2.

- **Liquid bridge model**

The liquid bridge DEM algorithm used for the simulation was set up by Remy *et al.* (2012) to study the effect of wet granular flows in a bladed mixer, and it was adopted later by DEM\_Solutions. This liquid bridge model is based on the model developed by Mikami *et al.* (1998), which consists of a regression expression of the numerical solution of the Young-Laplace equation. The capillary force is expressed as a function of the liquid bridge volume and the separation distance between particles:

$$\hat{F}_c = \exp(A\hat{h} + B) + C, \quad \text{Eq. 5.2}$$

where the normalized bridge force is  $\hat{F}_c = F_c/\pi R_{eff}\gamma$ , the dimensionless separation distance is  $\hat{h} = h/R_{eff}$  and  $A$ ,  $B$  and  $C$  are parameters given as:

for sphere-sphere contact

$$A = -1.1\hat{V}^{-0.53}, \quad \text{Eq. 5.3}$$

$$B = (-0.34\ln\hat{V} - 0.96)\theta_L^2 - 0.019\ln\hat{V} + 0.48, \quad \text{Eq. 5.4}$$

$$C = 0.0042\ln\hat{V} + 0.078, \quad \text{Eq. 5.5}$$

and for sphere-wall contact by

$$A = -1.9\hat{V}^{-0.51}, \quad \text{Eq. 5.6}$$

$$B = (-0.016\ln\hat{V} - 0.76)\theta_L^2 - 0.012\ln\hat{V} + 1.2, \quad \text{Eq. 5.7}$$

$$C = 0.013\ln\hat{V} + 0.18. \quad \text{Eq. 5.8}$$

$A$ ,  $B$  and  $C$  are calculated from the dimensionless liquid bridge volume ( $\hat{V} = V/R_{eff}^3$ ) and the contact angle  $\theta_L$ . The effective radius,  $R_{eff}$ , is defined for particle-particle contact according to Derjaguin approximation (Willett, 2000) as follow:

$$R_{eff} = \frac{2R_i R_j}{R_i + R_j}. \quad \text{Eq. 5.9}$$

In the case of particle-wall contact, the radius of the particle is used instead of the effective radius.

The critical separation distance, which results on the breaking of the liquid bridge, is obtained by regression expressions similar to the relationship given by Lian *et al.* (1993). The separation distances are given respectively for sphere-sphere and sphere-wall contacts by

$$\hat{h} = (0.62\theta_L + 0.99)\hat{V}^{0.34}, \quad \text{Eq. 5.10}$$

$$\hat{h} = (0.22\theta_L + 0.95)\hat{V}^{0.32}, \quad \text{Eq. 5.11}$$

where the normalized separation distance ( $\hat{h} = h/R_{eff}$ ) depends on the contact angle  $\theta$  (rad) and the liquid bridge volume  $\hat{V}$ .

The liquid bridge volume is defined according to Shi and McCarthy model (Shi and McCarthy, 2008); the bridge volume is the contribution of liquid from the surface of contact of two particles. The liquid volume from each contact surface is defined as the volume of a spherical cap, which is defined by tangential lines from the centre of one particle to the surface of the other particle. For example, the liquid volume contributed from particle  $i$  is expressed as:

$$V_i = \frac{L_i}{2} \left( 1 - \sqrt{1 - \frac{R_j^2}{(R_i + R_j)^2}} \right), \quad \text{Eq. 5.12}$$

where  $L_i$  is the total liquid volume on the surface of particle  $i$ . The total liquid bridge volume at the contact between two particles  $i$  and  $j$ , is  $V = V_i + V_j$ . In the case of sphere-wall contact, the liquid bridge volume is obtained only from the liquid within the spherical cap on the sphere surface.

- **Liquid distribution in the granular material**

Initially, the volume of liquid is evenly distributed on the particles bed. The liquid bridge is formed when particles come into contact between each other or with the geometry walls, and the volume of the bridge is computed as described above. The bridge is broken when the separation distance exceeds the critical distance (see Eq. 5.10 and Eq. 5.11) and the liquid



returns back to the particle. The effect of the tangential motion on the capillary force is not considered, i.e. the liquid bridge can move tangentially over the surface of particle and wall, and the liquid bridge force acts only on the normal direction. The viscous force is neglected because of the slow rotational speed of the shear cell and the small quantities of liquid in play.

- **Calculation of the shear stress from the simulation**

The stress distributions are assumed to be uniform across the horizontal shear plan in the annular shear cell (Nedderman, 1992). Thus, the shear stresses in the simulation and the experiment are calculated from the torque on the lid as a result of the resistance to the movement of the particles driven by the rotation of the shear cell. The relationship between the shear stress,  $\tau$ , and the torque,  $\Gamma$ , is expressed as:

$$\tau = \frac{\Gamma}{\frac{2}{3}\pi(r_e^3 - r_i^3)}, \quad \text{Eq. 5.13}$$

where  $r_i$  and  $r_e$  are, respectively, the internal and external radii of the lid. The torque on the lid in the simulation is calculated from the contact force particle–geometry.

From the simulation, the deviatoric stress and pressure can be calculated from the contact normal forces. It has been demonstrated that the tangential contact forces contribution to the deviatoric stress is very small (Thornton and Anthony, 1998; Thornton and Sun, 1993). The average stress tensors of a particles assembly of volume  $V_m$  are calculated from this expression (Cundall and Strack, 1979; Bagi, 1996):

$$\sigma_{ij} = \frac{1}{V_m} \sum_1^N F_{ij} \cdot k, \quad \text{Eq. 5.14}$$

where  $F_{ij}$  is the contact normal force,  $k$  is the branch vector connecting the centre of mass of the two particles in contact,  $V_m$  is the measurement cell volume and  $N$  is the number of particle in the cell. The principle stresses are then calculated from the nine stress tensors by determination of eigenvalues. From the principle stresses the deviatoric stress and the pressure are calculated, respectively, from the following equations (Hare *et al.*, 2015; Luding, 2008):

$$\sigma_H = \frac{\sigma_1 + \sigma_3 + \sigma_2}{3}, \quad \text{Eq. 5.15}$$

$$\tau_D = \frac{\sqrt{(\sigma_1 - \sigma_3)^2 + (\sigma_1 - \sigma_2)^2 + (\sigma_3 - \sigma_2)^2}}{\sqrt{6}}, \quad \text{Eq. 5.16}$$

where  $\sigma_H$  and  $\tau_D$  are the pressure and the deviatoric stress.  $\sigma_1$ ,  $\sigma_2$  and  $\sigma_3$  are respectively the major, the intermediate and the minor principle stresses.

### 5.3. Results and discussions

#### 5.3.1. Inter-particle friction measurements

Experimentally, many issues hinder the achievement of precise measurements of the friction coefficient such as relative humidity, surface roughness, particle size, particle morphology, adhesion and deformation etc. In the literature, the friction coefficient is often given as an approximate value and for a given measurement condition. The measured values of glass-glass sliding friction are rare. Moreover, the values found in the literature are inconsistent (Bharadwaj *et al.*, 2010), as you can see in Table 5.3.

Table 5.3: The values of glass-glass sliding friction from the literature.

Values of $\mu_p$	References
$\sim 0.1$	Foerster <i>et al.</i> , 1994
0.2-0.5	Stewart et al., 2001
$0.29 \pm 0.05$	Karmakar, 2014
0.4	Beare and Bowden, 1935
0.5	Majid and Walze, 2009
0.8	Brown and Richards, 1960

In this work, the friction of 2 mm glass beads as supplied, without any surface treatment, and others washed with acetone are measured. The friction test, as explained in chapter 3, was carried out for glass bead sliding upon a slide of glass (g-g: as supplied glass beads and wg-g: acetone washed glass beads) and a slide of steel (g-s). Fig. 5.3 shows the variation of the friction coefficient and the friction force as a function of the normal force. The friction coefficient decreases with the normal force increasing and then attains a constant value (from 3 N or 4 N). The friction coefficient of the acetone washed glass bead is lower compare to the non-treated one and the constant value is attained earlier at about 2 N of the normal force. From the friction force – normal force curves in Fig. 5.3-b, the apparent friction coefficient can be obtained by linear regression. The values of the apparent friction coefficients are given in Table 5.4. As expected, the apparent friction coefficient of the acetone washed glass beads is lower compared to the non-treated glass beads. This points out the effect of the surface treatment on the measurement of the friction at the particle scale. Indeed, the acetone used to clean up the glass beads helps to remove some of the impurities adhered to the surface and hence reduces the friction force. However, it may chemically modify the properties of the surface or physically coat the surface if it is not properly removed. This effect observed at the particle scale can be observed at a macroscopic scale; it can affect the shear resistance of the granular material in shear test for example.

Fig. 5.3-c and Fig. 5.3-d show the variations of the friction coefficient and the friction force for wet contact. The presence of liquid decreases the friction coefficient. The friction coefficient and the friction force response for glass–glass and glass–steel contacts have the same variation in the presence of liquid bridge. The extrapolation of data in Fig. 5.3-b and Fig. 5.3-d unveils the presence of an adhesive force. The intercept of the linear regression with the x-axis at zero friction force allows estimating this adhesive force. Table 5.4 shows that the adhesive force is increased in the wet case compare to the dry one.

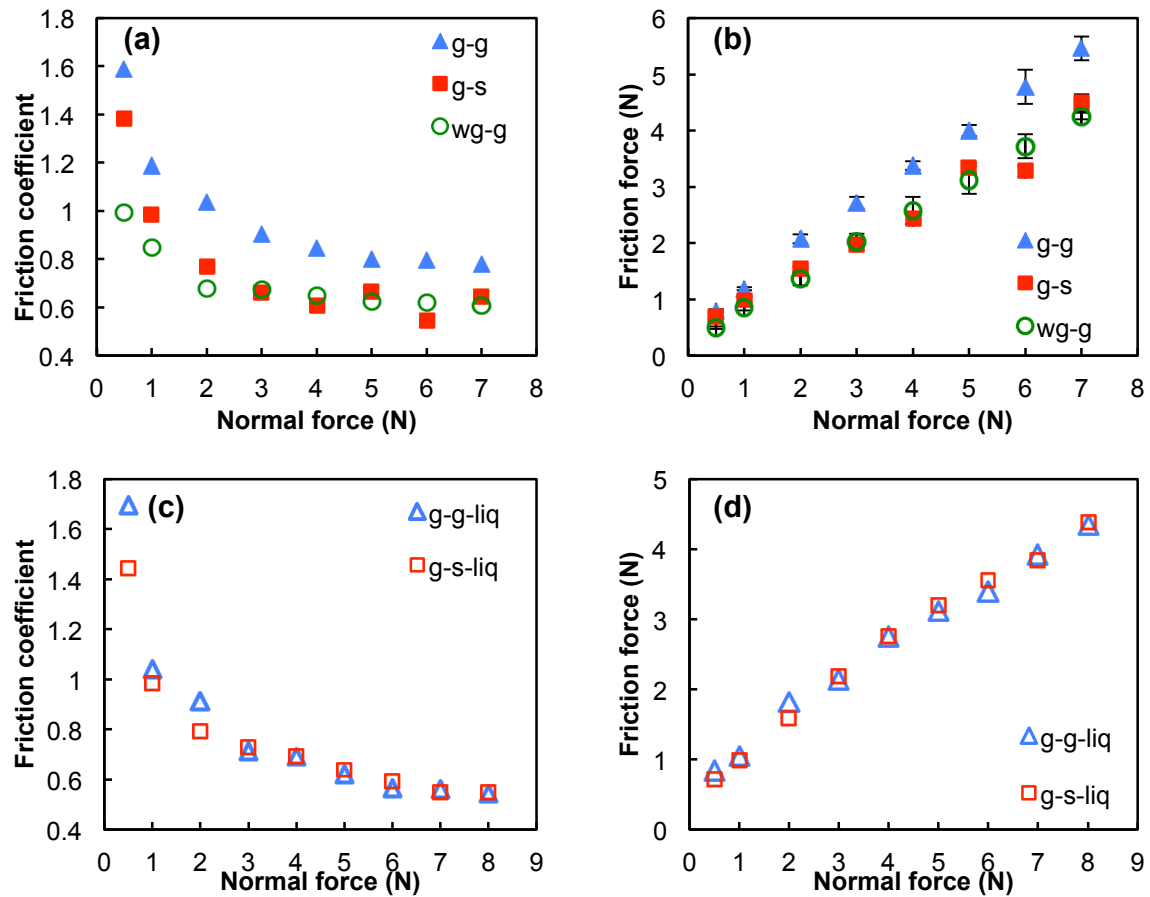


Fig. 5.3. Variation of the sliding friction coefficient (a) and (c) and the average friction force (b) and (d) of 2 mm glass bead sliding upon steel slide and glass slide, in the dry case (a) and (b) and wet case (c) and (d).

Table 5.4. The apparent friction coefficients and the adhesive forces from linear regression of the friction force–normal force data.

Fiction contact	Apparent friction	Adhesive force (N)	$R^2$
g-g (dry)	<i>0.71</i>	<i>0.75</i>	<i>0.998</i>
wg-g (dry)	<i>0.58</i>	<i>0.42</i>	<i>0.999</i>
g-s (dry)	<i>0.54</i>	<i>0.77</i>	<i>0.974</i>
g-g (wet)	<i>0.46</i>	<i>1.27</i>	<i>0.989</i>
g-s (wet)	<i>0.48</i>	<i>1.62</i>	<i>0.988</i>

### 5.3.2. Effect of microscopic properties on the macroscopic behaviour of the granular material in the simulation

We have first studied, the effect of the Young's modulus on the shear behaviour of the granular material. Then, after having chosen the adequate value of the Young's modulus, the effect of the particle sliding friction is studied. We focus only on the effect of the particle–particle friction, the particle–wall friction is not varied.

#### 5.3.2.1. Effect of the Young's modulus

We have shown in chapter 2, that the contact stiffness, which depends on the Young's modulus, affects the time-step; reducing the Young's modulus value leads to increase the time-step and hence to reduce the simulation time. The value of the Young's modulus is often reduced in the literature in order to speed up the computational time. In this section, we analyse the effect of the Young's modulus on the shear behaviour of the granular material for an eventual decrease of its value. Three values of the Young's modulus  $E1$ ,  $E2$  and  $E3$  were used for the simulation and they expressed different states of rigidity: hard, intermediate and soft respectively.  $E1$  is close to the value measured experimentally for the glass beads. Table 5.5 shows the effect of the Young's modulus on the time-step of the simulation. The latter is estimated as 19 % of the Rayleigh time in all cases, which is an appropriate percentage for granular material with high coordination numbers (4 and above) (DEM\_Solutions, 2015). We observe that the time-step increases by one order of magnitude for a decrease in the Young's modulus by two orders of magnitude and that has a big influence on the total time of the simulation, e.g. the total computation time for 3 s of simulation is about 320 h for  $E1$ , 40 h for  $E2$  and 7 h for  $E3$  in real time. In order to gain in the computational time, the value of the Young's modulus is often reduced, this can influence the result obtained from the simulation though. Next, the effect of decreasing the Young's modulus on the shear behaviour of the granular material will be discussed. We focus on the impact on the stress ratio, the voidage fraction, the coordination number or the number of liquid bridge in the wet case and the average velocity of the particle. The results from the simulation are also compared with the experimental measurements.

Table 5.5. Effect of the Young's modulus input values on the time-step of the simulation.

Variables	Young's modulus (GPa)	Time-step (s)
$E1$	26	$2.3e-07$
$E2$	0.26	$2.3e-06$
$E3$	0.0026	$2.4e-05$

#### a. Effect of Young's modulus on the stress ratio

Fig. 5.4 shows the variation of the stress ratio (shear stress / normal stress) as a function of the displacement of the shear cell during shearing. This displacement is expressed relative to the diameter of the particle by  $(\Phi R_e/d)$ , where  $\Phi$  is the rotational angle of the shear cell and  $R_e$  is its external radius. This expression gives a concrete representation of the shearing progress. The stress ratio data given in this figure are measured for a normal stress of about 12 kPa in experiment and simulation. The applied normal stress to the glass beads bed is assumed to be constant during shearing in the experiment since the granular bed is subjected to a constant load. In the simulation, the normal stress is controlled by servo-control of the position of the lid over shearing time. However, the variation of the normal force during shearing can be different from one simulation to another depending on the parameters used, in particular the Young's modulus. Therefore, the stress ratio is relied to get over the variation of the shear stress response due to the normal stress variation and to better compare the results.

Fig. 5.4-a shows the variation of the stress ratio of dry glass beads. The observed curves shows an increase of the fluctuations of the signal with the Young's modulus increasing. The experimental stress ratio also shows a fluctuation, which is caused by the rearrangement of glass beads under shearing and by the stick-slip motion accompanied. The average stress ratio in steady-state shearing from the simulation is between 0.34 – 0.35 with a large standard deviation for  $E1$ . However, the average stress ratio obtained from the experimental data is about 0.42. The simulated stress ratio is underestimated compare to the experimental one by about 17% – 19%. The observation of the stress ratio variations at the start of shearing (from 0.04 rad) shows different profiles depending on the Young's modulus values. This gives an idea about the deformations of the granular bed under shearing. We observe that curves of  $E1$  and  $E2$  show the same profile, which is different to the profile of  $E3$ . The latter attains the yield stress tardily, which means that the deformation of the granular material is softer.

Fig. 5.4-b shows the variation of the stress ratio of wet glass beads ( $V_R = 4.5\%$ ). The increase of the fluctuations of the signal with the Young's modulus increasing is also observed for the wet case. The experimental signal shows a large stick-slip oscillations compared to the dry case. The average values of the stress ratio at steady-state from the simulation underestimate the experimental one. However, the profile of the signal at the start of shearing for  $E1$  and  $E2$

is closer to the experimental one. On the contrary, the profile of  $E3$  is different, as it was observed in the dry case.

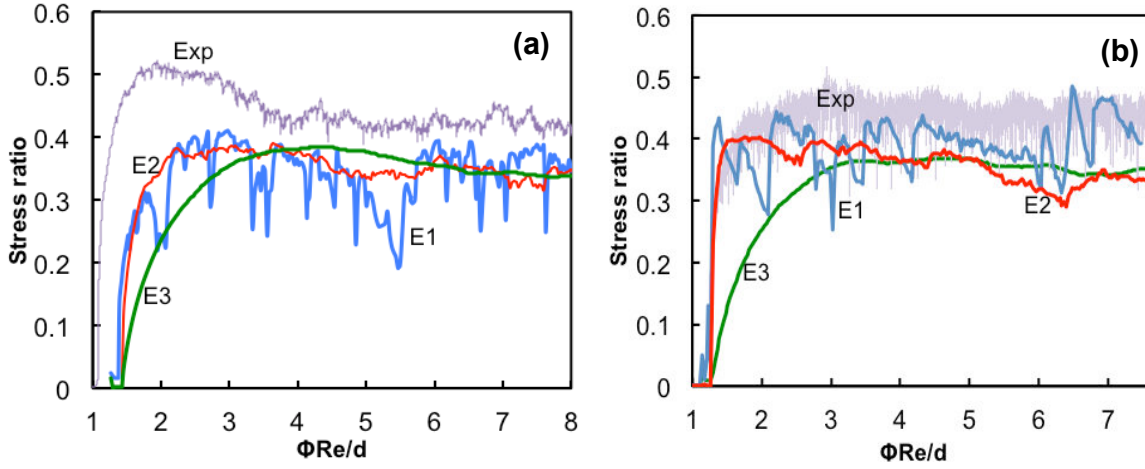


Fig. 5.4. Variation of the stress ratio (shear stress / normal stress) during shearing for different Young's modulus values (E1, E2, E3) from the simulation and compared to the experimental data (Exp). (a) For dry glass beads, (b) for wet glass beads ( $V_R = 4.5\%$ ).

#### b. Effect of Young's modulus on the voidage fraction, the coordination number (the number of liquid bridge) and the velocity of particles

In this section, we analyse the variation of some properties of the granular material during shearing under the variation of the Young's modulus values. We focus on the voidage fraction, the coordination number and the velocity of particles for dry and wet glass beads. In the wet case, the number of liquid bridge is considered instead of the coordination number.

Fig. 5.5-a shows a decrease of the value of the voidage fraction by decreasing of the Young's modulus to  $E3$ . However, we observe close values of the voidage fraction for  $E1$  and  $E2$ . Moreover, we observe that the voidage fraction attains a constant value at the steady-state shearing, as it is expected. The same observations are made for the wet glass beads. However, we can see an increase of the voidage fraction values for the wet case compared to the dry one. The last point will be discussed later. The disruption observed for data of  $E1$  is caused by the instability of the position of the lid at high Young's modulus of particles.

Fig. 5.5-b shows an increase of the coordination number for a decrease in the Young's modulus values. The average number of coordination is found to be small, i.e. the calculated number for  $E1$  is about 4. The latter is the minimum number required to ensure a stable system (Zamponi, 2008). In deed, the coordination number from the simulation is calculated as the number of contacts divided by half of the number of particles. However, particles with no contact at all or with one contact do exist in the simulation (Thornton and Antony, 1998), which leads to reduce the calculated number of coordination. For the wet case, the number of liquid bridges per particle is higher than the number of the coordination number. Indeed, some liquid bridges

are formed even for no physical contact between particles, provided that the separation distance is smaller than a critical distance as given by Lian *et al.*, (1993). The number of liquid bridges decreases by increasing the Young's modulus from  $E3$  to  $E2$ , following the number of coordination. The disruption of the data for  $E1$  makes the variation of the number of liquid bridge not clear.

In the literature, Antony and Kruyt (2009) have numerically studied the effect of the Young's modulus on the voidage fraction and the coordination number of dry granular material sheared in an axisymmetric compression test. Two polydisperse spheres, with an average size of 100  $\mu\text{m}$ , were used in this purpose: soft ( $E = 0.07 \text{ GPa}$ ) and hard ( $E = 70 \text{ GPa}$ ). Similar results were observed; an increase of the coordination number and a decrease of the voidage fraction for a decrease in the Young's modulus.

Fig. 5.5-c displays the velocity profile of particles for different positions in the bed height denoted by  $Z/H$ , where  $Z$  is the vertical coordinate and  $H$  is the total height of the bed. The normalized velocity is given by the average velocity of particles, during steady-state, for a given position divided by the rotational speed of the shear cell. The velocity of particles decreases from the cell bottom ( $Z/H = 0$ ) to the top ( $Z/H = 1$ ) since the lid (on the top) is immobile while the cell is rotating. The saturation of the velocity near to the top and the bottom results from particles gripped by the bars in the lid and the bottom of the cell. The saturation is more significant in the lower part of the cell; it is occupying about 40% of the total height of the granular bed. However, the saturation observed in the upper part is dependent on the Young's modulus values, i.e., it increases with the Young's modulus increasing. This means that the sheared layer of the granular bed decreases by decreasing the Young's modulus. For wet glass beads, we observe that the effect of the Young's modulus on the particles velocity is reduced; almost the same variation is observed for  $E1$  and  $E2$  and slightly lower velocity for  $E3$ . It can be observed also that the additional cohesive forces decrease the velocity of particles, especially for  $E1$  and  $E2$ . Moreover, the saturation of the velocity at the upper part is not observed. This can be explained by the fact that the existence of cohesive forces between particles contributes on driving the movement of particles on the top.

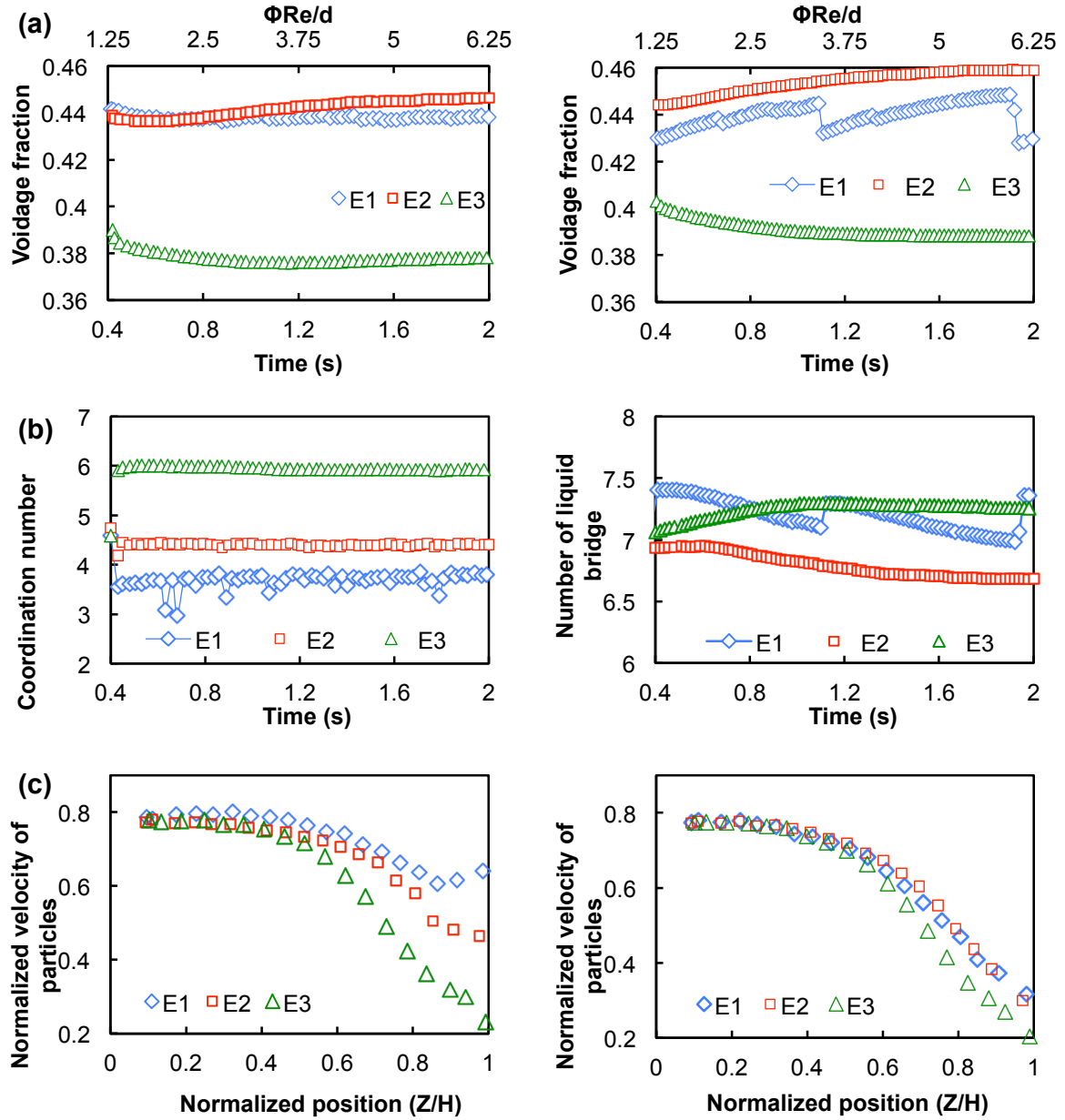


Fig. 5.5: Left, variation of the voidage fraction, the coordination number and the velocity of particles during shearing for dry glass beads and for different Young's modulus values. Right, variation of the voidage fraction, the number of liquid bridge and the velocity of particles for wet glass beads and for different Young's modulus values. All data are given for an applied normal stress of 12 kPa.

### c. Conclusions

The analysis of the Young's modulus effect on dry and wet granular material properties has been studied in this section. We have shown that the Young's modulus does not affect significantly the average stress ratio values at steady-state shearing. However, the stress ratio response for the highest Young's modulus  $E1$  shows a remarkable instability of the signal, which is caused in a part by the instability of the compressive force applied by the lid to the



granular material. In fact, it was hard to maintain a constant normal stress by servo-control of the lid displacement during shearing in this case. The reason is that the Young's modulus of particle is in the same order of magnitude as the one of geometry. The latter was a little increased in this circumstance compared to the other simulations. We have also shown that the Young's modulus affects the velocity of particles in the shear cell. The average velocity and the shear zone decrease with a decrease in the Young's modulus value. For the wet case, the effect of the Young's modulus on the velocity of particle is reduced and the saturation of the velocity in the top of the granular bed disappeared. Moreover, the decrease of the Young's modulus value leads to an increase in the number of coordination and to a decrease in the voidage fraction.

The discussed influence of the Young's modulus on the granular material properties is on one hand, an important aspect to take into consideration before running a simulation. On the other hand the computation time is largely affected by the Young's modulus value and should be also considered. For this study the Young's modulus  $E2$  is the appropriate value to be considered and it will be used in the following simulations.

### 5.3.2.2. Effect of particle sliding friction

In this section, the effect of the particle sliding friction ( $\mu_p$ ) on the stress ratio, the coordination number (the number of liquid bridge for the wet case), the voidage fraction and the velocity of particles are studied. For this purpose, different values of  $\mu_p$  were used for the simulations: 0.1, 0.25, 0.35, 0.5 and 0.7.

#### a. Effect of particle sliding friction on the stress ratio

The shear stress from the simulation as well as in the experiment is calculated from the torque on the lid as given by Eq. 5.13. Fig. 5.6 shows the stress ratio variation during shearing for different particle sliding friction values. The displayed data is obtained for a normal stress of about 12 kPa for the simulation and the experiment. We observe that the particle sliding friction affects the value of the stress ratio for dry case (figure on the left) and wet case (figure on the right). We observe also that the simulated values underestimate the experimental one. As mentioned above, we are only focusing on the stress ratio at steady-state.

The variation of the stress ratio as a function of the particle sliding friction is given in Fig. 5.6-c. We observe an increase of the stress ratio with the particle sliding friction increasing between 0.1 and 0.5. However, the increase of the particle sliding friction above 0.5 leads to a saturation of the stress ratio variation. The saturation is attained earlier in the wet case at about  $\mu_p = 0.35$ .

The comparison of the stress ratio variation with the particle sliding friction for dry and wet cases shows higher values of the stress ratio of wet glass beads at low sliding friction ( $\mu_p \leq 0.5$ ), however it becomes slightly lower or equal to the dry one at high sliding friction ( $\mu_p > 0.5$ ). This indicates that the effect of liquid is affected by the value of the particle sliding friction.

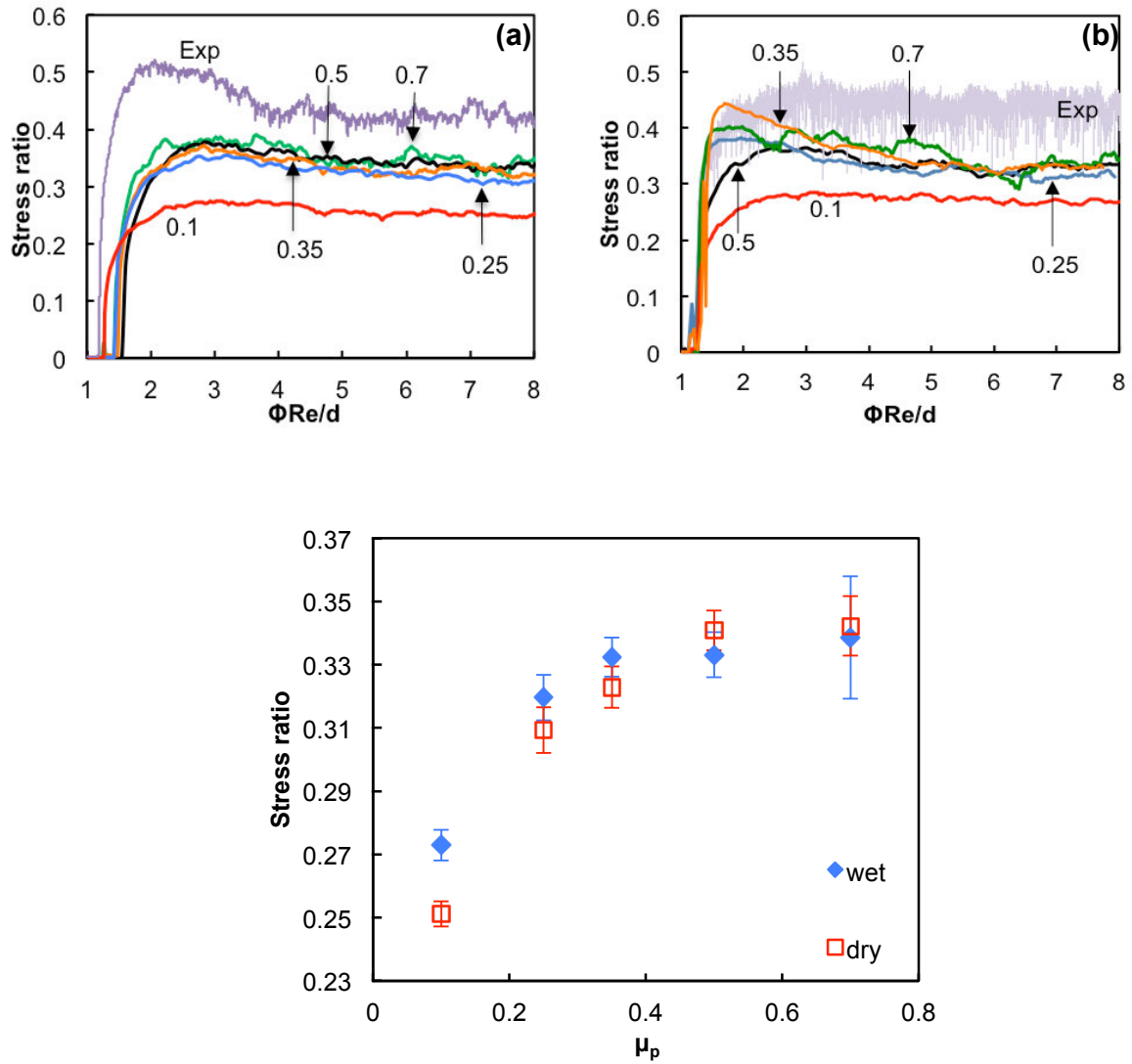


Fig. 5.6: Stress ratio variation during shearing for different particle sliding friction values, (a) for dry and (b) for wet. (c) Average stress ratio variation with the particle sliding friction for dry and wet glass beads.

#### b. Effect of particle sliding friction on the voidage fraction, the coordination number (number of liquid bridges) and the velocity of particles

Fig. 5.7-a shows the variation of the voidage fraction during shearing at about 12 kPa of normal stress. Regardless of the effect of the particle sliding friction, the voidage fraction decreases when the lid starts to move down to reach the desired normal stress, for times between 0.4 s – 0.46 s for the dry case data and 0.36 s – 0.42 s for the wet case. The compacted granular material begins then to dilate as the shear cell starts to rotate; the voidage increases and reaches a constant value at steady-state. Now, regarding the effect of the particle sliding friction, we observe that the voidage fraction increases with the sliding friction increasing for dry and wet cases.

Fig. 5.7-b shows that the coordination number takes a constant value during shearing, which means that the average number of contact is preserved under the motion of particles. This is not the case of the liquid bridges number, which seems to vary a little at the start of shearing and then to reach a constant value at the steady-state. As expected a decrease of both the coordination number and the number of liquid bridges is observed for a decrease in the particle sliding friction coefficient. Thornton and Anthony (1998) have shown that the coordination number starts to saturate at high values of particle sliding friction beyond 0.6 or 0.7. We expect also a saturation of the number of liquid bridges around the same values of the sliding friction. Indeed, the effect of the sliding friction on the number of liquid bridges starts to be small between 0.5 and 0.7. Thornton and Anthony (1998) have demonstrated that increasing the friction at the contacts leads to an increase in the stability of the system and hence a smaller number of contacts is needed to establish a stable configuration. This may explain the lower number of the coordination number obtained for  $\mu_p = 0.7$  (see Fig. 5.7-b).

Fig. 5.7-c shows a decrease of the average velocity of particles for an increase in the particle sliding friction. For the dry case, the saturation zones of the velocity, near to the top and the bottom of the shear cell, increases with an increase in the particle sliding friction. This means that the shearing zone decreases with the particle sliding increasing. For the wet case, the effect of the particle sliding friction on the velocity is observed to be reduced compared to the dry case.

It has been observed by Hsiau and Shieh (2000) that the velocity of particles is affected by the voidage fraction of the granular material. Velocities were measured experimentally in a transparent shear cell using CCD camera to record the motion of several tracer particles. They demonstrated that even for a small decrease in the voidage fraction, a decrease of the velocity of particle can be observed especially at the upper part of the granular bed. From the simulation, we found that both voidage fraction and velocity of particles decrease with the particle sliding friction decreasing. Therefore, we conclude that the velocity of particles is affected by the voidage fraction variation.

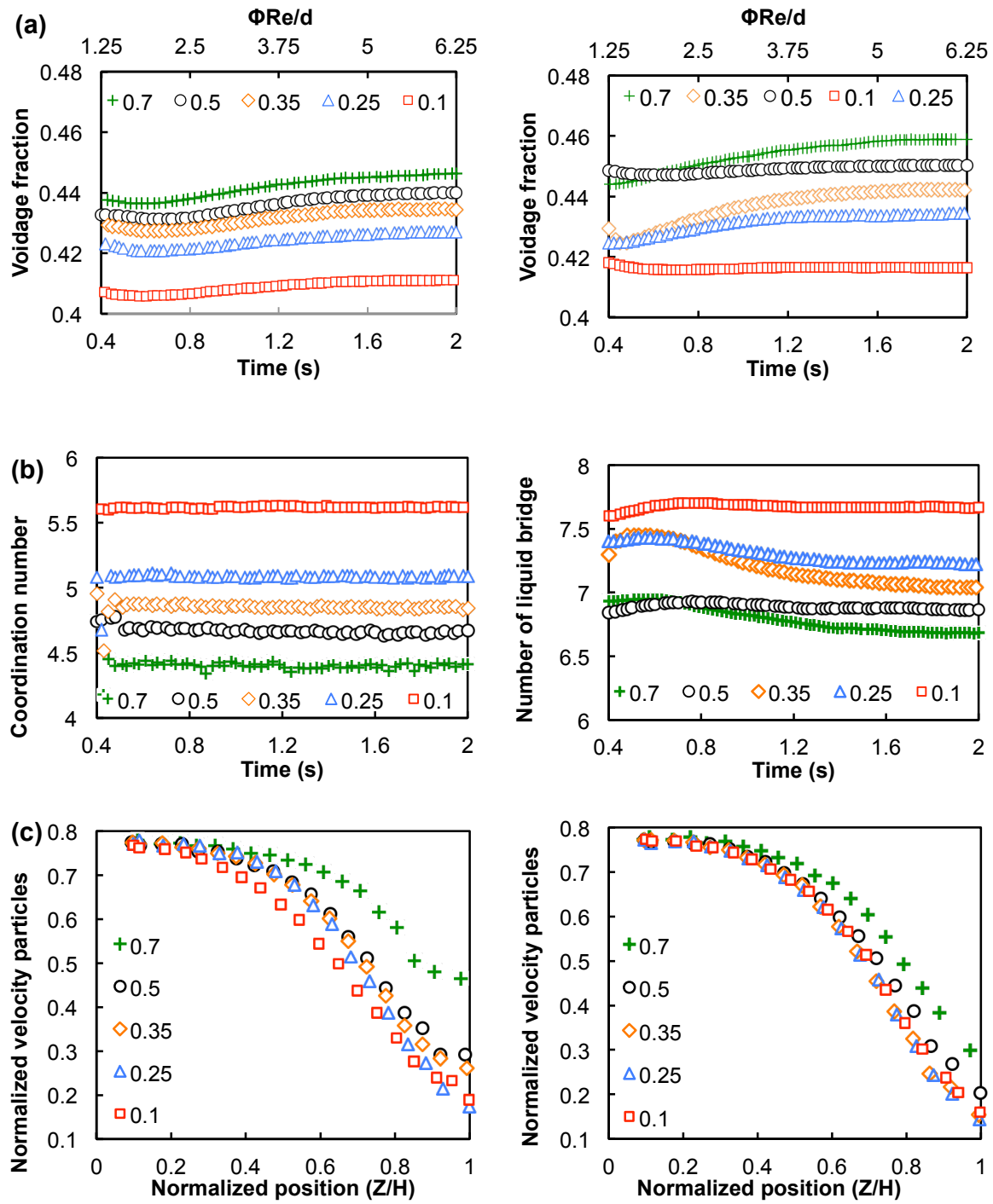


Fig. 5.7: Left, variation of the voidage fraction, the coordination number and the velocity of particles during shearing for dry glass beads and for different particle sliding friction values. Right, variation of the voidage fraction, the number of liquid bridges and the average velocity of particles for wet glass beads and for different particle sliding friction values.

### c. Conclusions

In this section, we have shown that the particle sliding friction affects many of the granular material properties. First, the stress ratio increases with the particle sliding friction increasing up to about 0.5 and saturates above that value. We observed higher values of the stress ratio for the wet case compared to the dry case for  $\mu_p < 0.5$ , however both values get close beyond 0.5. Secondly, we observed an increase of the voidage fraction and a decrease of the number of coordination by increasing the particle sliding friction. The number of liquid bridge for the wet case follows the variation of the coordination number in the dry case. Finally, the increase of the particle sliding friction increases the average velocity of particles but decreases the shearing zone. The presence of liquid reduces the effect of the friction on the velocity of particles and the shearing zone variation.

In the following, a constant value of the particle sliding friction will be used for the dry and wet cases in order to focus on the effect of liquid. The value of 0.5 will be considered since it is in the range of the measured value for the dry and wet cases.

#### 5.3.3. Effect of liquid on the shear behaviour of wet granular material

##### 5.3.3.1. Variation of the liquid bridge force with the separation distance

Fig. 5.8 shows the liquid bridge force variation with the separation distance between sphere-sphere. The data gives the liquid bridge forces between spheres at a given time during shearing and for different volume ratios ( $V_R$ ). The data of the liquid bridges formed between sphere-wall are not shown here but they have the same variation aspect as the sphere-sphere in term of the effect of the separation distance and the volume ratio. The liquid as described by the model of Mikami *et al.* increases exponentially for a decrease in the separation distance (see Eq. 5.2). The separation distance as described by Lian *et al.* model increases for an increase in the volume of liquid (see Eq. 5.10 and Eq. 5.11). Therefore more liquid bridges are formed for large separation distances when the quantity of liquid increases. Fig. 5.8 shows that the liquid bridge force not only dependent on the separation distance but also on the volume of liquid, i.e. for the same separation distance, forces increase with the volume of liquid increasing. At small separation distance, close to zero, the effect of the separation distances prevails the effect of the volume of liquid; the liquid bridge forces data for different liquid fractions are superimposed. An increase of the liquid bridge force is observed for small negative separation distance, i.e. when particle are overlapped, although the separation distances was set to zero to avoid super large force.

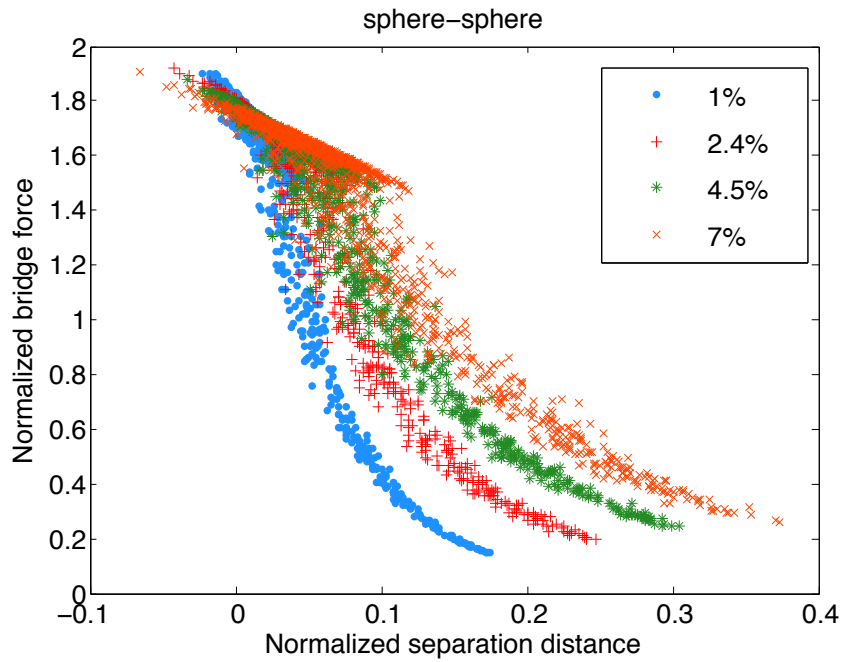


Fig. 5.8. Variation of the normalized liquid bridge force ( $F_c/\pi R\gamma$ ) as a function of the normalized separation distance ( $2h/R$ ) for sphere-sphere contact.

### 5.3.3.2. Effect of liquid on the shear stress

Fig. 5.9 shows the shear stress response from the experimental shear test for dry and wet glass beads ( $V_R = 1\%$ ). A small increase of the average shear stress of wet glass beads is observed for low normal stress (about 1 kPa) in Fig. 5.9-a. The shear stress signal shows an oscillatory stick-slip motion with almost the same amplitude for both cases (dry and wet). However, a noticeable increase of the amplitude of the stick-slip motion is clearly observed for wet glass beads at high normal stress (about 12 kPa) in Fig. 5.9-b. By increasing the normal stress, the behaviour of wet glass beads under shearing is different compared to the dry one. Indeed, the presence of liquid provides a loose configuration of the granular material and hence promotes the mobility of particles under shearing. This can be observed by looking at the yield stress (the maximum shear stress at the peak), which is lower in the wet case compared to the dry one. It is not obvious to compare the values of the shear stress (for dry and wet) because of the large oscillation of the signal. An average value of the shear stress of all the data at steady-state is considered.

Fig. 5.10-a shows the stress ratio calculated as the average steady-state shear stress divided by the normal stress and plotted as a function of the normal stress. The effect of liquid on the stress ratio is more significant at low normal stresses; an increase of the stress ratio with the normal stress decreasing can be observed at low normal stress ( $\sigma < 5$  kPa). However, it becomes constant above 5 kPa. The effect of the liquid content increasing is not clearly observed here. By contrast, it was observed, for smaller glass beads (70-110  $\mu\text{m}$ ); the stress

ratio increased for an increase in the liquid fraction. Surprisingly here, a reverse effect is obtained for 7% of the liquid fraction; the stress ratio is decreased at low normal stress but it converges to the same constant value above 5 kPa.

From the simulation, it is observed in Fig. 5.10-b that the stress ratio decreases with the normal stress and converges to a constant value beyond 5 kPa. The liquid bridge forces and the normal forces are evaluated from the simulation and a force ratio is calculated. This force ratio is the capillary force divided by the normal contact force (the forces at sphere-sphere and sphere-wall contact) and is plotted as a function of the normal stress in Fig. 5.11. We observe a decrease of this force ratio with the normal stress increasing and it tends toward a constant value at high stress above 5 kPa. This variation is comparable to the variation of the stress ratio observed in Fig. 5.10. We deduce that the liquid bridge force is not directly affected by the normal stress applied to the granular material, i.e. the normal stress does not affect the separation distance too much. However, the decrease of the normal force contact by decreasing the normal stress makes the liquid bridge forces more significant and hence they affect more the shear stress response. However, the effect of the liquid volume increasing on the capillary force is not significant; curves observed in Fig. 5.11 are overlapped.

The model used to calculate the liquid bridge force in our work is limited to small liquid fractions, which forms liquid bridges at the contact points, known as the pendular state. The increase of the volume of liquid leads to broaden the liquid bridges and hence to make them touch each other. In this case, a new capillary state is defined, known as the funicular state. In order to check out the state of saturation for the different liquid fractions used in this work, a microscopic observation was carried out. A few wet glass beads were brought into contact and liquid bridges were observed. Fig. 5.12 shows liquid bridges with small volume of liquid for 1% of the volume ratio. These liquid bridges are broadening when the quantity of liquid increases to 2.4% and 4.5%, most of them are not in contact with their neighbours though. However, at 7% many liquid bridges have been connected with their neighbours as seen in Fig. 5.12 on the right hand side. The change of saturation state at 7% means that the numerical model should not be used for such high liquid fraction. This can explain the difference between experimental and simulated stress ratio data obtained for 7% of liquid fraction.

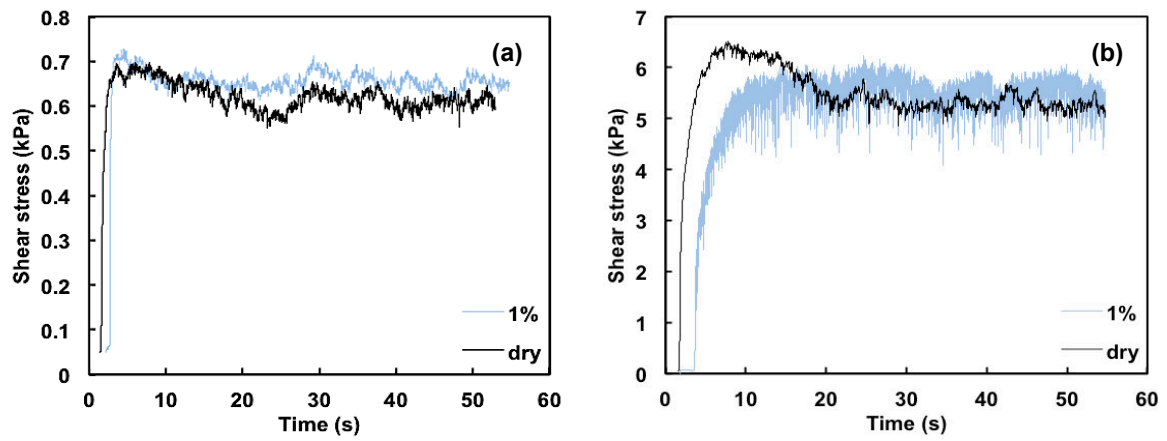


Fig. 5.9. Shear stress response during shearing for dry and wet glass beads (1%). (a) at low normal stress (1 kPa) and (b) at high normal stress (12 kPa).

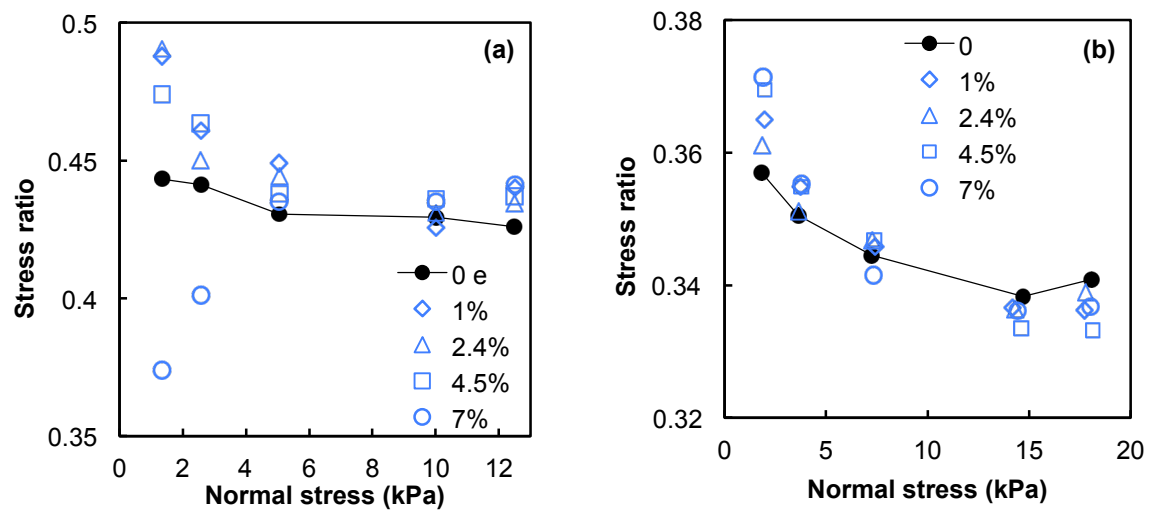


Fig. 5.10. Stress ratio variation with the normal stress for different liquid fractions from experiment (a) and simulation (b).



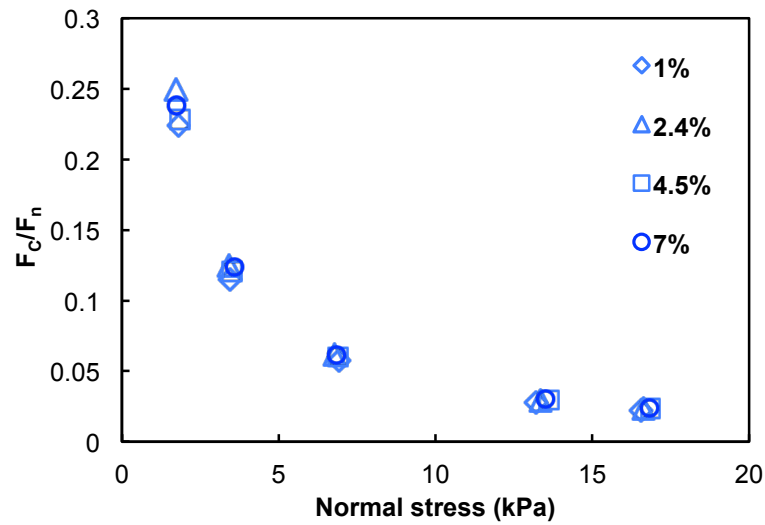


Fig. 5.11. Variation of the force ratio (capillary force divided by the normal force) with the normal stress for different liquid fractions ( $V_R(\%)$ : 1, 2.4, 4.5 and 7).

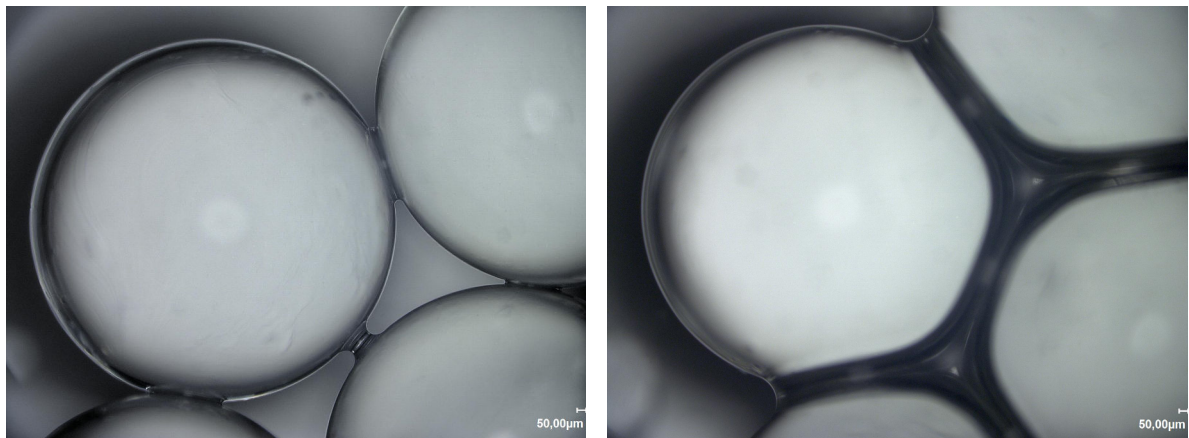


Fig. 5.12. Optical microscope observation of liquid bridges between glass beads. Low liquid content ( $V_R = 1\%$ ) on the left and large liquid content ( $V_R = 7\%$ ) on the right.

### 5.3.3.3. Effect of liquid on the voidage fraction

The voidage fraction variation from experiment and simulation are calculated as the volume of voids divided by the total volume of the granular bed in the shear cell. Fig. 5.13 shows the same variation of the voidage fraction with the liquid fraction from the experimental and the simulated data. Initially, the voidage fraction increases when a small quantity of liquid is added to the granular material because of the formation of liquid bridges. Then, the increase of the quantity of liquid leads to the formation of a few more liquid bridges but mostly to expand the volume of the existed liquid bridges and hence to decrease the voidage fraction. We have

shown previously (in chapter 4) that the increase in the voidage fraction as a result of the addition of liquid depends on the particle size. We observed larger increase of the voidage fraction for 12-40  $\mu\text{m}$  glass beads than for 70-110  $\mu\text{m}$ . Yet, the increase of the voidage fraction for 2 mm glass beads is smaller than that observed for 70-110  $\mu\text{m}$ .

As it is observed in Fig. 5.13, the simulated data underestimates the experimental one for the wet case while the values are very close in the dry case. This may be explained by the fact that the liquid is evenly distributed in the simulation but may be not in the experiment; large gaps may exist in the zone where no liquid bridges are formed in the experiment.

It can be observed an agreement between the simulation and the experiment that the largest voidage fraction is reached at 1% of the volume ratio. This assumes that the majority of liquid bridges are formed at this level. Investigating the variation of liquid bridges in the next subsection will check this out.

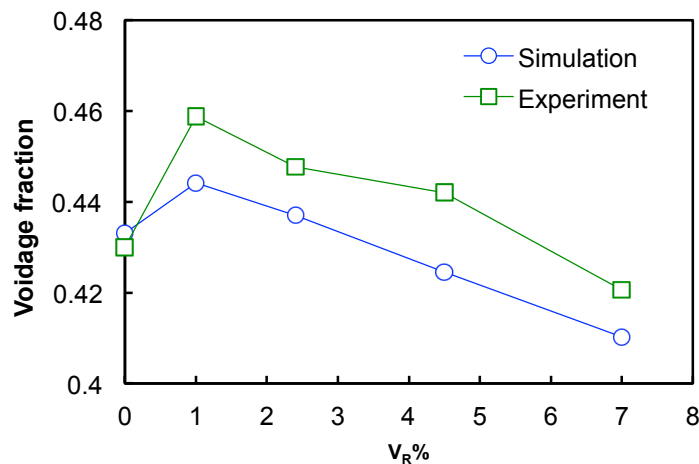


Fig. 5.13: Variation of the voidage fraction with the liquid fraction from the simulation and the experiment.

#### 5.3.3.4. Effect of liquid and normal stress on the number of liquid bridges

Fig. 5.14 shows the variation of the average number of liquid bridges per particle during shearing. The plotted data are given for a high-applied normal stress around 12 kPa. At first, the number of liquid bridges increases when the shear cell starts to rotate (about time = 0.4 s). We observed that the voidage fraction slightly decreased for the same period of time and hence promoted the formation of liquid bridges. Then the voidage fraction increased and, therefore, the number of liquid bridges decreases. It is observed that the decrease in the number of liquid bridges during shearing depends on the liquid content, i.e. it is more pronounced when the liquid content is smaller. This behaviour is not explained by the variation of the voidage fraction since it is almost the same for the different liquid fractions. However, it is explained by the fact that at small liquid fractions, the number of broken liquid bridges is larger than the

number of formed liquid bridges. In fact, the breakage of liquid bridges, initially formed before shearing, depends on the separation distance between sphere-sphere and sphere-wall and the critical separation distance, causes the breakdown of the liquid bridge, depending on the volume of liquid (see Eq. 5.10 and Eq. 5.11); it is smaller for lower liquid contents and consequently the liquid bridges are more easily broken under shearing. Finally, the number of liquid bridges reaches a constant value at steady-state shearing.

Regarding the effect of liquid fractions on the number of liquid bridges, we observed that the average number per particle does not significantly increase for an increase in the quantity of liquid; about 6 liquid bridges per particle are formed at 1% and rises to around 7 at 7% of the liquid fraction. This corroborates the assumption made previously that most of the liquid bridges are formed at 1% of liquid fraction and explains the variation of the voidage fraction in the previous section.

The variation of the number of liquid bridge with the applied normal stress is given by

$$\Delta N\% = \frac{N - N_0}{N_0} * 100, \quad \text{Eq. 5.17}$$

where  $N_0$  is the number of liquid bridges formed for an applied normal stress equivalent to the weight of the lid and  $N$  is the number for a given normal load applied over the lid. Fig. 5.15 shows that the number of liquid bridges increases with the normal stress up to about 5 - 6 kPa and then saturates. This variation is observed for the different liquid fractions. The saturation of the number of liquid bridges leads to a saturation on the capillary forces and consequently affects the shear stress response.

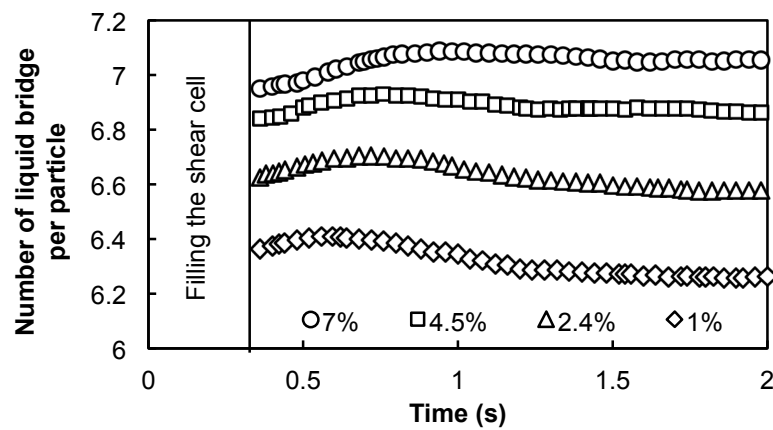


Fig. 5.14. Variation of the average number of liquid bridges per particle during shearing for different liquid fractions.

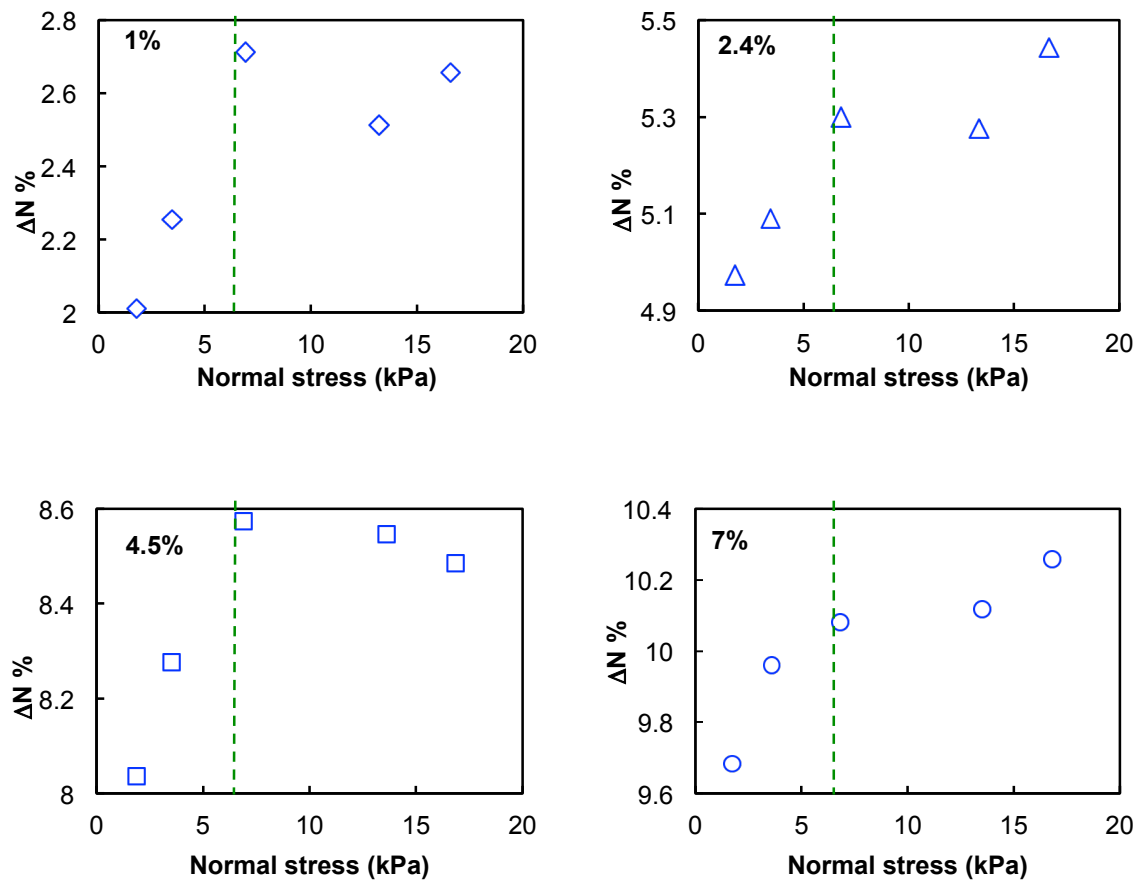


Fig. 5.15. Variation of the number of liquid bridges with the normal stress for different liquid fractions.

## 5.4. Conclusions

The discrete element method was used in the continuation of our experimental study (chapter 4) in order to gain an understanding of some microscopic aspects of the dry and wet shear behaviour of granular materials. The numerical simulations were carried out in parallel with experimental testing in order to compare the results and to understand the difference if any. We have tried to introduce the same experimental parameters (size of particles, geometry dimensions of the shear cell, particle properties, etc.) for the simulation to the extend possible. It was actually necessary to study the effect of the variation of some parameters on the results. We have shown that the young's modulus can be decreased in order to speed up the simulation but not too much to not affect the results. We have shown also that the variation of the particle sliding friction affects the results in the dry and wet cases. We choose to use the same value of the sliding friction for the dry and wet case in order to evaluate the effect of liquid independently on that value.

In the investigation of the effect of liquid in the simulation we have focused on the effect of liquid fraction and the normal stress. The effect of the liquid fraction was not significant for

either experimental or numerical results. In fact, we have used large sized glass beads to speed up the computations, however this reduces the effect of the capillary forces in the presence of significant gravitational forces. Regarding the effect of the normal stress, we have shown that the capillary forces are relatively significant at low normal stresses since low normal contact forces are implied. However, this effect is reduced at high normal stresses since the contact forces are more significant. The number of liquid bridges increases with the normal stress increasing up to around 5 kPa and then saturates above that value.

## **Conclusions (en Français)**

La méthode des éléments discrets a été utilisée à la suite de notre étude expérimentale (chapitre 4) afin de mieux comprendre certains aspects microscopiques du comportement au cisaillement de milieux granulaires sec et humide. Les simulations numériques ont été effectuées en parallèle avec des essais expérimentaux afin de comparer les résultats. Nous avons essayé d'introduire les mêmes paramètres expérimentaux pour la simulation dans la mesure du possible (taille des particules, dimensions géométriques de la cellule de cisaillement, propriétés des particules, etc.). Il a été nécessaire d'étudier l'effet de la variation de certains paramètres sur les résultats. Nous avons montré que le module du Young peut être diminué afin d'accélérer la simulation mais pas trop pour ne pas affecter les résultats. Nous avons également montré que la variation du coefficient de frottement des particules affecte les résultats dans les cas secs et humides. Nous choisissons d'utiliser la même valeur de frottement de glissement pour le cas sec et humide afin d'évaluer l'effet du liquide indépendamment de cette valeur.

Dans l'investigation de l'effet du liquide dans la simulation nous nous sommes concentrés sur l'effet de la fraction de liquide et de la contrainte normale. L'effet de la fraction de liquide n'a pas été significatif sur les résultats expérimentaux ou numériques. En fait, nous avons utilisé des billes de verre de grande taille pour réduire le temps de calcul numérique, mais cela réduit l'effet des forces capillaires en présence de forces gravitationnelles significatives. En ce qui concerne l'effet de la contrainte normale, nous avons montré que les forces capillaires sont relativement importantes à des contraintes normales faibles, étant donné que des forces de contact normales moins importantes sont impliquées. Cependant, cet effet est réduit pour les contraintes normales élevées puisque les forces de contact sont plus importantes. Le nombre de ponts liquides augmente avec la contrainte normale jusqu'à environ 5 kPa puis devient constant au delà de cette valeur.

## References

- Antony, S.J. and Kruyt, N.P., 2009. Role of interparticle friction and particle-scale elasticity in the shear strength mechanism of three-dimensional granular media. *Phys. Rev. E*, 79, 031308(1)-031308(9).
- Bagi, K., 1996. Stress and strain in granular assemblies. *Mech. Mater.*, 22, 165-177.
- Baharadwaj, R., Ketterhagen, W.R. and Hancock, B.C., 2010. Discrete element simulation study of a Freeman powder rheometer. *Chem. Eng. Sci.*, 65, 5747-5756.
- Beare, W.G. and Bowden, F.P., 1935. Physical properties of surfaces. I. Kinetic friction. *Philos. Trans. R. Soc. A*, 234, 329-354.
- Brown, R.L. and Richards, J.C., 1960. Profile of flow of granules through apertures. *Trans. Inst. Chem. Eng.* 38, 243-256.
- Cundall, P.A. and Strack, O.D.L., 1979. A discrete numerical model for granular assemblies. *Geotechnique*, 29, 47-65.
- DEM\_Solutions, 2015. EDEM 2.7 User Guide. DEM Solutions Limited, Edinburgh, 1 – 133.
- Foerster, S.F., Louge, M.Y., Chang, H. and Allia, K., 1994. Measurement of the collision properties of small spheres. *Phys. Fluids*, 6, 1108-1115.
- Hare, C., Zafar, U., Ghadiri, M., Freeman, T., Clayton, J. and Murtagh, M.J., 2015. Analysis of the dynamics of the FT4 powder rheometer. *Powder Technol.*, 285, 123-127.
- Hsiau, S., and Shieh, Y., 2000. Effect of solid fraction on fluctuations and self-diffusion of sheared granular flows. *Chem. Eng. Sci.*, 55, 1969-1979.
- Karmakar, S., 2014. Experimental investigations of mechanical properties of wet granular materials. PhD Thesis, University of Saarlandes, Saarbrücken.
- Lian, G., Thornton, C. and Adams, M.J., 1993. A theoretical study of the liquid bridge forces between two rigid spherical bodies. *J. Colloid Interface. Sci.*, 161, 138-147.
- Louati, H., Oulahna, D. and de Ryck, A., 2015. Apparent friction and cohesion of a partially wet granular material in steady-state shear. *Powder Technol.*, 278, 65-71.
- Luding, S., 2008. Constitutive relations for the shear band evolution in granular matter under large strain. *Particuology*, 6, 501-505.
- Majid, M. and Walzel, P., 2009. Convection and segregation in vertically vibrated granular beds. *Powder Technol.*, 192, 311-317.
- Mikami, T., Kamiya, H. and Horio, M., 1998. Numerical simulation of cohesive powder behaviour in a fluidized bed. *Chem. Eng. Sci.*, 53, 1927-1940.
- Nase, S.T., Vargas, W.L., Abatan, A.A. and McCarthy, J.J., 2001. Discrete characterization tools for cohesive granular material. *Powder Technol.*, 116, 214-223.
- Nedderman, R.M., 1992. Statics and kinematics of granular materials. Cambridge University Press, UK, 1992.
- Ning, Z. and Ghadiri, M., 2006. Distinct element analysis of attrition of the granular solids under shear deformation. *Chem. Eng. Sci.*, 61, 5991-6001.

Remy, B., Khinast J.G. and Glasser B.J., 2012. Wet granular flows in a blade mixer: Experiments and simulations of monodisperse spheres. *AIChE Journal*, 58, 3354-3369.

Shi, D. and McCarthy, J.J., 2008. Numerical simulation of liquid transfer between particles. *Powder Technol.*, 184, 64-75.

Stewart, R.L., Bridgwater, J., Zhou, Y.C. and Yu, A.B., 2001. Simulated and measured flow of granules in a bladed mixer-a detailed comparison. *Chem. Eng. Sci.*, 56, 5457-5471.

Tardos, G., McNamara, S. and Talu, I., 2003. Slow and intermediate flow of a frictional bulk powder in the couette geometry. *Powder Technol.*, 131, 23-39.

Thornton, C., and Anthony, S.J., 1998. Quasi-static deformation of particulate media. *Philo. Trans.*, 356, 2763-2782.

Thornton, C., and Sun, G., 1993. Axisymmetric compression of three dimensional polydisperse systems of spheres. *Powders and grains*, 93, 129-134.

Willett, C.D., Adams M.J., Johnson, S.A. and Seville, J.P.K., 2000. Capillary bridge between two spherical bodies. *Langmuir*, 16, 9396-9405.

Zamponi, F., 2008. Packings close and loose. *Nature*, 453, 606-607.

Zhou, Y.C., Wright, B.D., Yang, R.Y., Xu, B.H. and Yu, A.B., 1999. Rolling friction in the dynamic simulation of sandcastle formation. *Physica A*, 269, 536-553.

Zhou, Y.C., Xu, B.H., Yu, A.B. and Zulli, P., 2002. An experimental and numerical study of the angle of repose of coarse sphere. *Powder Technol.*, 125, 45-54.

### Appendices: Investigation of the effect of the rotational speed of the shear cell on the stress ratio response during shearing

Two values of the rotational speed of the shear cell were used  $\omega = 0.05 \text{ rpm}$ , which is the same value as the experimental test and  $\omega = 1 \text{ rpm}$ , which is used for all simulated tests. We observe that by increasing the speed of the shear cell we speed up the stress ratio to reach the steady-state, where both curves seem to have the same average value. The increase of the rotational speed helps to reduce the time of the simulation significantly especially that we are focusing on the steady-state in this study.

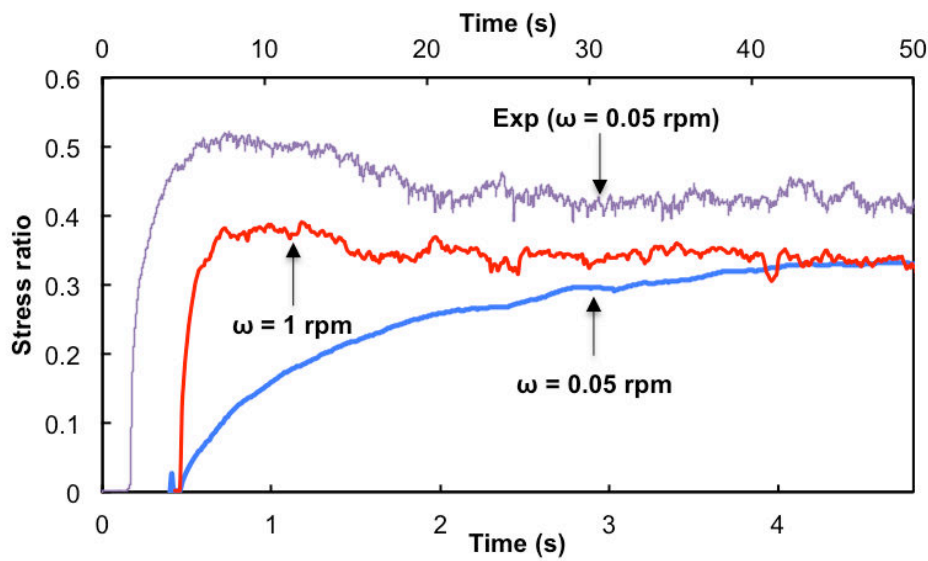


Fig.1. The stress ratio variation during shearing for two different rotational speed values of the shear cell.





## Conclusions and perspectives

The ultimate goal of this study is to provide a qualitative and quantitative analysis of the wet granular material behaviour. This analysis is at two complementary levels: macroscopic and microscopic scales, using two approaches: experiments and simulations. The two approaches allow us to achieve most of our objectives:

- The experimental analysis of the shear resistance of wet glass beads shows the dependence of the shear response on both the liquid contents and normal stresses. This dependence appeared as a non-linear shear-normal stresses relationship implying different regimes. In particular, different regimes were observed at low and high normal stresses.
- The variation of the liquid contents affects also the voidage fraction of the granular bed as a result of the formation of liquid bridges in the unsaturated state and the filling of voids by liquid in the saturated state. The relationship between the voidage fraction and the inter-particle forces has been studied by Feng and Yu (2000) and Yu *et al.* (2003) and many of the results have been supported by our study. We provide also an investigation of the voidage fraction at wide range of liquid contents. However, a relationship between the shear resistance and the voidage fraction of the granular bed is still not well understood.
- The investigation of the impact of the particle size shows an increase of the capillary forces and the number of liquid bridges per unit surface with a decrease in the particle size. This affects consequently the shear resistance of the wet granular material.
- The stick-slip motion, which accompanies the shear stress response, appears when adding minute amounts of liquid. The amplitude and the period of the stick-slip oscillation change with the applied normal stress and the liquid content changing. More investigation in this subject is also needed.
- The study of the tensile strength using Rumpf model and the comparison with the experimental results provide an analysis based on the number of liquid bridges broken. An increase of the tensile strength at high normal stress is due to the large number of liquid bridges broken under shearing. A decrease of the tensile strength at low normal stress is due to the small number of liquid bridges broken caused by the rolling rearrangements.
- The numerical study using DEM allowed to investigate other parameters on the shear behaviour of the wet granular material namely the sliding friction coefficient and the Young's modulus. The comparison between the simulated and the experimental results provides a quantitative analysis of the number of liquid bridges and the capillary forces. A large particle size was used for the simulation to reduce the computational time, however the increase of the particle size change some of the capillary force effects, e.g. it reduces the effect of the liquid content variation on the capillary forces.

This study gives an analysis of some aspects of the wet granular material behaviour, however, as it can be noticed from the perspectives, a lot of other aspects need to be studied yet. Even for simple systems, i.e. mono-dispersed spherical beads in quasi-static regime, the analysis is still complicated. Moreover, the change of some parameters can largely change the obtained results, such the particle size studied in this work. Thus we encourage more comparative studies using other materials (solid and liquid). The influence of the induced viscosity in liquid bridges is also an interesting case to be investigated.

## Conclusions et perspectives

L'objectif final de ce travail est d'étudier qualitativement et quantitativement le comportement du milieu granulaire humide. Cette étude est faite sur deux niveaux d'analyse : macroscopique et microscopique, au moyen d'une approche expérimentale et de simulation numérique. Ces deux approches permettent d'atteindre la majorité des objectifs :

- L'analyse expérimentale de billes de verre humides a montré une dépendance de la réponse au cisaillement à la variation de la quantité de liquide et la contrainte de cisaillement appliquée. Cette dépendance apparaît comme une variation non-linéaire de la contrainte de cisaillement en fonction de la contrainte normale donnant lieu à différents régimes. En particulier, deux différents régimes ont été observés selon à faible ou à forte contrainte normale.
- La variation de la quantité de liquide affecte aussi bien la porosité de lit granulaire en raison de la formation de pont capillaire pour l'état insaturé et du remplissage de vide par le liquide en état saturé. La relation entre la porosité et les forces inter-particulaires a été étudiée par Feng and Yu (2000) and Yu *et al.* (2003) et la plupart des résultats ont été confirmés par cette étude. Nous avons présenté également une étude plus élargie de la variation de la porosité avec la fraction de liquide. Cependant une relation entre la résistance au cisaillement et la porosité du lit granulaire n'est toujours pas totalement comprise.
- L'effet de la taille de particules a montré une augmentation de forces capillaires et le nombre de pont liquide par unité de surface pour une diminution de la taille de particules. Ceci affecte également la résistance à l'écoulement de milieu granulaire.
- Le glissement saccadé, accompagnant la réponse de la contrainte de cisaillement, apparaît dès l'introduction d'une faible quantité de liquide. L'amplitude et la fréquence de ce signal dépendent de la fraction de liquide et de la contrainte normale appliquée. Ces résultats peuvent être exploités d'avantage afin d'obtenir des informations sur la déformation de milieu granulaire en régime quasi-statique.
- L'étude théorique de la traction par le modèle de Rumpf et de Schubert et la comparaison avec les résultats expérimentaux permettent une analyse qualitative de nombre de ponts liquide. A forte contrainte normale, l'augmentation de la traction est due à un large nombre de ponts liquide brisés sous cisaillement. A faible contrainte normale, la diminution de la traction est due à un nombre de ponts liquide brisés plus faible en présence de réarrangement de roulement de billes.
- La méthode de simulation numérique DEM a permis d'étudier certains paramètres de milieu granulaire humide tel que le module de Young et le coefficient de glissement à l'échelle de particule. La comparaison entre la simulation et l'expérimentation donne une analyse quantitative des forces capillaires et du nombre de ponts liquides en jeu. La taille de particules dans la simulation numérique, relativement large, limite les effets

capillaires, notamment l'effet de la variation de la quantité de liquide sur les forces capillaires.

Cette étude donne une analyse de certains aspects du comportement de milieu granulaire humide et ouvre des perspectives sur d'autres aspects qui méritent d'être étudié. Même pour le système simple (milieu granulaire sphérique et mono-disperse en régime quasi-statique), le comportement de milieu granulaire humide reste compliqué à analyser. De plus, le changement de certaines propriétés de milieu peut changer les résultats obtenus (par exemple : la taille de particules, la rugosité de surface, la nature de liquide). Ainsi nous encourageons des études comparatives en utilisant d'autres matériels (solide et liquide). L'influence de la viscosité de liquide accompagnant les effets capillaires est également intéressante à étudier.

## References

- Adams, M.J. and Perchard, V., 1985. The cohesive forces between particles with interstitial liquid. *Ins. Chem. Eng. Symp.*, 91, 147-160.
- Albert, R., Albert, I., Hornbaker, D., Schiffer, P. and Barabasi, A., 1997. Maximum angle of stability in wet and dry spherical granular media. *Phys. Rev. E*, 56, R6271.
- Antony, S.J. and Kruyt, N.P., 2009. Role of interparticle friction and particle-scale elasticity in the shear strength mechanism of three-dimensional granular media. *Phys. Rev. E*, 79, 031308(1)-031308(9).
- Bagi, K., 1996. Stress and strain in granular assemblies. *Mech. Mater.*, 22, 165-177.
- Bharadwaj, R., Ketterhagen, W.R. and Hancock, B.C., 2010. Discrete element simulation study of a freeman powder rheometer. *Chem. Eng. Sci.*, 65, 5747 – 5756.
- Beare, W.G. and Bowden, F.P., 1935. Physical properties of surfaces. I. Kinetic friction. *Philos. Trans. R. Soc. A*, 234, 329-354.
- Bocquet, L., Charlaix, E., Ciliberto, S. and Crassous, J., 1998. Moisture-induced ageing in granular media and the kinetics of capillary condensation. *Nature*, 396, 735-737.
- Bocquet, L., Charlaix, É., and Restagno, F., 2002. Physics of humid granular media. *Comptes Rendus Phys.*, 3, 207–215.
- Brown, R.L. and Richards, J.C., 1960. Profile of flow of granules through apertures. *Trans. Inst. Chem. Eng.* 38, 243-256.
- Capone, G., d'Agostino, V., della Valle, S. and Guida, D., 1992. Stick-slip instability analysis. *Meccanica*, 27, 111-118.
- Carr, J.F., 1967. Tensile strength of granular materials. *Nature*, 213(5081), 1158-1159.
- Collet, R., 2010. Critères de malaxabilités des milieux granulaires humides. Ph.D Thesis, University of Toulouse, Toulouse.
- Cundall, P.A., 1971. A computer model for simulating progressive, large-scale movements in blocky rock systems. *Proceedings of the international Symposium on Rock Mechanics*. Nancy, France, 129-136.
- Cundall, P.A. and Strack, O.D.L., 1979. A discrete numerical model for granular assemblies. *Geotechnique*, 29, 47 – 65.
- DEM\_Solutions, 2015. EDEM 2.7 User Guide. DEM Solutions Limited, Edinburgh, 1 – 133.
- Denis, J., Briant, J. and Hipeaux, J.C. 1997. *Physico-chimie des lubrifiants*. Edition Technip Duran J., Sables, poudres, et grains, Eyrolles Sciences.
- Feng, C.L., Yu, A.B., 1998. Effect of liquid addition on the packing of mono-sized coarse spheres. *Powder Technol.*, 99, 22-28.
- Feng, C.L. and Yu, A.B., 2000. Quantification of the relationship between porosity and interparticle forces for the packing of wet uniform spheres. *J. of Colloid and Interface Sci.*, 231, 136-142.
- Fischer-Cripps, A.C., 2011. *Nanoindentation*. Springer, New York Dordrecht Heidelberg

London.

Fisher, R.A., 1926. On the capillary forces in an ideal soil; correction of formulae given by W. B. Haines. *J. Agr. Sci.*, 16, 492-505.

Fournier, Z., Geromichalos, D., Herminghaus, S., Kohonen, M.M., Mugele, F., Scheel, M., Schulz, M., Schulz, B., Schier, Ch., Seemann, R. and Skudelny, A. 2005. Mechanical properties of wet granular materials. *J. Phys.: Condens. Matter*, 17, S477-S502.

Foerster, S.F., Louge, M.Y., Chang, H. and Allia, K., 1994. Measurement of the collision properties of small spheres. *Phys. Fluids*, 6, 1108-1115.

Fraysse, N., Thomé, H., and Petit, L., 1999. Humidity effects on the stability of a sandpile. *Eur. Phys. J. B*, 11, 615–619.

Garg, R., Galvin, J., Li, T. and Pannala, S., 2012. Open-source Mfix-DEM software for gas-solids flows: Part I-Verification studies. *Powder Technol.*, 220, 122 – 137.

Gras, J.P., 2011. Approche micromécanique de la capillarité dans les milieux granulaire : rétention d'eau et comportement mécanique. Ph.D Thesis, Université Montpellier II, Montpellier.

Goldman, A.J., Cox, R.G. and Brenner, H., 1967. Slow viscous motion of a sphere parallel to a plane wall – I. motion through a quiescent fluid. *Chem. Eng. Sci.*, 22, 637-651.

Han, F., Zhang, J., Chen, G. and Wei, X., 2008. Density, viscosity, and excess properties for aqueous poly(ethylene glycol) solutions from (298.15 to 323.15) K. *J. Chem. Eng. Data*, 53, 2598-2601.

Hare, C., 2015. Bulk characterisation of powders. Course: powder characterisation chemical, physical and mechanical properties, University of Leeds, Leeds.

Hare, C., Zafar, U., Ghadiri, M., Freeman, T., Clayton, J. and Murtagh, M.J., 2015. Analysis of the dynamics of the FT4 powder rheometer. *Powder Technol.*, 285, 123-127.

Helio, P.N. and Meire, P.S.B., 2013. Linear and nonlinear Hertzian contact models for materials in multibody dynamics. 22<sup>nd</sup> international congress of mechanical engineering (COBEM), Ribeirão Preto, SP, Brazil.

Hertz, H., 1882. Über die Berührung fester elastischer Körper. *J. für die reine und angewandte Mathematik*, 92, 156-171.

Hornbaker, D., Albert, R., Albert, I., Barabasi, A. and Schiffer, P., 1997. What keeps sandcastles standing? *Nature*, 387, 765.

Hotta, K., Takeda, K. and Linoya, K., 1974. The capillary binding force of a liquid bridge. *Powder Technol.*, 10, 231-242.

Hsiau, S., and Shieh, Y., 2000. Effect of solid fraction on fluctuations and self-diffusion of sheared granular flows. *Chem. Eng. Sci.*, 55, 1969-1979.

Huntzicker, W.E., 2003. How newspapers reported a milling disaster 125 years ago. *Hennepin History*, 62, 18-34.

Israelachvili, J.N., 1991. Intermolecular and surface forces. Academic Press, London.

Iveson, S.M., 2002. Limitations of one-dimensional population balance models of wet

granulation processes. *Powder Technol.*, 124, 219-229.

Iveson, S.M., Litster, J.D., Hapgood, K. and Ennis, B.J., 2001. Nucleation, growth and breakage phenomena in agitated wet granulation processes: a review. *Powder Technol.*, 117, 3-39.

Johnson, K.L., 1985. *Contact Mechanics*, Cambridge University Press, Cambridge, UK.

Johnson, K.L., Kendall, K. and Roberts, A.D., 1971. Surface energy and the contact of elastic solids. *Proc. R. Soc. Lond. A*, 324, 301-313.

Johanson, K., Rabinovich, Y., Moudgil, B., Breece, K. and Taylor, H., 2003. Relationship between particle scale capillary forces and bulk unconfined yield strength. *Powder Technol.*, 138, 13-17.

Karmakar, S., 2014. Experimental investigations of mechanical properties of wet granular materials. PhD Thesis, University of Saarlandes, Saarbrücken.

Klein, N.S., Bachman, J., Aguado, A. and Toralles-Carbonari, B., 2012. Evaluation of the wettability of mortar component granular materials through contact angle measurements. *Cem. Concr. Res.*, 42, 1611-1620.

Lian, G., Thornton, C. and Adams, M.J., 1998. Discrete particle simulation of agglomerate impact coalescence. *Chem. Eng. Sci.*, 53, 138-147.

Lian, G., Thornton, C. and Adams, M.J., 1993. A theoretical study of the liquid bridge force between rigid spherical bodies. *J. Colloid Interface Sci.*, 161, 3381-3391.

Lommen, S., Schott, D. and Lodewijks, G., 2014. DEM speedup: Stiffness effects on behavior of bulk material. *Particology*, 12, 107 – 112.

Louati, H., Oulahna, D. and de Ryck, A., 2015. Apparent friction and cohesion of a partially wet granular material in steady-state shear. *Powder Technol.*, 278, 65-71.

Lu, N., Wu, B., Tan, C., 2007. Tensile strength characteristics of unsaturated sands. *Journal of Geotechnical and Geoenvironmental Eng.*, 133(2), 144 – 154.

Lubert, M., 2000. Aptitude à l'écoulement d'un milieu granulaire : exploitation des instabilités de cisaillement et évaluation de vieillissement. Ph.D Thesis, Université de Provence, Marseille.

Laubert, M. and de Ryck, A. 2001. Slip events and dilatancy in a sheared fine noncohesive powder. *Phys. Rev. E*, 63 (2), 021502.

Luding, S., 2008. Cohesive, frictional powders: contact models for tension. *Granular Matter* 10, 235-246.

Luding, S., 2008. Constitutive relations for the shear band evolution in granular matter under large strain. *Particology*, 6, 501-505.

Majid, M. and Walzel, P., 2009. Convection and segregation in vertically vibrated granular beds. *Powder Technol.* 192, 311-317.

Maugis, D., 1987. Adherence of elastomers: Fracture mechanics aspects. *J. Adhesion Sci. Technol.*, 1, 105-134.

Malone, K.F. and Xu, B. H., 2008. Determination of contact parameters for discrete element method simulations of granular systems. *Particology*, 6, 521 – 528.



- Mazon, T.G., Levine, A.J., Ertas, D. and Halsey, T.C., 1999. The critical angle of wet sand piles. *Phys. Rev. E*, 60, R5044-R5047.
- Mazzone, D.N., Tardos, G.I. and Pfeffer, R., 1986. The effect of gravity of the shape and strength of a liquid bridge between two spheres. *J. Colloid Interface Sci.*, 113, 544-556.
- Mikami, T., Kamiya, H., and Horio, M., 1998. Numerical simulation of cohesive powder behavior in a fluidized bed. *Chem. Eng. Sci.*, 53, 1927-1940.
- Milewski, J.V., 1987. *Handbook of fillers and reinforcements for plastics*. Van Nostrand-Reinhold Co, New York.
- Mitarai, N. and Nori, F., 2006. Wet granular materials. *Adv. Phys.*, 55, 1-45.
- Mizuno, M., Fukaya, A. and Jimbo, G., 1991. The estimation of packing characteristics by centrifugal compaction of ultrafine. *KONA Powder Part.* 9, 19-27.
- Moller, P.C.F., and Bonn, D., 2007. The shear modulus of wet granular matter. *EPL journal*, 80, 1-5.
- Nase, S.T., Vargas, W.L., Abatan, A.A. and McCarthy, J.J., 2001. Discrete characterization tools for cohesive granular material. *Powder Technol.*, 116, 214-223.
- Nedderman, R.M., 1992. *Statics and kinematics of granular materials*. Cambridge University Press, 352.
- Newitt, D.M. and Conway-Jones, J.M., 1958. Contribution to the theory and practice of granulation. *Trans. Inst. Chem. Eng.*, 36, 422-442.
- Ning, Z. and Ghadiri, M., 2006. Distinct element analysis of attrition of granular solids under shear deformation. *Chem. Eng. Sci.*, 61, 5991 – 6001.
- Onoda, G.Y. and Liniger, E.G., 1990. Random loose packings of uniform spheres and the dilatancy onset. *Phys. Rev. Lett.*, 64, 2727.
- Oulahna, D., Collet, R., and de Ryck, A., 2012. Mechanical resistance due to shearing of partially wet granular media. *KONA: Powder & particle journal*, 30, 109.
- Pasha, M., Dogbe, S., Hare, C., Hassanpour, Ali. and Ghadiri, M., 2014. A linear model of elasto-plastic and adhesive contact deformation. *Granular Matter*, 16, 151 – 162.
- Persson, A. and Frenning, G., 2013. The influence of rolling friction on the shear behaviour of non-cohesive pharmaceutical granules – An experimental and numerical investigation. *Eur. J. Pharm. Sci.*, 49, 241 – 250.
- Pierrat, P. and Caram, H.S., 1997. Tensile strength of wet granular materials. *Powder Technol.*, 91, 83-93.
- Pietsch, W., 1968. Tensile strength of granular materials. *Nature*, 217, 736.
- Pietsch, W., 1991. *Size enlargement by agglomeration*. John Wiley and Sons, Chichester.
- Pietsch, W., 2002. *Agglomeration process: phenomena, technologies, equipment*. Wiley-VCH, Weinheim.
- Pitois, O., Moucheront, P. and Château, X., 2000. Liquid bridge between two moving spheres: an experimental study of viscosity effects. *J. Colloid Interface Sci.*, 231, 26-31.

- Rabinovich, Y.I., Esayanur, M.S. and Moudgil, B.M., 2005. Capillary forces between two spheres with a fixed volume liquid bridge: theory and experiment. *Langmuir*, 21, 10992–10997.
- Rathbone, D., Marigo, M., Dini, D. and van Wachem, B., 2015. An accurate force-displacement law for the modelling of elastic-plastic contacts in discrete element simulations. *Powder Technol.*, 282, 2-9.
- Remy, B., Khinast J.G. and Glasser B.J., 2012. Wet granular flows in a blade mixer: Experiments and simulations of monodisperse spheres. *AIChE Journal*, 58, 3354-3369.
- Robbins, M.O., 1999. Jamming, friction and unsteady rheology. *Cond-mat/9912337*.
- Rondet, E., Ruiz, T. and Cuq, B., 2013. Rheological and mechanical characterization of wet agglomerates processed in low shear mixer. *J. Food Eng.*, 117, 67–73.
- Rumpf, H., 1962. The tensile strength of granules and agglomerates. *Intersci. Publ.*, 379-418.
- Saleh, K. and Guigon, P., 2009. Mise en oeuvre des poudres – granulation humide : bases et théorie. *Techniques de l'ingénieur*, J2253 V1, 1-14.
- Savkoor, A.R. and Briggs, G.A.D., 1977. The effect of tangential force on the contact of elastic solids in adhesion. *Proc. R. Soc. Lond. A*. 356, 103-114.
- Schubert, H., 1984. Capillary forces: modeling and application in particulate technology. *Powder Technol.*, 37, 105-116
- Schulze, D., 2003. Time- and velocity-dependent properties of powders affecting slip-stick oscillations, *Chem. Eng. Technol.*, 26 (10), 1047-1051.
- Schulze, D., 2008. *Powders and bulk solids: behavior, characterization, storage and flow*. Springer-Verlag Berlin Heidelberg.
- Schwedes, J. and Schulze, D., 1990. Measurement of flow properties of bulk solids. *Powder Technol.*, 61, 59-68.
- Scott, G.D., 1962. Packing of spheres: Packing of equal spheres. *Nature*, 193, 465.
- Scott, G.D. and Kilgour, D.M., 1969. The density of random close packing of spheres. *Brit. J. Appl. Phys.*, 2, 863-866.
- Seville, J.P.K., Willett, C.D. and Knight, P.C., 2000. Interparticle forces in fluidisation: a review. *Powder Technol.*, 113, 261-268.
- Shäfer, J., Dippel, S. and Wolf, D.E., 1996. Force schemes in simulations of granular materials. *Journal de Physique I France*, 6, 5 – 20.
- Shi, D. and McCarthy, J.J., 2008. Numerical simulation of liquid transfer between particles. *Powder Technol.*, 184, 64-75.
- Silbert, L.E., Ertas, D., Grest, G.S., Halsey, T.C., Levine, D. and Plimpton, S.J., 2001. Granular flow down an inclined plane: Bagnold scaling and rheology. *Phys. Rev. E*, 64, 051302.
- Simons, S., Seville, J. and Adams, M., 1994. An analysis of the rupture energy of pendular liquid bridges. *Chem. Eng. Sci.*, 49, 2331–2339.
- Stewart, R.L., Bridgwater, J., Zhou, Y.C. and Yu, A.B., 2001. Simulated and measured flow of

granules in a bladed mixer-a detailed comparison. *Chem. Eng. Sci.*, 56, 5457-5471.

Tagami, N. and Horio, M., 2003. A computational study of fluidized beds with particle size distribution. The second Asian particle technology symposium (APT 2003), Penang, Malaysia.

Tardos, G., McNamara, S. and Talu, I., 2003. Slow and intermediate flow of a frictional bulk powder in the couette geometry. *Powder Technol.*, 131, 23-39.

Tegzes, P., Albert, R., Paskvan, M., Barabasi, A., Vicsek, T. and Schiffer, P., 1999. Liquid-induced transitions in granular media. *Phys. Rev. E*, 60, 5823-5826.

Thornton, C., 1997. Coefficient of restitution for collinear collisions of elastic-perfectly plastic spheres. *J. Appl. Mech.*, 64, 383-386.

Thornton, C., and Anthony, S.J., 1998. Quasi-static deformation of particulate media. *Philo. Trans.*, 356, 2763-2782.

Thornton, C., and Sun, G., 1993. Axisymmetric compression of three dimensional polydisperse systems of spheres. *Powders and grains*, 93, 129-134.

Thornton, C. and Yin, K.K., 1991. Impact of elastic spheres with and without adhesion. *Powder technol.*, 65, 153-166.

Tsuji, Y., Tanaka, T. and Ishida, T., 1992. Lagrangian numerical simulation of plug flow of cohesionless particles in a horizontal pipe. *Powder Technol.*, 71, 239 – 245.

Visser, J., 1989. An invited review: Van der Waals and other cohesive forces affecting powder fluidization. *Powder Technol.*, 58, 1-10.

Yang, R.Y., Zou, R.P. and Yu, A.B., 2000. Computer simulation of the packing of fine particles. *Phys. Rev. E*, 62, 3900.

Yang, R.Y., Zou, R.P. and Yu, A.B., 2001. Effect of capillary force on the packing of particles: a numerical study. *Proc. 6<sup>th</sup> International Congress on Chemical Engineering*, Melbourne, Australia, paper 175.

Yang, R.Y., Zou, R.P. and Yu, A.B., 2003. Effect of material properties on the packing of fine particles. *J. Appl. Phys.*, 94, 3025.

Yu, A.B., Bridgwater, J., Burbidge, A., 1997. On the modelling of the packing of fine particles. *Powder Technol.*, 92, 185-194.

Yu, A.B., Feng, C.L., Zou, R.P. and Yang, R.Y., 2003. On the relationship between porosity and inter-particle forces. *Powder Technol.*, 130, 70-76.

Yuan, Y. and Lee, T.R., 2013. Contact angle and wetting properties Surface science techniques. In: Bracco, G. and Holst, B. ed. *Surface science techniques*. Springer-Verlag Berlin Heidelberg, 3-34.

Walton, O.R. and Johnson, S.M., 2009. Simulating the effects of interparticle cohesion in micron-scale powders. *AIP Conf. Proc.*, 1145, 897-900.

Wakeman, R.J., 1975. Packing densities of particles with log-normal size distributions. *Powder Technol.*, 11, 297-299.

Weir, G. and Tallon, S., 2005. The coefficient of restitution for normal incident, low velocity particle impacts. *Chem. Eng. Sci.*, 60, 3637 – 3647.

Wensrich, C. M. and Katterfeld, A., 2012. Rolling friction as a technique for modelling particle shape in DEM. *Powder Technol.*, 217, 409 – 417.

Willett, C.D., 1999. The micromechanics of wet particulate materials. Ph.D Thesis, University of Birmingham, Birmingham.

Willett, C.D., Adams, M.J., Johnson, S.A. and Seville, J.P.K., 2000. Capillary bridge between two spherical bodies. *Langmuir*, 16, 9396-9405.

Zamponi, F., 2008. Packings close and loose. *Nature*, 453, 606-607.

Zhou, Y.C., Xu, B.H., Yu, A.B. and Zulli, P., 2002. An experimental and numerical study of the angle of repose of coarse sphere. *Powder Technol.*, 125, 45-54.

Zhou, Y.C., Wright, B.D., Yang, R.Y., Xu, B.H. and Yu, A.B., 1999. Rolling friction in the dynamic simulation of sandpile formation. *Physica A: statistical mechanics and its applications*, 269, 536 – 553.

Zhu, H.P., Zhou, Z.Y., yang, R.Y. and Yu, A.B., 2007. Discrete particle simulation of particulate systems: Theoretical developments. *Chem. Eng. Sci.*, 62, 3378 – 3396.

Zhu, H.P., Zhou, Z.Y., yang, R.Y. and Yu, A.B., 2008. Discrete particle simulation of particulate systems: A review of major applications and findings. *Chem. Eng. Sci.*, 63, 5728 – 5770.

## **Experimental and numerical study of humid granular material: influence of liquid content in quasi-static regime**

### **Abstract**

We study experimentally and numerically the shear behaviour of wet granular material. We investigate the effect of the liquid content and the applied normal stresses to this behaviour. An annular shear cell was used to carry out the experiments, for a large range of applied normal stress from about 0.3 kPa to 12 kPa. The results give the variation of the shear stress at steady-state as a function of the normal stress for a wide range of liquid fraction. The incorporated liquid goes from forming bridges at the contact point to completely filling the space between grains. The shear resistance and the voidage fraction variations with the liquid fraction were analysed. Depending on the applied normal stress and the liquid fraction, different regimes of the shear resistance were identified. The discrete element method (DEM) was used to gain a microscopic understanding of the shear behaviour of dry and partially wet granular material in the shear cell. Large size glass beads were used to speed up the computational time and to facilitate characterisation at the particle scale. First, the influence of the microscopic properties of the particle (The Young's modulus and the sliding friction) on the macroscopic properties of dry and wet granular materials (the coordination number, the voidage fraction, the shear ratio and the velocity of particles) was investigated. Secondly, the shear behaviour of the partially wet granular material for different liquid fractions and normal stresses was studied. The capillary forces and the number of liquid bridges were quantitatively analysed.

**Keywords:** Wet granular material, capillary force, shear test, voidage fraction, Discrete element method (DEM)

## **Rhéologie de milieu granulaire humide : influence de la quantité de liquide en régime quasi-statique par approche expérimentale et simulation numérique**

### **Résumé**

Cette thèse est une étude expérimentale et numérique du comportement au cisaillement de milieu granulaire humide sous l'effet de la quantité de liquide introduite et la contrainte normale appliquée. Les expériences ont été faites sur une cellule de cisaillement annulaire, pour une large gamme de contraintes appliquées allant de presque 0.3 kPa à 12 kPa. Les résultats donnent la variation de la contrainte de cisaillement en régime stationnaire en fonction de la contrainte normale pour une large variation de la quantité de liquide. Le liquide dans le milieu granulaire va de ponts liquides formés au point de contact jusqu'au remplissage totale de l'espace entre les grains. L'effet de liquide sur la résistance au cisaillement et la porosité de milieu granulaire a été analysé. Différents régimes du comportement de milieu granulaire humide ont été identifiés. Afin d'acquérir une compréhension microscopique du comportement au cisaillement de milieu granulaire sec et partiellement humide, la méthode des éléments discrets (DEM) a été utilisée. Des billes de verre de grande taille (2 mm de diamètre) ont été utilisées pour réduire le temps de simulation et faciliter la caractérisation à l'échelle de particule. Une première partie a été consacrée à l'étude de l'effet des propriétés microscopiques de particule (Module de Young et la friction de glissement) sur les propriétés macroscopiques de milieu granulaire sec et humide (le nombre de coordination, la porosité, le ratio de contraintes et la vitesse de particules). Une deuxième partie a été concernée par l'étude du comportement au cisaillement de milieu granulaire humide pour différentes fractions de liquide et différentes contraintes normale appliquées. En particulier, les forces capillaires et le nombre de ponts liquide ont été quantitativement analysés.

**Mots-clés :** Milieu granulaire humide, force capillaire, test de cisaillement, porosité, méthode des éléments discrets (DEM)